

Politecnico di Milano

School of Industrial and Information Engineering

Master of Science in Mechanical Engineering



PRELIMINARY DESIGN AND AERODYNAMIC PERFORMANCE EVALUATION OF MULTI-STAGE CENTRIFUGAL COMPRESSORS

Advisor: Prof. Paolo Gaetani

Co-Advisor: Dr. Sergio Lavagnoli

Candidate:

Andrea Cappelletti - Matr. 853746

Academic Year 2016-2017

Ringraziamenti

Ringrazio il Prof. Gaetani per avermi offerto l'opportunità di partecipare a questa nuova esperienza. Un grazie anche a Sergio per avermi seguito da vicino lungo questo percorso e a Zuheyr per il caloroso sostegno. Ringrazio ovviamente Alessandro per avermi offerto la sua supervisione e i suoi consigli durante tutto il progetto.

Un ringraziamento speciale va alla mia famiglia, che ho sempre sentito accanto nonostante la lontananza.

Ringrazio infine le tante persone che al Von Karman hanno contribuito a rendere speciale questa esperienza.

Abstract

The present Master Thesis deals with the implementation of a program for the preliminary design and performance evaluation of multi-stage centrifugal compressors. In this regard, a research work has been previously successfully developed by the former student of Polytechnic of Milan Alessandro Romei, leading to an automatic Matlab® program, called CCD (Centrifugal Compressor Design). CCD allows to generate an initial sizing of the machine requiring only few input parameters such as the mass flow, the suction conditions, the fluid properties and the total pressure ratio. Nonetheless, since in CCD the performances of the compressor are considered to depend upon global parameters, as the flow coefficient and the peripheral Mach number, the need of a more precise approach was felt, so to search for a better capturing of the real behavior of the machine. Proceeding from this basis, the present project is targeting the implementation of a numerical design methodology based on modern 1D loss correlations, that can guarantee a good performance prediction at the operating point, to model the principal components of multi-stage centrifugal compressors: the impeller, the vaned and vaneless diffuser, the return system and the final volute.

Successively, the computation of the efficiency and pressure ratio maps of the compressor has been carried out adapting the existing off-design procedure created by Casey and Robinson (2013) and developed by Al-Busaidi and Pilidis (2016).

Finally, four test cases, representative of different kinds of compressors, have been accounted to apply and validate the code comparing the predictions of the main geometrical and thermodynamic quantities with reference data and with the results of the previous version of CCD.

Sommario

Il compressore centrifugo rappresenta una delle macchine a fluido maggiormente versatili, svariando da applicazioni per impianti di trattamento chimico fino a sistemi di refrigerazione e propulsione dei veicoli, grazie ad una buona compattezza e alle elevate prestazioni che é in grado di garantire, sia in configurazioni monostadio sia multistadio. Inoltre, grande interesse è suscitato dai margini di miglioramento di cui ancora dispone, essendo particolarmente complessi da studiare e comprendere a fondo i meccanismi fluidodinamici che avvengono al suo interno, anche se grandi sforzi computazionali vengono compiuti a riguardo. Per tali motivi, la fase di progettazione diventa molto delicata e strumenti di supporto al lavoro degli ingegneri possono rivelandosi molto utili per indirizzare correttamente i successivi studi. In questo contesto si inserisce la presente Tesi Magistrale, svolta presso il Von Karman Institute for Fluid Dynamics (VKI) dove si era precedentemente effettuata una collaborazione con un ex studente del Politecnico di Milano, Alessandro Romei, che aveva portato alla creazione di un software Matlab®, chiamato Centrifugal Compressor Design (CCD), per la progettazione preliminare di compressori centrifughi. In breve, ricevendo in un input file i principali parametri di progetto, quali portata, condizioni termodinamiche in ingresso, rapporto di compressione totale e proprietà del fluido di lavoro, CCD genera un dimensionamento di massima della macchina calcolando le principali grandezze geometriche e stima l'efficienza del compressore utilizzando un approccio a parametri globali, tra cui il coefficiente di portata e il numero di Mach.

L'obiettivo di questo lavoro é lo sviluppo e l'implementazione di una metodologia che tenga invece conto, dal punto di vista uno-dimensionale, delle specifiche perdite aerodinamiche che si generano all'interno del compressore per calcolare le prestazioni nel punto di funzionamento e dimensionare di conseguenza i suoi principali componenti: la girante, il diffusore palettato e non palettato, il sistema di ritorno e la voluta. Piú nel dettaglio, le perdite degli elementi non palettati saranno valutate attraverso equazioni di conservazione del momento angolare e di conservazione dell'energia, mentre

per gli altri componenti verranno considerati specifici coefficienti di perdita di pressione totale.

Una volta terminata la parte di design, il programma genera, con una routine preesistente basata sui lavori di Casey e Robinson (2013) e Al-Busaidi e Pilidis (2016), le mappe di efficienza e rapporto di compressione fuori dalla condizione di progetto.

Infine, quattro casi verranno utilizzati per l'applicazione e la validazione della nuova metodologia, considerando macchine molto diverse tra loro: un compressore a tre stadi con interrefrigeratori, un cinque stadi funzionante con una miscela di idrocarburi, un sei stadi adibito alla compressione di idrogeno e lo stadio finale di un compressore assi-centrifugo per uso propulsivo. Il confronto sarà realizzato comparando i risultati della nuova versione di CCD con quella precedente e con i dati disponibili per ciascuno dei precedenti compressori.

List of Symbols

Roman Symbols

A	area inside blade passage	m^2
A_R	area ratio	—
b	blade height	m
B	fractional area blockage	—
c_f	friction coefficient	—
d	diameter	m
D_{eq}	equivalent diffusion factor	—
d_H	hydraulic diameter	m
e	peak to valley surface roughness	m
f_c	loss correction factor	—
h	enthalpy	J
i	incidence	deg
L	mean streamline meridional length	m
L_{ax}	axial length of the compressor	m
L_B	blade mean camberline	m
\dot{m}	mass flow	kg/s
M	Mach number	—
N	rotational speed	rpm
N_{bl}	number of blades	—
N_s	number of seals	—
o	throat opening	m
P	fins pitch	m
p_R	seal pressure ratio	—
r	radius	m
Re	Reynolds number	—
s	pitch, clearance gap	m
t	thickness	m
T	temperature	K
u	peripheral velocity	m/s
v	absolute velocity	m/s
w	relative velocity	m/s

Greek Symbols

α	absolute angle from meridional direction	<i>deg</i>
α_C	streamline slope	<i>deg</i>
β	relative flow angle	<i>deg</i>
γ	specific heat ratio	—
δ_{cl}	clearance gap	<i>m</i>
ϵ	blade blockage/convergence factor	—
λ	total work factor	—
λ_B	blade work factor	—
μ	dynamic viscosity	<i>Pa · s</i>
ρ	density	<i>kg/m³</i>
σ	slip factor	—
ϕ_{01}	inlet flow coefficient	—
ζ	impeller tip distortion factor	—
$\bar{\omega}$	total pressure loss coefficient	—

Subscripts

0	total quantity
1	impeller inlet
2	impeller outlet
3	diffuser vane inlet
4	diffuser vane outlet
5	diffuser outlet
6	volute exit/cross-over bend exit
7	exit cone discharge/return channel exit
8	return system exit
<i>bl</i>	referred to the blade
<i>cl</i>	clearance gap parameter
<i>DF</i>	windage and disk friction
<i>e</i>	eye coordinate
<i>eff</i>	effective quantity
<i>FB</i>	full blade
<i>h</i>	hub coordinate
<i>id</i>	ideal quantity
<i>L</i>	leakage parameter
<i>l</i>	laminar flow value
<i>m</i>	meridional component
<i>max</i>	maximum condition
<i>R</i>	recirculation parameter
<i>r</i>	fully rough condition
<i>s</i>	shroud coordinate
<i>SP</i>	splitter blades
<i>sh</i>	quantity after shock
<i>t</i>	turbulent flow value
<i>tg</i>	tangential component
<i>th</i>	throat parameter

Superscripts

'	relative condition
*	sonic condition

Contents

1	Loss Model	1
1.1	Introduction	1
1.2	Impeller Losses	4
1.2.1	Incidence Loss	5
1.2.2	Diffusion Loss	6
1.2.3	Choking Loss	7
1.2.4	Skin Friction Loss	8
1.2.5	Blade Loading Loss	9
1.2.6	Hub to Shroud Loss	10
1.2.7	Distortion Loss	10
1.2.8	Mixing Loss	11
1.2.9	Clearance loss	11
1.2.10	Supercritical Mach Loss	12
1.2.11	Shock Loss	13
1.3	Parasitic Losses	13
1.3.1	Windage and Disk Friction	13
1.3.2	Leakage Work	15
1.3.3	Recirculation Work	17
2	Design Procedure	19
2.1	Impeller Inlet	24
2.2	Impeller Outlet	30
2.3	Diffuser design	34
2.3.1	Vaneless Diffuser	34
2.3.2	Vaned Diffuser	38
2.4	Stage exit	43
2.4.1	Return System	43
2.5	Volute	49
2.6	Stage performance	54
2.7	Geometry Plot	55
2.8	Output File	56

3 Off Design Performance Maps	57
3.1 Pressure Ratio Map	58
3.2 Efficiency Map	61
3.3 Procedure in CCD	63
4 Validation	67
4.1 3 stages IGCC	68
4.1.1 Off-Design IGCC	72
4.1.2 Match of first stage	75
4.2 5 Stages Process Compressor	78
4.2.1 Off-design 5 stages	80
4.2.2 6 Stages Hydrogen compressor	84
4.2.3 Flow coefficient match	86
4.3 High Efficiency Centrifugal Compressor (HECC)	88
4.3.1 Off-design	92
4.4 Summary of Validation Tests	96
5 Conclusions	97
5.1 Future Works	98
6 References	99

List of Figures

1.1	CCD Scheme	2
1.2	Files for CCD	3
1.3	h-s diagram	4
1.4	Sketch of blade throat opening	7
1.5	Blade surface velocity profile	12
1.6	Typical geometry of a straight-through labyrinth seal	16
2.1	Example of input file for CCD	20
2.2	Settings file	21
2.3	Initial design procedure in case of first stage of a shaft	23
2.4	Initial design procedure in case of following stages	23
2.5	Section of a generic impeller of a centrifugal compressor	25
2.6	Zoom of the region between eye of the compressor and blade inlet	25
2.7	Representation of full and splitted blades	29
2.8	Blade exit angle according to flow coefficient	30
2.9	Exit velocity triangle	32
2.10	Thermodynamic transformations across the impeller	33
2.11	Sketch of impeller followed by a parallel wall diffuser	36
2.12	Sketch of impeller followed by a vaned diffuser	39
2.13	General shape of a return system	44
2.14	Geometry of a circular external volute	50
2.15	Geometry of a circular semi-external volute	50
2.16	Geometry of a rectangular internal volute	51
2.17	General Shape of the volute	51
2.18	Exit cone	54
2.19	Example of the layout of a five stage compressor as generated by CCD	55
2.20	Example of output file gathering the most important stage parameters	56

3.1	Flow coefficient correction for vaned turbocharger	59
3.2	Off-design efficiency correction	59
3.3	Flow coefficient correction at low design Mach number for vaneless stages	60
3.4	Efficiency correction with tip-speed Mach numbers	61
3.5	Input file for the performance maps	63
3.6	Variation of the peak flow coefficient with respect to that at choke	64
3.7	Variation of the surge flow coefficient with respect to that at choke	65
3.8	Example of efficiency performance map	65
3.9	Example of pressure ratio performance map	66
4.1	3 stage geometry plot	69
4.2	Comparison off CCDV03 maps with tests	73
4.3	Comparison of CCD V03 maps with CCD V01	74
4.4	3 stages IGCC geometry with matching input	75
4.5	5 stages efficiency map with test data	81
4.6	5 stages pressure ratio map with test data	81
4.7	5 stages PR map with speed correction	82
4.8	5 stages efficiency map of 100% speedline	82
4.9	5 stages pressure ratio map of 100% speedline	83
4.10	6 stages compressor geometry	84
4.11	Efficiency and PR maps comparison for the 6 stages case	85
4.12	Efficiency and PR maps comparison for the 6 stages case with ϕ_{01} match	86
4.13	High Efficiency Centrifugal Compressor as modeled by NASA	88
4.14	High Efficiency Centrifugal Compressor as sketched by CCD	89
4.15	HECC efficiency map of CCD V03 compared with test data, CFD and CCD V01	93
4.16	HECC pressure ratio map of CCD V03 compared with test data	93
4.17	Efficiency map comparison between CCD V03 and CFD results performed at VKI	94
4.18	Pressure ratio map comparison between CCD V03 and CFD results performed at VKI	95

List of Tables

4.1	IGCC comparison results	70
4.2	IGCC results comparison with CCD V01	71
4.3	IGCC off design constants	72
4.4	Value of off-design constants for low and high Mach numbers .	72
4.5	IGCC comparison between the output of CCD V03 and the test data after matching	76
4.6	IGCC comparison between the output of CCD V03 and CCD V01 with the new geometry for first stage	77
4.7	Comparison between CCD V03 and 5-stage compressor test data	78
4.8	Comparison between CCD V03 and V01 for the 5-stage compressor test case with the same input	79
4.9	5 stages off design paramters for blending function	80
4.10	5 stages off design parameters	80
4.11	Data of 6 stage hydrogen compressor	84
4.12	Six stages compressor comparison between CCD V03 and V01 with $\phi_{01} = 0.027$	85
4.13	Six stages efficiency comparison of CCD V03 and V01 with an inlet flow coefficient for V03 of $\phi_{01} = 0.0181$	86
4.14	Suction parameters for HECC	88
4.15	HECC comparison between CCD V03 results and HECC data	90
4.16	HECC: Comparison between the results of CCD V03 and CCD V01	91
4.17	HECC paramters for blending function	92
4.18	HECC: low and high limit for off-design parameters	92

Chapter 1

Loss Model

1.1 Introduction

Even if nowadays the use of accurate CFD (Computational Fluid Dynamics) simulations for turbomachinery is massive, it is not true that it has swept away less sophisticated instruments from the repertoire of an engineer. In fact, during the first steps of the design phase, the designer usually relies on cheap and quick tools to obtain a reasonable preliminary sizing of the machine on which conduct, only later, more detailed analyses. These are the advantages that a program like CCD can guarantee and that rise the interest in its further improvement.

The new version of CCD can be divided, as it can be seen from fig. (1.1), in 4 different and subsequent parts: the loop for the design, the geometry plot of the compressor, the evaluation of the performance map for the off-design and the generation of the output file containing all the most relevant information about the compressor.

In order to give CCD more flexibility, the program has been organized in a main routine plus several files and subroutines that are recalled by the main one. In fig. (1.2) all the required files and subroutines are reported.

The new task is to implement and integrate in CCD a specific loss model, to evaluate more accurately the performances of the compressor (previously the machine was treated as a black box) and compare the two versions with the same validation cases. In order to keep the same code philosophy, 1D correlations have been found in literature to analyse all the most important components of a centrifugal compressor (i.e. impeller, diffuser, return system and volute). In fact, some loss models about centrifugal compressors have been published across the years, from the studies of Galvas [44] in the 70's and Herbert [40] in the 80's to the works of Whitfield and Baines [5] and Aungier

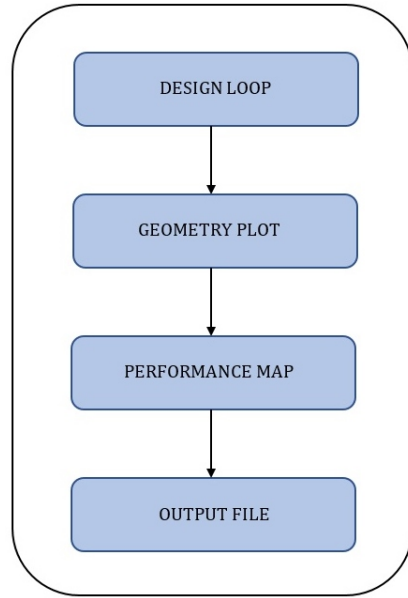


Figure 1.1: Scheme of CCD working principles

[1] in the 90's. In general, the aim of these models is to scorporate the overall losses occurring in a centrifugal compressor into different contributions that have a physical background (meaning they can be related to phenomena like skin friction and blade loading) and can be computed considering only simple geometrical and flow quantities.

The work of R. H. Aungier [1] has been taken as principal reference because found to be complete in terms of modeled components. Moreover, the combination of theoretical analysis and empirical investigations, that constitutes the foundation of 1D loss correlations, is very profound and the author guarantees to have tested and validated it with a huge variety of compressors obtaining good results.

As well explained in [4] 1D losses can be grouped into three models: Zero-Zone, Single-Zone and Two-Zone modelling. The Zero-Zone approach uses characteristical non-dimensional parameters, such as the flow coefficient ϕ and the peripheral Mach number M_{u2} , to estimate the efficiency of the compressor. The Single-Zone considers the flow as uniform and describable by the mean streamline coordinate while the Two-Zone distinguishes between a high momentum fluid, called 'Jet', and a low momentum one, called 'Wake', and analyses the flow differently for the two regions.

Generally, the correlations provided by Aungier belong to the Single-Zone approach even if, for some penalties like incidence and mixing, they refer not only to the meanline coordinate. Aungier employs proper loss formulas for

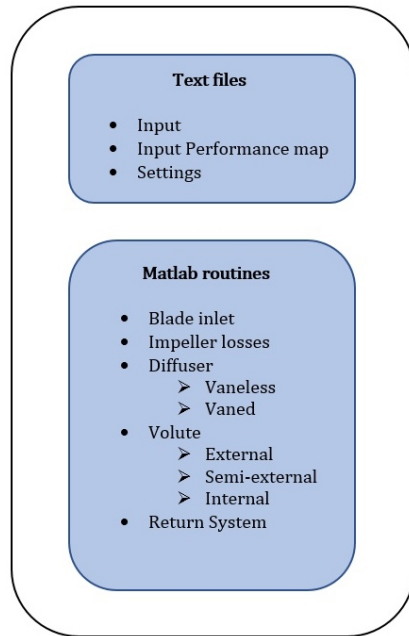


Figure 1.2: Overview of the files needed by the CCD

the vaned components like the impeller, the vaned diffuser and return vane channel while, as it will be later explained, exploits 1D governing equations, such as momentum, energy and gas state, for the vaneless spaces of the compressor.

1.2 Impeller Losses

It has to be pointed out that, when dealing with the only rotating component of the compressor as the impeller is, the velocity to be considered (and therefore all the depending quantities) is the relative and not the absolute one as for all the others, following the kinematic relationship $\vec{v} = \vec{w} + \vec{u}$.

The impeller model of Aungier is based on the total pressure loss coefficients $\bar{\omega}$ to find the real exit relative total pressure p'_02 using the relative inlet total pressure p'_01 and a correction factor f_c :

$$p'_02 = p'_{02,id} - f_c(p'_01 - p_1) \sum_{i=1} \bar{\omega}_i \quad (1.1)$$

As stated by the author himself, a total pressure loss coefficient is more accurate than an enthalpy based one because it is not dependent upon the pressure ratio involved.

For what concerns the impeller, a first distinction stands between internal and external losses as again explained in [4]: the external (or parasitic) losses do not contribute to the pressure generation but they are only responsible for an increment in total temperature. The internal losses, instead, cause a decrease in the pressure rise (see fig. (1.3)).

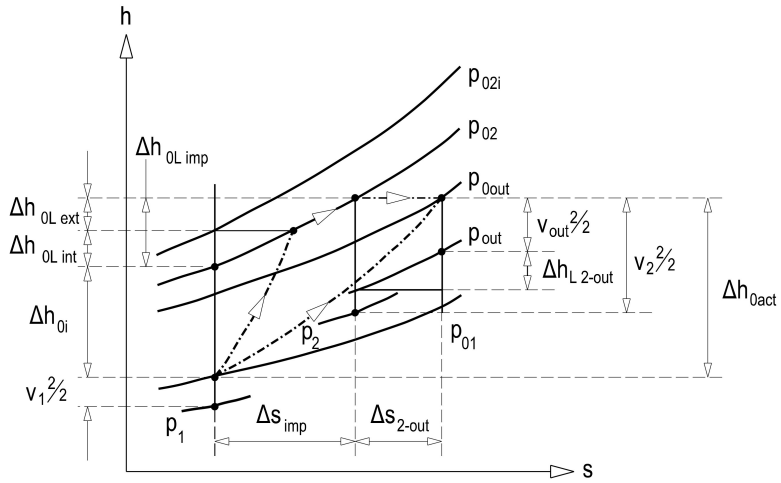


Figure 1.3: h-s diagram of the thermodynamic transformations occurring across the compressor

The following internal losses are considered for the impeller as prescribed by Aungier:

- Incidence
- Clearance
- Skin friction
- Blade loading
- Hub to shroud
- Tip distortion
- Wake mixing
- Supercritical Mach number
- Diffusion
- Choking
- Shock

1.2.1 Incidence Loss

The correlation for the incidence loss is accounting for the flow adjustment into the blade passage as expressed by eq. (1.2). According to the convention adopted, the angles are taken from the meridional direction, the opposite of what done by Aungier, therefore the formulas have been changed to correct this difference.

$$\bar{\omega}_{inc} = 0.8[1 - v_{m1}/(w_1 \cos \beta_{1bl})]^2 + [N_{bl,full} t_{bl}/(2\pi r_1 \cos \beta_{1bl})]^2 \quad (1.2)$$

Eq. (1.2) is applied at hub, mid and shroud inlet stream surfaces and the total pressure incidence loss is computed as a weighted average, where the mid values are weighted 10 times as heavy as the hub and shroud ones. The meridional velocity at blade inlet is assumed to be uniform while the relative angle changes along blade span according to the peripheral velocity. The first term is null in case of design point condition since $w_1 \cos \beta_{1bl}$ is exactly v_{m1} as β_{1bl} is chosen to be equal to design β_1 (so optimal incidence $i_{1,opt}$ is equal to zero). On the other hand, this part will become relevant when dealing with

off-design conditions due to the onset of a perpendicular component hitting directly the blade. The second contribution to the incidence loss, instead, considers the effect of abrupt flow area contraction at the blade leading edge due to the latter's thickness. $N_{bl,full}$ distinguishes the number of full blades since, as will be explained in chapter 2, also splitted blades can be present.

1.2.2 Diffusion Loss

The throat area is defined as the smallest section in a blade passage. To discharge the same mass flow, the throat velocity w_{th} has to be higher than the inlet meridional velocity $w_{1m} = w_1 \cos \beta_1$ as we can see comparing the two terms in eq. (1.7):

$$\dot{m} = \rho_1 A_1 w_1 \cos \beta_1 = \rho_{th} A_{th} w_{th} \quad (1.3)$$

with the density term that will depend on the velocity itself. However, w_{th} is usually lower than the inlet velocity w_1 and so a deceleration, hence a diffusion of the flow, will occur. Since a dissipation is intrinsic in this process we must account for a diffusion loss which is weighted according to the velocity ratio w_{th}/w_1 . The estimation of the throat area is one of the most difficult challenges in 1D preliminary design, also because a detailed geometry profile is inherently missing in a 1D approach. Therefore, a simplified procedure proposed by Whitfield and Baines will be employed. At first, no difference between inlet and throat sections is considered in terms of radial extent, so that the throat height equals the inlet blade height b_1 . Because of this hypothesis, to satisfy rothalpy conservation (see eq. (1.4)) the relative total temperature ($T'_1 = T_1 + \frac{w_1^2}{2c_p}$) is constant between the two sections.

$$h_1 + w_1^2/2 - u_1^2/2 = h_{th} + w_{th}^2/2 - u_{th}^2/2 \quad (1.4)$$

Moreover, the flow is considered to be isentropic between inlet and throat sections and so also the relative total pressure and density are constant. A slightly different approach is adopted in case of supersonic entrance flow. In that situation, a normal shock is considered to occur when $M'_1 > 1$, as proposed both by Aungier and Whitlfield and Baines. The isentropic relations are then applied starting from the conditions just after the discontinuity, where the relative total temperature is equal to the upstream one but the total pressure is lower and the Mach number turned to be subsonic. Subsequently, the throat opening 'o' is computed as it would be a side of a rectangular triangle with hypotenuse the pitch 's', found as $s = \pi d_1 / N_{bl,full} - t_{bl,1}$.

$$o = s \cos \beta_{1,bl} \quad (1.5)$$

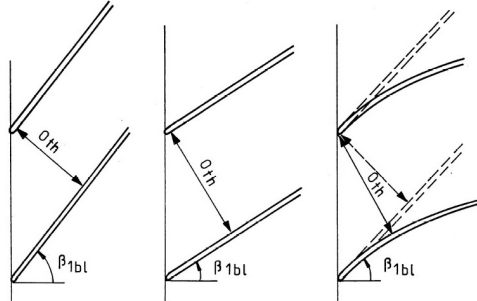


Figure 1.4: Sketch of blade throat opening

As it can be figured out from fig. (1.4), the more the blade is curved at the inlet the less accurate will be the throat estimation.

The geometrical throat area comes by $A_{th,geom} = o_{th} b_1$.

The effective flow area A_{th} results from a correction of the geometric one with a blockage factor, representing the percentage of area really available to the flow passage. Whitfield and Baines consider to be reasonable for the throat a blockage coefficient of 0.97, so that $A_{th} = 0.97 \times A_{th,geom}$.

Also the inlet area A_1 , previously indicated, has to be the effective one, therefore comprehensive of the blockage due to the blade thickness. Finally, through a mass balance, (eq. (1.3) under our assumptions turns into eq. (1.6)), the throat relative Mach number M'_{th} , the static thermodynamic properties and throat velocity w_{th} can be calculated using the Mach number relationships $w = M' \sqrt{\gamma RT}$, as in eq. (1.6)

$$\frac{M'_1 A_1 \cos \beta_1}{(1 + (\gamma - 1) M'^2_1 / 2)^{(\gamma+1)/2(\gamma-1)}} = \frac{M'_th A_{th}}{(1 + (\gamma - 1) M'^2_{th} / 2)^{(\gamma+1)/2(\gamma-1)}} \quad (1.6)$$

The expression of diffusion total pressure loss given by Aungier is reported in eq. (1.7). According to it, a dependency also on the incidence one is present, because the two phenomena have to be considered linked for an overall entrance loss.

$$\bar{\omega}_{dif} = 0.8[1 - w_{th}/w_1]^2 - \bar{\omega}_{inc} \quad \bar{\omega}_{dif} > 0 \quad (1.7)$$

1.2.3 Choking Loss

A choking condition is reached when the throat velocity reaches the sonic value. When this happens or when it's very close to happen, a choking loss is generated. The choking loss is present mainly in the off-design evaluation because in the design case this condition should be avoided. The calculation

of the sonic area A^* , the area leading to sonic velocity with fixed mass flow and static temperature, is again derived from eq. (1.6) with $M'_{th} = 1$ and then compared to the effective throat area. Aungier employs the parameter $X_{ch} = 11 - 10A_{th}/A^*$ to find the choking loss (when $X_{ch} > 0$):

$$\bar{\omega}_{ch} = \frac{1}{2}(0.05X_{ch} + X_{ch}^7) \quad (1.8)$$

1.2.4 Skin Friction Loss

One of the most common source of losses is skin friction between the fluid and the metal surfaces that Aungier recalls in eq. (1.9).

$$\bar{\omega}_{sf} = 4c_f \left(\frac{\bar{w}}{w_1} \right)^2 L_B/d_H \quad (1.9)$$

$\bar{w}^2 = \frac{w_1^2 + w_2^2}{2}$ represents the root mean square velocity.

As the majority of the experiments regarding friction were conducted in pipe flows, it is common practice to reconduct usual turbomachine passages to equivalent pipe quantities (hence hydraulic quantities) to be consistent with the data taken from them. d_H is the the hydraulic diameter which Aungier refers to as the average of the tip and throat one based on the common expression:

$$\text{hydraulic diameter} = 4 \frac{\text{cross sectional area}}{\text{wetted peremeter}} \quad (1.10)$$

The computation of the hydraulic diameters at throat follows:

$$d_{H1} = \frac{4A_{th}}{2(b_1 + s \cos \beta_1)N_{bl,full}} \quad (1.11)$$

and at tip becomes:

$$d_{H2} = \frac{4\pi d_2 b_2 / N_{bl}}{2\pi d_2 / N_{bl} + 2b_2} \quad (1.12)$$

The friction coefficient c_f is evaluated by Aungier according to the ongoing flow regime. As usual, it will depend mainly on two parameters: the Reynolds number $Re_d = \rho_1 u_2 d_H / \mu_1$ and the peak to valley surface roughness e (a value of $e = 5$ has been assumed as reference μm but the possibility to modify it has been provided in the settings file. The tip peripheral velocity u_2 has been employed for the calculation of the Reynolds number following the guidelines of the work of R. A. Van Den Braembussche [11]. If $Re_d < 2000$

the flow regime is laminar and, since roughness plays no role, the friction coefficient can be expressed by $c_f = c_{fl} = 16/Re_d$. In the transition zone (i.e. $2000 < Re_d < 4000$ instead, c_f is assessed by another equation having the laminar (c_{fl}) and turbulent (c_{ft}) friction coefficients as extreme values:

$$c_f = c_{fl} + (c_{ft} - c_{fl})(Re_d/2000 - 1) \quad (1.13)$$

When $Re_d > 4000$ the flow is turbulent but a distinction has to be pointed out between smooth and rough surfaces conditions. In reality, the surface cannot be perfectly smooth but it can thus be considered when the laminar sub-layer fully contains the roughness peaks. The turbulent smooth friction coefficient c_{fts} is modeled by

$$\frac{1}{\sqrt{4c_{fts}}} = -2\log_{10}\left[\frac{2.51}{Re_d\sqrt{4c_{fts}}}\right] \quad (1.14)$$

while the turbulent rough friction coefficient c_{ftr} value is taken from:

$$\frac{1}{\sqrt{4c_{ftr}}} = -2\log_{10}\left[\frac{e}{3.71d}\right] \quad (1.15)$$

To establish which effect roughness is playing a roughness-based Reynolds number Re_e is evaluated according to $Re_e = (Re_d - 2000)e/d$. The turbulent skin friction coefficient then becomes:

$$c_f = c_{fts} \quad Re_e < 60 \quad (1.16)$$

$$c_f = c_{fts} + (c_{ftr} - c_{fts})(60/Re_e) \quad Re_e \geq 60 \quad (1.17)$$

1.2.5 Blade Loading Loss

Another main source of loss in centrifugal compressors is represented by the blade loading, which is related to blade-to-blade pressure gradients. It is strongly dependent on the solidity, i.e. the chord to pitch ratio. In fact, given a certain force to be imparted to the fluid, correlated to the passage mass flow and tangential velocity deflection, blade loading will increase if the number or length of the blade decrease and viceversa. An excessive loading can lead to boundary layer growth and flow detachment in the impeller, causing a great amount of losses. A parameter representing the loading is the maximum velocity difference:

$$\Delta w = \frac{2\pi d_2 u_2 \lambda_B}{N_{bl,eff} L_B} \quad (1.18)$$

where λ_B is the blade work factor, $N_{bl,eff}$ is the effective number of blades and the blade mean camberline. The final pressure loss given by Aungier weights the maximum velocity difference with respect to the inlet relative one as it can be seen from eq. (1.19)

$$\bar{\omega}_{bl} = (\Delta w/w_1)^2/24 \quad (1.19)$$

1.2.6 Hub to Shroud Loss

As blade loading loss is related to pressure gradients among the blades, the hub to shroud loss is related to the presence of pressure gradients along the blade span due to radial equilibrium issues. The hub to shroud loss schematized by Aungier considers the streamline curvature $k_m = \frac{\alpha_{C2} - \alpha_{C1}}{L}$ in the meridional plane between inlet and exit of the blade, therefore referring to blade inlet and outlet velocities for the calculations in eq. (1.20)

$$\bar{\omega}_{hs} = (\bar{k}_m \bar{b} \bar{w}/w_1)^2/6 \quad (1.20)$$

α_{C1} and α_{C2} are the streamline slope angles with the axis. The inlet one is calculated in the blade inlet routine according to the input provided while, since the outlet is always perfectly radial, it will be $\alpha_{C2} = 0$. The meridional length L is approximated by $L \approx d_2/2 - (d_E/2 + r) + (r + b_1/2)(\pi/2 - \alpha_{C1})$, where r is the shroud radius of curvature of the blade at inlet.

A distinction on blade length has to be made here. Since the shape of the blade is in general fully three-dimensional, different lengths can be considered. L is the meridional length which considers the extension of the blade in the meridional plane and L_B is the blade mean camberline, evaluated on the secondary plane accounting also for the curvature due to backward orientation and inlet swirl of the blade.

1.2.7 Distortion Loss

Aungier assesses that the impeller tip meridional velocity profile distortion can be expected to contribute to a loss modelable as an abrupt expansion. The tip distortion factor ζ is:

$$\zeta = \frac{1}{1 - B_2} \quad (1.21)$$

Tip blockage B_2 is a very important parameter representing the boundary layer blockage at tip and it is comprehensive of lots of contributions (skin friction, area ratio ecc.) as it can be seen by eq. (1.22).

$$B_2 = \bar{\omega}_{sf} \frac{p_{01} - p_1}{p_{02} - p_2} \sqrt{\frac{w_1 d_H}{w_2 b_2}} + \left[0.3 + \frac{b_2^2}{L_B^2} \right] \frac{A_R^2 \rho_2 b_2}{\rho_1 L_B} + \frac{\delta_{cl}}{2b_2} \quad (1.22)$$

δ_{cl} is the clearance gap (fixed in the setting file, default 0.5 mm) applied only in case of open impellers and the area ratio A_R is defined as:

$$A_R = A_2 \cos \beta_{2,bl} / A_1 \cos \beta_{1,bl} \quad (1.23)$$

The distortion loss weights the meridional velocity component on the relative inlet velocity as expressed by eq. (1.24)

$$\bar{\omega}_{dis} = [(\zeta - 1)v_{m2}/w_1]^2 \quad (1.24)$$

1.2.8 Mixing Loss

It has been analysed that in compressors the low momentum fluid tends to concentrate in a small region on tip suction side, called wake, while the other part, called jet, is the free stream and isentropic one. Once the blade ends, the two regions mix together causing a loss due to developing drag forces. Aungier first evaluates the magnitude of the wake velocity with the estimation of the velocity at which separation occurs. This is done considering the equivalent diffusion factor $D_{eq} = \frac{w_{max}}{w_2}$, with $w_{max} = (w_1 + w_2 + \Delta w)/2$.

$$w_{sep} = w_2 \quad D_{eq} \leq 2 \quad (1.25)$$

$$w_{sep} = w_2 D_{eq}/2 \quad D_{eq} > 2 \quad (1.26)$$

The mixing involves only the meridional component of the velocity and $V_{m,mix}$ is found by

$$v_{m,mix} = v_{m2} A_2 / \pi d_2 b_2 \quad (1.27)$$

After the blade trailing edge, the available area rises as the blades thickness does not cause blockage anymore hence the meridional mix velocity will be slightly lower than V_{2m} . A_2 is the area inside blade passage at impeller exit computed as $A_2 = \pi b_2 d_2 \epsilon_2$ and $\epsilon_2 = 1 - \frac{N_{bl} t_b}{\pi d_2}$ blade blockage at exit

$$v_{m,wake} = \sqrt{w_{sep}^2 - w_{2,tg}^2} \quad (1.28)$$

The wake mixing loss, similar to another abrupt expansion loss, is given by eq. (1.29)

$$\bar{\omega}_{mix} = [(v_{m,wake} - v_{m,mix})/w_1]^2 \quad (1.29)$$

1.2.9 Clearance loss

Clearance loss applies only to open impellers as in this case flow can leak from one blade passage to another due to blade-to-blade pressure difference.

The blade pressure difference Δp_{cl} and clearance gap leaking flow will yield a total pressure loss given by eq. (1.30)

$$\bar{\omega}_{cl} = \frac{2\dot{m}_{cl}\Delta p_{cl}}{\dot{m}\rho_1 w_1^2} \quad (1.30)$$

Δp_{cl} is found by the moment of momentum variation by:

$$\Delta p_{cl} = \frac{\dot{m}(d_2 v_{2,tg} - d_1 v_{1,tg})}{N_{bl,eff} \bar{d} L} \quad (1.31)$$

u_{cl} is the flow velocity across the gap and m_{cl} is the mass leaking in the clearance is

$$u_{cl} = 0.816 \sqrt{2\Delta p_{cl}/\rho_2} \quad (1.32)$$

$$\dot{m}_{cl} = \rho_2 N_{bl,eff} s L u_{cl} \quad (1.33)$$

1.2.10 Supercritical Mach Loss

The initial acceleration of the flow on the suction surface (see fig. (1.5)) can yield to a supersonic velocity, even if the inlet one is not, causing shocks inducing also boundary layer separation. The inlet critical Mach number

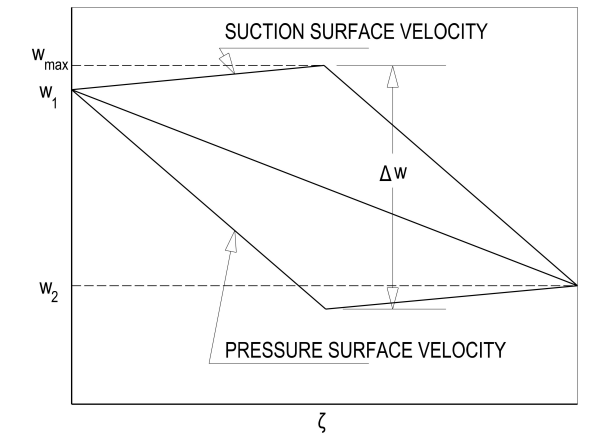


Figure 1.5: Surface velocities along the non-dimensional blade coordinate ζ

leading to that condition can be computed by $M'_{cr} = M'_1 w^*/w_{max}$. The sonic velocity w^* comes from the sound speed formula $w^* = \sqrt{\gamma R T^*}$ where the star temperature T^* at sonic condition is found using the relative total temperature and Mach number correlations:

$$T^* = T'_{01} \left(\frac{\gamma + 1}{2} \right)^{-1} \quad (1.34)$$

The supercritical Mach number loss set by Aungier is:

$$\bar{\omega}_{cr} = 0.4[(M'_1 - M'_{cr})w_{max}/w_1]^2 \quad (1.35)$$

1.2.11 Shock Loss

Whitfield and Baines report that no total pressure loss correlation for inlet shock losses are available in literature, therefore a new procedure will be adopted. As suggested by the authors, the shock is considered to be normal and this hypothesis allows to compute the thermodynamic quantities after the discontinuity using a Mach number based equations available in literature. The relative total pressure just after the normal shock p'_{SH} can be found as:

$$p'_{SH} = p'_{01} \left[\frac{(\gamma + 1)M'^2_1}{(\gamma - 1)M'^2_1 + 2} \right]^{\gamma/(\gamma-1)} \left[\frac{(\gamma + 1)}{2\gamma M'^2_1 - (\gamma - 1)} \right]^{1/(\gamma-1)} \quad (1.36)$$

From $\Delta p'_{SH}$, $\Delta p'_{01}$ will finally results.

$$\bar{\omega}_{SH} = \Delta p'_0 / (p'_0 - p)_1 \quad (1.37)$$

1.3 Parasitic Losses

External losses comprehend three different categories:

- Windage and disk friction
- Leakage
- Recirculation

1.3.1 Windage and Disk Friction

The friction occurring between the rotating disk and the stationary housing is referred to as windage and disk friction. The work done by Daily and Nece (1960) is considered by Aungier as the best source available for this source of loss. The dissertation is similar to the one for skin friction as a rotating disk in a housing for smooth and rough disks is treated. The torque coefficient is given by

$$C_M = \frac{2\tau}{\rho\omega^2 r^5} \quad (1.38)$$

where τ is the torque due to friction and ω is the rotational speed. The coefficients will depend on the flow regime existing between the boundary

layer of the disk and the one of the housing, basing the criterion again on the Reynolds number, here computed as $Re = \frac{\rho_2 \omega r_2^2}{\mu_2}$, four flow regimes are considered and for each of them a specific torque coefficient (not considering roughness yet) is set:

1. Laminar, merged boundary layers

$$C_{M1} = \frac{2\pi}{(s/r)Re} \quad (1.39)$$

2. Laminar, separate boundary layers

$$C_{M2} = \frac{3.7(s/r)^{0.1}}{\sqrt{Re}} \quad (1.40)$$

3. Turbulent, merged boundary layers

$$C_{M3} = \frac{0.08}{(s/r)^{\frac{1}{6}} Re^{\frac{1}{4}}} \quad (1.41)$$

4. Turbulent, separate boundary layers

$$C_{M4} = \frac{0.102(s/r)^{0.1}}{Re^{0.2}} \quad (1.42)$$

s is the gap between the disk and the housing and r the disk radius. A typical value of 0.02 for the s over r ratio has been taken starting from indications given by Aungier. The smooth torque coefficient C_{Ms} can be evaluated by the maximum value of the four torque coefficient and it will give an indication on which is the existing flow regime. The disk can be considered as smooth till a value of Re_s given by eq. (1.43)

$$Re_s \sqrt{C_{Ms}} = 1100(e/r)^{-0.4} \quad (1.43)$$

The Reynolds number Re_r at which roughness has no more effect is instead:

$$Re_r = 1100 \frac{r}{e} - 6 \cdot 10^6 \quad (1.44)$$

And the torque coefficient for fully rough disk is given by

$$\frac{1}{\sqrt{C_{Mr}}} = 3.8 \log_{10} \left(\frac{r}{e} \right) - 2.4 \left(\frac{s}{r} \right)^{0.25} \quad (1.45)$$

In the middle of the two regimes the torque coefficient is

$$C_M = C_{Ms} + (C_{Mr} - C_{Ms}) \log(Re/Re_s) / \log(Re_r/Re_s) \quad (1.46)$$

At this point, Aungier corrects these ideal disk torque coefficients to adapt them to centrifugal compressor, setting a correction for the clearance gap leakage flows. Denoting the previous torque friction coefficient as C_{M0} , the new torque coefficient is:

$$C_M = C_{M0}(1 - K)^2 / (1 - K_0^2) \quad (1.47)$$

Where K is the clearance gap swirl parameter and K_0 and C_q other clearance parameters

$$K = K_0 + C_q(1.75K_F - 0.316)r_2/s \quad (1.48)$$

$$K_0 = 0.46/(1 + 2s/d) \quad (1.49)$$

$$C_q = \frac{\dot{m}(\rho_2 r_2 u_2 / \mu_2)^{1/5}}{2\pi\rho_2 r_2^2 u_2} \quad (1.50)$$

For seal leakage towards the tip the impeller tip swirl parameter K_F can be evaluated by

$$K_F = v_{2t}/u_2 \quad (1.51)$$

otherwise $K_F = 0$.

The impeller disk friction torque coefficient is computed independently for the disk and the cover and the results are adjusted by:

$$C_{MD} = 0.75C_M \quad (\text{for the disk}) \quad (1.52)$$

$$C_{MC} = 0.75LC_M \left[1 - \left(\frac{d_{1e}}{d_2} \right)^5 \right] / (r_2 - r_1) \quad (\text{for the cover}) \quad (1.53)$$

and then the windage and disk friction parasitic work is obtained from:

$$\lambda_{DF} = (C_{MD} + C_{MC})\rho_2 u_2 r_2^2 / (2\dot{m}) \quad (1.54)$$

In case of uncovered impellers, the term C_{MC} is not considered.

1.3.2 Leakage Work

Another parasitic loss is represented by the leakage across the eye and shaft seals and gaps. The computation of the leakage work requires the knowledge of the seal geometry, which is typically considered as a straight-through labyrinth seal. A schematization of the seal geometry is shown in fig. (1.6)

where δ is the gap between the seal and the shaft, P is the pitch between fins, t is their thickness and N the fins number.

Once again, some typical values of these parameters are extrapolated from the books of Aungier and Ludtke, but they have been put in the settings file to let the user the possibility of modifying them. δ of 0.5 mm, a gap to thickness ratio $\delta/t = 2$ a gap to pitch $\delta/P = 0.15$ and seal pressure ratio $p_R = 0.6$ and a number of seals $N = 4$

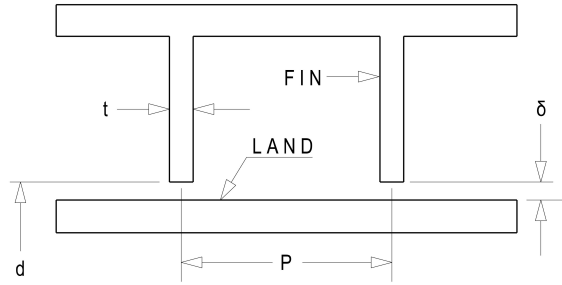


Figure 1.6: Typical geometry of a straight-through labyrinth seal

A paper from Egli (1935) provides an acceptable method to estimate the leakage. The leakage mass flow is defined as:

$$\dot{m}_L = \pi d \delta C_t C_c C_r \rho_2 \sqrt{RT_2} \quad (1.55)$$

Where ρ and T are evaluated on higher pressure side of the seal that is the tip one. Some empirical seal coefficients are present in this equation, the contraction ratio C_r :

$$C_r = 1 - \frac{1}{3 + \left[\frac{54.3}{1+100\delta/t} \right]^{3.45}} \quad (1.56)$$

The seal throttling coefficient C_t :

$$C_t = \frac{2.143[\ln(N) - 1.464]}{N - 4.322} [1 - p_R]^{0.375p_R} \quad (1.57)$$

And the carryover coefficient C_c accounting for the residual kinetic energy carried through one restriction to the next:

$$C_c = 1 + \frac{X_1[\delta/P - X_2 \ln(1 + \delta/P)]}{1 - X_2} \quad (1.58)$$

$$X_1 = 15.1 - 0.05255 \exp[0.507(12 - N)] \quad N \leq 12 \quad (1.59)$$

$$X_1 = 13.15 + 0.1625N \quad N > 12 \quad (1.60)$$

$$X_2 = 1.058 + 0.0218N \quad N \leq 12 \quad (1.61)$$

$$X_2 = 1.32 \quad N > 12 \quad (1.62)$$

$$(1.63)$$

The expression of the leakage work will depend on the impeller configuration, if it is an open or a covered one. For covered impellers, Aungier accounts for the fact that the leakage flow is worked on by the impeller a second time:

$$\lambda_L = \frac{\dot{m}_L \lambda_B}{\dot{m}} \quad \text{for covered impellers} \quad (1.64)$$

For open impellers, the assumption made is that half of the blade clearance leakage flow is reenergized by the impeller:

$$\lambda_L = \frac{\dot{m}_{cl} u_{cl}}{2u_2 \dot{m}} \quad \text{for open impellers} \quad (1.65)$$

1.3.3 Recirculation Work

Recirculation flow is related to incipient stall condition. In particular at low mass flow rate, when the load becomes high, you can expect some backflows generating wasted work. The Lieblein criterion for axial compressor with the equivalent diffusion factor D_{eq} is used to predict stall when $D_{eq} > 2$, even if most impellers can go beyond that. The recirculation work is:

$$\lambda_R = \left(\frac{D_{eq}}{2} - 1 \right) \left[\frac{w_{2t}}{v_{2m}} + 2 \tan \beta_2 \right] \quad \lambda_R \geq 0 \quad (1.66)$$

Chapter 2

Design Procedure

The design of a compressor in CCD follows a sequential path so that the analysis is carried out component after component and stage after stage, thanks to the fact that the outlet quantities of a component or stage are the inlet quantities of the next one, till the whole machine is completely solved.

The input file (see an example in fig. (2.1)) contains some mandatory specifications for the analysis such as the suction temperature T_{01} and suction pressure p_{01} , the discharge pressure $p_{0,out}$ (thus total pressure ratio β_{tot}), the mass flow rate \dot{m} , fluid properties like the specific heat ratio γ and the molecular weight \tilde{M} , and the style of the compressor (i.e. it indicates whether a compressor is for turbocharger or process application). Other quantities like the number of stages and shafts, the pressure ratio distribution among the stages, the stage flow coefficient ϕ_{01} and impeller blade exit angle $\beta_{2,bl}$ can be either selected by the user or estimated by the code as it was in the previous version. Furthermore, the user can decide to have a vaneless or vaned diffuser after the impeller, and a volute or a return system connecting the stages.

A new characteristic of the code is the distinction between shrouded or unshrouded and splitted or full blades impellers. These choices are not demanded to the user but the code makes them taking some guidelines from common practice applications. For what concerns the cover, the unshrouded impeller is set for all turbocharger compressors while process compressors feature a cover. The reason behind is that process compressors are in general multi-stage and it is more difficult to keep low clearances risking to suffer a great impact of leaking flows. The cover is applicable as long as the limit on the peripheral speed, typically around $350 - 380 \text{ m/s}$ according to Came and Robinson, is respected. By the way, the critical value of the peripheral speed not to be overcome is at discretion of the user, specifying it in a settings file like the one of fig. (2.2). If the limit is overcome, thus leading to excessive centrifugal stresses, the code switches to an unshrouded configuration.

```
-----Input parameters read by CCD (Centrifugal Compressor Code)-----
Mass_Flow_Rate_[kg/s]          29.60
Suction_Temperature_[K]         298.20
Suction_Pressure_[bar_a]        1.01
Discharge_Pressure_[bar_a]      6.33
Molecular_Weight_[kg/kmol]      29.87
isentrop_coeff_[]               1.4
viscosity_[Pa_s]                1.716e-5
T0_ref_[K]                      273.10
C_sutherland_[K]                110.4
Critical_Temperature_[K]        190.56
Critical_Pressure_[bar_a]       45.99
Total_number_of_stage_[]        3
Number_of_shaft_[]              2
StageXShaft_[]                  Sh1   Sh2   Sh3   Sh4   Sh5
Flow_coefficient[]              0.107 0.098 0     0     0
                               S1    S2    S3    S4    S5    S6    S7    S8    S9    S10
Intercooler_[]                  1     1     0     0     0     0     0     0     0     0
Reinj_Temperature[K]            304   305   0     0     0     0     0     0     0     0
pressure_drop[%]                2.5   2.5   0     0     0     0     0     0     0     0
Pressure_ratio_[]               2.163 1.749 1.726 0     0     0     0     0     0     0
Shape_factor_[]                 0.88  0.91  0.93  0     0     0     0     0     0     0
Beta_2_bBlade_[deg]             -40   -40   -40   -40   -40   -40   -40   -40   -40   -40
-----DIFFUSER-----
Vaned_Diffuser[y/n]             S1    S2    S3    S4    S5    S6    S7    S8    S9    S10
                               1     0     0     0     0     0     0     0     0     0
-----VOLUTE-----
volute[y/n]                     S1    S2    S3    S4    S5    S6    S7    S8    S9    S10
                               1     1     1     0     0     0     0     0     0     0
-----RETURN SYSTEM-----
Return_System[y/n]               S1    S2    S3    S4    S5    S6    S7    S8    S9    S10
                               0     0     0     0     0     0     0     0     0     0
-----STYLE OF COMPRESSOR-----
style      process
```

Figure 2.1: Example of input file for CCD

Similarly, splitted blades are applied to all turbocharger applications and to process compressors with stage pressure ratios higher than two, as suggested again by Came and Robinson, in order to limit the losses at the inlet due to a high incoming relative velocity w_1 limiting blade blockage.

Starting from the first stage, with the initial assumption of the total work factor λ and the isentropic efficiency η_{is} , the analysis develops with the computation of the peripheral Mach number M_{u2} (defind as $M_{u2} = \frac{u_2}{\sqrt{\gamma RT_{0,in}}}$) from the adimensionalised energy equation, function also of the stage pressure ratio β :

$$M_{u2} = \sqrt{\frac{\beta^{\frac{\gamma-1}{\gamma}} - 1}{(\gamma - 1)\lambda\eta_{is}}} \quad (2.1)$$

which immediately allows to find the peripheral velocity u_2 from eq. (2.2)

$$u_2 = M_{u2} \sqrt{\gamma RT_{01}} \quad (2.2)$$

At this point the procedure is different depending whether we are dealing with a first stage of a shaft or a successive one (refer to fig. 2.3 and fig. 2.4).

```

-----SETTING PARAMETERS for CCD-----
-----Impeller Parameters-----
roughness actual[micron]      5
roughness reference[micron]    5
clearance_gap/r2              0.00637
throat blockage                0.97
delta/de                       0.002
delta/t                         2
delta/p                         0.15
seal number N                  4
p_r                             0.6
s/r2                           0.02
-----Blade inlet routine parameters-----
K_birdi_1                      0.28
K_birdi_2                      0.8
t_b/d2 shrouded                 0.01
t_b/d2 unshrouded               0.003
-----Vaneless diffuser-----
r4/r2 min                       1.55
-----Vaned diffuser-----
Nvane-Nb1                        -4
thickness/r3                     0.03
incidence[deg]                  -0.5
AR min                           1.4
AR max                           2.4
divergence min                  7
divergence max                  10.5
Load min                         0.15
Load max                         0.33
-----Volute-----
position                          external
SP                               1
cut off angle[deg]              320
exit cone divergence            10.5
exit cone AR                     2.3
wall thickness/r5               0.02
W/H                             1.7
-----Return system-----
incidence[deg]                  2
relative thickness               0.03
alpha C7[deg]                   -45
-----Other paramters-----
convergence factor               0.2
vane loading                      0.5
shroud limit[m/s]                370
min_pinching                      0.7
s/c                                0.4

```

Figure 2.2: Example of settings file for CCD in which characteristical parameters of the impeller, of the vaned and vaneless diffuser, of the return system and volute can be selected

In the first case the inlet flow coefficient ϕ_{01}

$$\phi_{01} = \frac{\dot{V}_{01}}{u_2 d_2^2} \quad (2.3)$$

(being \dot{V}_{01} the total volumetric flow rate calculated as $\dot{V}_{01} = \frac{\dot{m}}{\rho_{01}}$) is fixed and the rotational speed N has to be found. In the other case, instead, N is a constraint imposed by the first stage and ϕ_{01} is a result. The discharge temperature $T_{0,out}$ is found rewriting the definition of total work factor $\lambda = \frac{c_p(T_{0,out} - T_{0,in})}{u_2^2}$, so that:

$$T_{0,out} = T_{0,in} + u_2^2 \frac{\lambda}{c_p} \quad (2.4)$$

An additional guess, on λ , is needed since its value will be known at the end of the impeller procedure.

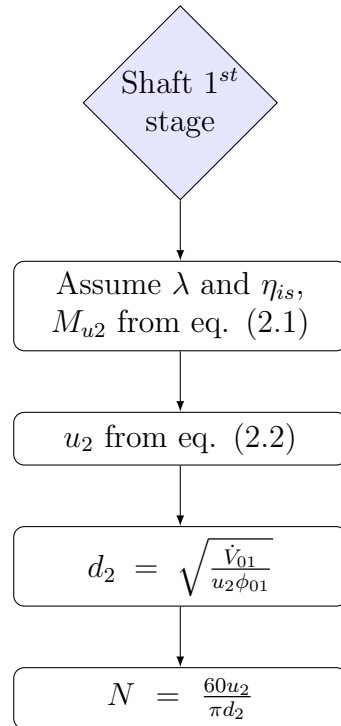


Figure 2.3: Initial design procedure in case of first stage of a shaft

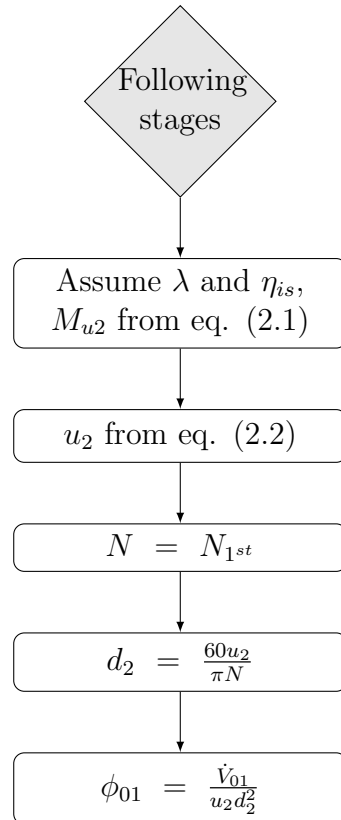


Figure 2.4: Initial design procedure in case of following stages

2.1 Impeller Inlet

A simplification is introduced to define the geometry of the impeller: as sketched in fig. (2.5), the region between the eye and the blade is supposed to be built with circular arcs, where r and R are respectively the shroud and hub radius of curvature. r is taken interpolating reference mean shroud radii of curvature values given by Ludtke:

$$2r/d_2 = \begin{cases} 0.13 & \text{when } 0 < \phi_{01} \leq 0.05 \\ 0.23 & \text{when } 0.05 < \phi_{01} \leq 0.1 \\ 0.35 & \text{when } 0.1 < \phi_{01} \leq 0.2 \end{cases} \quad (2.5)$$

and $R = r + b_1$, being b_1 the inlet blade height. Bezier curves are then employed to link blade inlet to the tip.

The inlet area A_1 can be expressed as:

$$\begin{aligned} A_1 &= \pi d_{1m} b_1 \epsilon_1 \\ &= \epsilon_1 \pi (r_{1s}^2 - r_{1h}^2) / \cos \alpha_{c1} \\ &= \epsilon_1 \frac{\pi}{4} k_1 d_{1s}^2 / \cos \alpha_{c1} \end{aligned} \quad (2.6)$$

With d_{1m} is indicated the exact mean diameter at blade inlet and ϵ_1 is the inlet blade blockage obtained by eq. (2.23).

Under all these assumptions, referring also to fig. (2.6), the blade inlet streamline flow angle α_{c1} results from geometrical considerations:

$$\frac{d_e}{2} + r - \frac{d_{1m}}{2} = \left(\frac{d_e}{2} + r - \frac{d_m}{2} \right) \cos \alpha_{c1} \quad (2.7)$$

$$\alpha_{c1} = \cos^{-1} \left(\frac{d_e/2 + r - d_1/2}{d_e/2 + r - d_m/2} \right) \quad (2.8)$$

The blade hub and shroud diameters d_{1h} and d_{1s} can be written as:

$$d_{1h} = d_{1m} - b_1 \cos \alpha_{c1} = \frac{d_{1m}}{d_e} d_e - \left(\frac{d_e - d_h}{2} \right) \cos \alpha_{c1} \quad (2.9)$$

$$d_{1s} = d_{1m} + b_1 \cos \alpha_{c1} = \frac{d_{1m}}{d_e} d_e + \left(\frac{d_e - d_h}{2} \right) \cos \alpha_{c1} \quad (2.10)$$

An important parameter influencing inlet geometry is the shape factor $k = 1 - \frac{r_h^2}{r_e^2}$. When the possibility of choosing it in the input is taken by the user, a suggested range is $0.5 < k < 0.95$ in order to guarantee a feasible stiffness to the shaft. r_h and r_e refer to eye and hub of the machine (defining

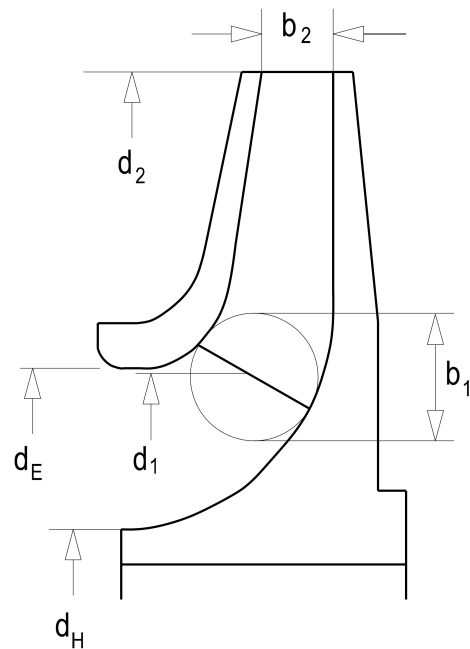


Figure 2.5: Section of a generic impeller of a centrifugal compressor

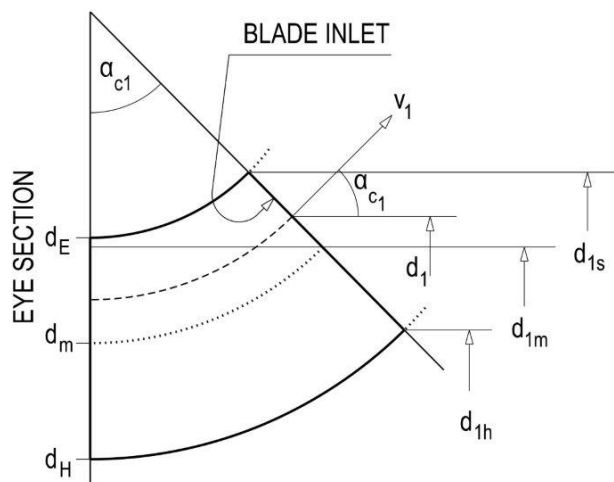


Figure 2.6: Zoom of the region between eye of the compressor and blade inlet

inlet blade height $b_1 = \frac{d_e - d_h}{2}$) while hub and shroud coordinate at blade inlet are represented by r_{1h} and r_{1s} . With the relationship $\frac{d_h}{d_e} = \sqrt{1 - k}$ it becomes:

$$d_{1h} = d_e \left(\frac{d_{1m}}{d_e} - \left(1 - \sqrt{1 - k} \right) \frac{\cos \alpha_{c1}}{2} \right) \quad (2.11)$$

$$d_{1s} = d_e \left(\frac{d_{1m}}{d_e} + \left(1 - \sqrt{1 - k} \right) \frac{\cos \alpha_{c1}}{2} \right) \quad (2.12)$$

through which the blade shape factor $k_1 = 1 - \frac{d_{1h}^2}{d_{1s}^2}$ can be calculated as:

$$k_1 = 1 - \frac{\left(\frac{d_1}{d_e} - \left(1 - \sqrt{1 - k} \right) \frac{\cos \alpha_{c1}}{2} \right)^2}{\left(\frac{d_1}{d_e} + \left(1 - \sqrt{1 - k} \right) \frac{\cos \alpha_{c1}}{2} \right)^2} \quad (2.13)$$

It is important to say that the blade inlet meanline coordinate that is considered for the 1D analysis do not refer to the exact mid coordinate but to the root mean square value that is:

$$d_1 = \sqrt{\frac{d_{1s}^2 + d_{1h}^2}{2}}$$

The value of $\frac{d_{1m}}{d_e}$ is recommended by Lüdtke according once again to the inlet flow coefficient, varying from 0.78 for cases with $\phi_{01} > 0.11$ to 1.12 for $\phi_{01} < 0.016$.

It's a common good design practice to minimize, for a given flow rate, the blade shroud relative velocity w_{1s} (which means minimizing also the shroud relative Mach number M'_{1s}) always following the aim of loss reduction. As done also in the previous version of CCD, the same minimization algorithm proposed by Casey and Rusch is adopted here. Even if the basic hypothesis of zero incidence, uniform inlet velocity profile with no swirl have been kept, some corrections are introduced to account for the effects of blade blockage ϵ_1 and the discrepancy between blade inlet and eye section, as that algorithm refers originally to high-flow capacity compressors configurations in which these sections are practically coincident.

The characteristic equations by Casy-Rusch are eq. (2.14) and eq. (2.15).

$$4 \frac{\phi_{01} M_{u2}^3}{\pi k} = \frac{M_{1s}'^3 \sin^2 \beta_{1s} \cos \beta_{1s}}{\left(1 + \frac{\gamma-1}{2} M_{1s}'^2 \cos^2 \beta_{1s}\right)^{1/(\gamma+1)+3/2}} \quad (2.14)$$

$$\cos \beta_{1s,opt} = \frac{\sqrt{3 + \gamma M_{1s}'^2 + 2M_{1s}'}}{2M_{1s}'} \quad (2.15)$$

with β_{1s} representing the relative flow angle at shroud. Corrections apply only to eq.(2.14) but they will be collected in coefficient k so to maintain the same shape of the equation.

The main term in Casey-Rusch equation is a non-dimensional mass flow function $\Phi = M_{u2}\phi_{01}$ which can be expressed, using the definitios of M_{u2} , ϕ_{01} , \dot{m} and some geometrical ones, as:

$$\begin{aligned} \Phi &= \frac{\dot{m}}{\rho_{01} a_{01} d_2^2} \\ &= \frac{\rho_1 A_1 v_{1m}}{\rho_{01} a_{01} d_2^2} \\ &= \frac{\rho_1}{\rho_{01} \cos \alpha_{c1}} \frac{\epsilon_1}{4} k_1 \frac{d_{1s}^2}{d_2^2} \frac{v_{1m}}{a_{01}} \\ &= \frac{\rho_1}{\rho_{01}} \frac{\pi}{4} k_{eq} \frac{u_{1s}^2}{u_2^2} \frac{v_{1m}}{a_{01}} \end{aligned} \quad (2.16)$$

Exploiting the definitions $v_{1m} = w_{1s} \cos \beta_{1s}$ and $u_{1s} = w_{1s}$ and the Mach relationships between total and static quantities we can arrive at:

$$\Phi = k_{eq} \frac{\pi}{4} \frac{M_{1s}'^3}{M_{u2}^2} \frac{\sin^2 \beta_{1s} \cos \beta_{1s}}{\left(1 + \frac{\gamma-1}{2} M_{1s}'^2 \cos^2 \beta_{1s}\right)^{1/(\gamma+1)+3/2}} \quad (2.17)$$

Thanks to an equivalent term $k_{eq} = \frac{\epsilon_1}{\cos \alpha_{c1}} k_1$ eq. (2.17) has the same structure of eq. (2.14):

$$4 \frac{\phi_{01} M_{u2}^3}{\pi k_{eq}} = \frac{M_{1s}'^3 \sin^2 \beta_{1s} \cos \beta_{1s}}{\left(1 + \frac{\gamma-1}{2} M_{1s}'^2 \cos^2 \beta_{1s}\right)^{1/(\gamma+1)+3/2}} \quad (2.18)$$

so that the equation can be treated equally to the one by Casey and Rusch.

The algorithm is solved with the Newton's method and the outputs M_{1s}' and $\beta_{1s} = \beta_{1s,opt}$ permit to reconstruct the velocity triangles and compute the thermodynamic quantities.

The blade shroud relative Mach number M'_{1s} is simply related to the absolute one M_1 through a trigonometric relationships thanks to the assumptions of the model. Together with the already known suction quantities (assumed to remain the same till blade inlet) and the gas state equation it is possible to evaluate the static quantities at blade inlet:

$$\begin{aligned} M_1 &= M'_{1s} \cos \beta_{1s,opt} & T_1 &= T_{01} \left(1 + \frac{\gamma - 1}{2} M_1^2 \right)^{-1} \\ p_1 &= p_{01} \left(1 + \frac{\gamma - 1}{2} M_1^2 \right)^{-1} & \rho_1 &= \frac{p_1}{ZRT_1} \end{aligned}$$

Z represents the compressibility factor to account for the real gas behaviour, as implemented in the previous version of CCD, and it is calculated from the generalised Nelson-Obert chart according to the specific values of reduced pressure and temperature.

Successively, the velocity triangle at shroud can be found:

$$w_{1s} = M'_{1s} \sqrt{\gamma RT_1} \quad u_{1s} = w_{1s} \sin \beta_{1s,opt} \quad v_1 = M_1 \sqrt{\gamma RT_1}$$

leading to the calculation of blade huband shroud diameters:

$$d_{1s} = 60 \frac{u_{1s}}{\pi N} \quad d_{1h} = d_{1s} \sqrt{1 - k}$$

The other velocity triangles, using the fact that v_1 is fully meridional, result from:

$$\begin{aligned} u_{1h} &= \pi \frac{N}{60d_{1h}} & w_{1h,t} &= -u_{1h} & w_{1h} &= \sqrt{v_1^2 + w_{1h,t}^2} \\ u_1 &= \pi \frac{N}{60d_1} & w_{1t} &= -u_1 & w_1 &= \sqrt{v_1^2 + w_{1t}^2} \end{aligned}$$

with the inlet relative flow angle $\beta_1 = \cos^{-1}(v_1/w_1)$.

The relative total quantities at inlet are then found using the Mach number relationships starting from the static quantities:

$$\begin{aligned} T'_{01} &= T_1 \left(1 + \frac{\gamma - 1}{\gamma} M_1' \right) \\ p'_{01} &= p_1 \left(1 + \frac{\gamma - 1}{\gamma} M_1' \right)^{\frac{\gamma}{\gamma-1}} \\ \rho'_{01} &= \rho_1 \left(1 + \frac{\gamma - 1}{\gamma} M_1' \right)^{\frac{1}{\gamma-1}} \end{aligned}$$

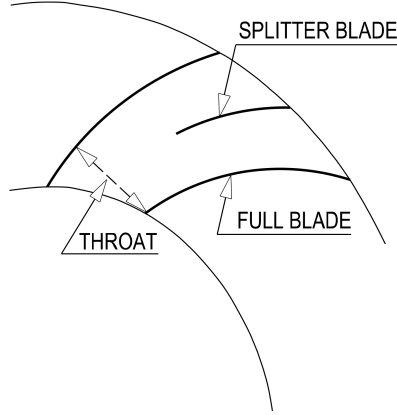


Figure 2.7: Representation of full and splitted blades

The axial length of the compressor is calculated from Birdi's equation:

$$\frac{L_{ax}}{d_2} = \sqrt{k_1(M'_{1s} + k_2)(1 - d_{1m}/d_2)(d_{1s} - d_{1h})/d_2} \quad (2.19)$$

from which the axial length comes from immediately.

The number of blades is computed from a formula by Stodola reported in 'Teoria delle Turbomacchine' by Osnaghi [32].

$$N_{bl} = \frac{2\pi \cos \bar{\beta}}{s/c \log(d_2/d_1)} \quad (2.20)$$

$\bar{\beta}$ is the mean average blade angle $\bar{\beta} = \frac{\beta_1 + \beta_2}{2}$ and s/c represents the pitch to chord ratio. According to Eckert, a reasonable value of s/c is 0.4 as it normally varies between 0.35 and 0.45, but the choice of this parameter is left to the user in the settings file so that there is some freedom on the estimation of the number of blades. It has to be pointed out that the blade number N_{bl} is rounded just after all the calculations are done. The reason behind this choice is that the round to integer number can cause discontinuity between one loop and another may leading to numerical instability, as encountered in some cases, while with this method the passage is gradual.

Since the impeller can be equipped with splitted blades (see fig. (2.7)), Aungier uses eq. (2.21) to determine the equivalent number of blades $N_{bl,eq}$

$$N_{bl,eq} = N_{bl,full} + N_{bl,sp} \frac{L_{SP}}{L_{FB}} \quad (2.21)$$

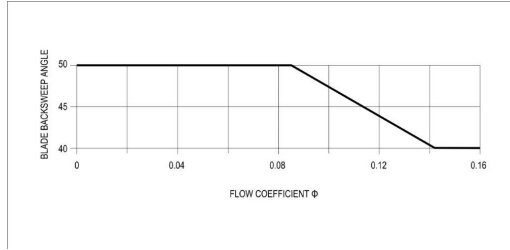


Figure 2.8: Variation of $\beta_{2,bl}$ with inlet flow coefficient ϕ as suggested by Ludtke

where L_{SP} and L_{FB} represent the splitter and full blade length respectively. It is assumed that the length of splitter blades is half the full blade one (approximately it varies between 0.5 and 0.75).

Moreover, the blade thickness t_b is supposed uniform all along the blade, as in a 1D model philosophy, but two different values are set depending on the configuration of the impeller:

$$t_b = \begin{cases} 0.003 \cdot d_2 & \text{for uncovered impellers} \\ 0.01 \cdot d_2 & \text{for covered impeller} \end{cases} \quad (2.22)$$

the relationship for uncovered impellers by Came and Robinson sets a blade thickness of 0.3% of the tip diameter d_2 , instead Ludtke suggestions of $t_b = 1\%$ of d_2 are followed for covered impellers where a higher thickness is required to withstand the additional stresses caused by the cover.

In all this procedure a first guess of the blade blockage

$$\epsilon_1 = 1 - \frac{t_b N_{bl,full}}{\pi d_1 \cos \beta_1} \quad (2.23)$$

and streamline flow angle α_{cl} is needed and all the procedure is repeated until the check on continuity is met.

2.2 Impeller Outlet

The blade exit angle $\beta_{2,bl}$ remains an input parameter of CCD and only when the user has not specified the number of stages it is estimated from a correlation based on the inlet flow coefficient, as reported in fig. (2.8),

The slip factor σ is taken from the well known Weisner relationship:

$$\sigma = 1 - \frac{\sqrt{\cos \beta_{2,bl}}}{N_{bl,eq}^{0.7}} \quad (2.24)$$

but according to Aungier a correction has to be applied in case the parameter $\epsilon = d_1/d_2$ overcomes the limit imposed by $\epsilon_{lim} = \frac{\sigma - \sigma^*}{1 - \sigma^*}$ with $\sigma^* = \sin(19\pi/180 + 0.2(\pi/2 + \beta_2))$ and the corrected slip factor becomes

$$\sigma_{corr} = \sigma \cdot \left[1 - \left(\frac{\epsilon - \epsilon_{lim}}{1 - \epsilon_{lim}} \right)^{(90+\beta_{2,deg})/10} \right] \quad (2.25)$$

Through rothalpy conservation the relative total temperature at outlet can be found from eq. (2.26):

$$T'_{02} = T'_{01} - \frac{u_1^2 - u_2^2}{2c_p} \quad (2.26)$$

The impeller outlet velocity triangle is found first guessing the exit flow coefficient ϕ_2 , defined as $\phi_2 = \frac{\dot{m}}{\rho_2 A_2 u_2}$.

According to Aungier, the good matching between the impeller and the diffuser relies on the impeller exit flow angle α_2 , with different values if the following diffuser is vaneless or vaned. In case of a vaneless diffuser, α_2 is suggested by eq. (2.27). $\phi_{01,aung}$ is the inlet flow coefficient according to Aungier convention, that is $\phi_{01,aung} = \frac{4}{\pi}\phi_{01}$.

$$\alpha_2 = \pi/2 - \tan^{-1}(0.26 + 3\phi_{01,aung}) \quad (2.27)$$

For a vaned diffuser, instead, it becomes

$$\alpha_{2,deg} = 72^\circ - 0.5 \ln \phi_{01,aung} - 585 \phi_{01,aung}^2 \quad (2.28)$$

The velocity triangle (of fig. 2.9) can then be constructed as:

$$\begin{aligned} w_{2m} &= \phi_2 \cdot u_2 & w_{2t} &= v_{2t} - u_2 & w_2 &= \sqrt{w_{2m}^2 + w_{2t}^2} \\ v_{2m} &= w_{2m} & v_{2t} &= v_{2m} \cdot \tan \alpha_2 & v_2 &= \sqrt{v_{2m}^2 + v_{2t}^2} \end{aligned}$$

The ideal flow angle $\beta_{2\infty}$ of the ideal relative velocity $w_{2\infty}$ is not equal to $\beta_{2,bl}$ because Aungier refers to w_2 as the velocity just after the end of the blades, where distortion effect, represented by ζ , is already applied.

The blade work factor, with the assumption of no inlet swirl, is deduced from eq. (2.29)

$$\lambda_B = \frac{v_{2t}}{u_2} \quad (2.29)$$

The static temperature results from the discharge temperature T_{02} :

$$T_2 = T_{02} - \frac{v_2^2}{2c_p} \quad (2.30)$$

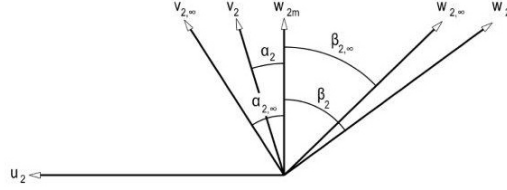


Figure 2.9: Exit velocity triangle, subscript ∞ refers to no slip condition

through which Mach numbers can be determined:

$$M_2 = \frac{v_2}{\sqrt{\gamma RT_2}} \quad M'_2 = \frac{w_2}{\sqrt{\gamma RT_2}} \quad (2.31)$$

Considering the geometry at the exit section, the blade blockage is computed as $\epsilon_2 = 1 - \frac{N_{blt_b}}{\pi d_2}$. In this case only the effect of the blade thickness is considered because the blade angle is already a parameter accounted in the blockage factor B_2 .

Exploiting the two definitions of flow coefficients in eq. (2.32) and eq. (2.33) and isolating the common term of the mass flow

$$\dot{m} = \phi_{01} \rho_{01} u_2 d_2^2 \quad (2.32)$$

$$\dot{m} = \phi_2 \rho_2 u_2 A_2 \quad (2.33)$$

the exit blade height b_2 is deduced, by matching the two equations and expliciting the exit passage area $A_2 = \pi \epsilon_2 d_2 b_2$:

$$b_2 = \frac{\phi_{01} \rho_{01}}{\phi_2 \rho_2} \frac{d_2}{\pi \epsilon_2} \quad (2.34)$$

Loss computation The definition of total pressure loss coefficient $\bar{\omega}$ is:

$$\bar{\omega} = \frac{\Delta p_0}{(p_0 - p)_{in}} \quad (2.35)$$

Summing all the impeller loss coefficients, the total pressure loss coefficient $\bar{\omega}_{tot}$ is calculated and the real relative total pressure can then be found as:

$$p'_{02} = p'_{02,id} - f_c(p'_{01} - p_1) \bar{\omega}_{tot} \quad (2.36)$$

$p_{02,id}$, as shown in fig. (2.10), is referred to by Aungier as the ideal relative total pressure that would be reached, in an isentropic transformation, having

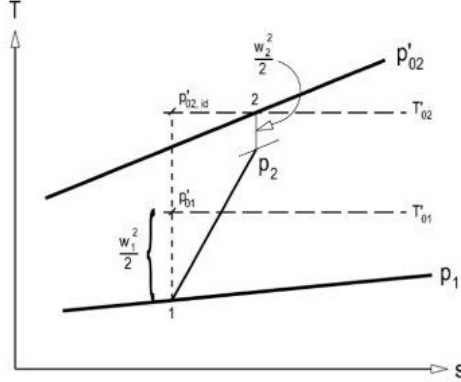


Figure 2.10: Thermodynamic diagram representative of the transformation occurring across the impeller

the same final relative total temperature T'_{02} :

$$p'_{02,id} = p'_{01} \left(\frac{T'_{02}}{T'_{01}} \right)^{\frac{\gamma}{\gamma-1}} \quad (2.37)$$

Aungier employs the correction factor f_c because the losses are calculated as a difference in total pressure weighted on the inlet conditions but applied at the outlet. f_c is evaluated as $f_c = \frac{T'_{02}\rho'_{02}}{T'_{01}\rho'_{01}}$ to scale the loss difference depending on the magnitude ratio between p'_{02} and p'_{01} .

Together with the relative total temperature T'_{02} , the Mach numbers are used to link the thermodynamic quantities. The static pressure at impeller exit p_2 is calculated with:

$$p_2 = p'_{02} \left(1 + \frac{\gamma - 1}{2} M'_2 \right)^{-1} \quad (2.38)$$

The same procedure allows to find the absolute total pressure at impeller discharge:

$$p_{02} = p_2 \left(1 + \frac{\gamma - 1}{2} M_2 \right) \quad (2.39)$$

Once also the exit blockage B_2 is found with eq. (1.22), the value of ϕ_2 can be calculated by crossing two definitions given by Aungier:

$$\frac{w_{2m}}{u_2} = \phi_2 \quad (2.40)$$

$$\frac{w_{2m}}{u_2} = \frac{\sigma(1 + \zeta\phi_2 \tan \beta_{2,bl})}{\tan \alpha_2} \quad (2.41)$$

Finally, the flow coefficient ϕ_2 can be expressed as:

$$\phi_2 = \frac{\sigma}{\tan \alpha_2 - \sigma \zeta \tan \beta_{2,bl}} \quad (2.42)$$

The parasitic losses are then computed as explained in the previous chapter so that the total work factor λ is recalculated with eq. (2.43):

$$\lambda = \lambda_B + \lambda_{par} \quad (2.43)$$

where $\lambda_{par} = \lambda_{DF} + \lambda_L + \lambda_R$ is the parasitic work.

2.3 Diffuser design

In a centrifugal compressor, the diffuser plays a crucial role in the recovery of static pressure from the high kinetic energy stream leaving the impeller. This component can consist in a vaneless annular space (named therefore vaneless diffuser) or can be characterized by cascades or wedges (vaned diffuser). Once again, Aungier modelling has been followed both for the vaneless diffuser and the vaned one, whose choice is set as a preference of the user in the input file.

2.3.1 Vaneless Diffuser

The vaneless diffuser modeled is a constant width diffuser type. Four governing equations (tangential and meridional momentum, gas state and energy equation) plus some auxiliary ones are employed by Aungier to fully characterize the vaneless diffuser (but also more generally are valid for vaneless spaces such as also the cross over bend). The aim is to directly integrate such equations from inlet to exit to find outlet quantities, considering when necessary mean values along the passage. Moreover, the same perfect gas assumption made for the impeller (even if corrected for the compressibility effect) is kept also here. The equations are:

- Continuity

$$\pi d \rho b v_m (1 - B) = \dot{m} \quad (2.44)$$

- Tangential momentum with friction

$$b v_m \frac{d(r v_t)}{dm} = -r v \cdot v_t c_f \quad (2.45)$$

- Meridional momentum

$$\frac{1}{\rho} \frac{dp}{dm} = \frac{v_t^2 \sin \alpha_C}{r} - v_m \frac{dv_m}{dm} - \frac{c_f v \cdot v_m}{b} - \frac{d\lambda_D}{dm} - \lambda_C \quad (2.46)$$

- Total enthalpy

$$h_T = h + \frac{1}{2} v^2 \quad (2.47)$$

λ_D and λ_C are two loss terms related to diffusion and curvature loss respectively. The diffusion loss term λ_D is obtainable from eq. (2.48)

$$\frac{d\lambda_D}{dm} = -2(p_0 - p)(1 - E) \frac{1}{\rho v} \frac{dv}{dm} \quad (2.48)$$

where E represents the diffusion efficiency (its value is extrapolated from eq. (2.51)), and the curvature loss is:

$$\lambda_C = k_m(p_0 - p)v_m/(13\rho v) \quad (2.49)$$

In an annular diffuser the diffusion loss term will be predominant while in a cross-over bend the second one will. It has to be noticed that, in the radial vaneless diffuser, the infinitesimal meridional coordinate dm will become the radial coordinate dr .

Since no total pressure loss coefficients are present in this analysis, the performance of the vaneless diffuser derives directly from the computed outlet absolute total pressure p_{05} .

At first, a consideration has to be made: the three pivotal quantities in vaneless diffuser sizing are the diffuser outlet radius r_5 , the diffuser exit absolute angle α_5 and the passage width b_5 . It is important to say that it is not possible to impose a value for all of them otherwise the problem will be over-constrained. As the walls are parallel, the width will be constant all along the passage, so that the exit width $b_5 = b_2$. The next decision is to set the diffuser exit radius r_5 so, consequently, the diffuser outlet flow angle α_5 is an output of the equations after being assumed at the beginning. The numerical subscripts are taken equal to the ones of the vaned diffuser where the exit section is station 5.

The choice of the diffuser exit radius is crucial for the effectiveness of this component: a too low exit radius will not lead to a satisfactory pressure

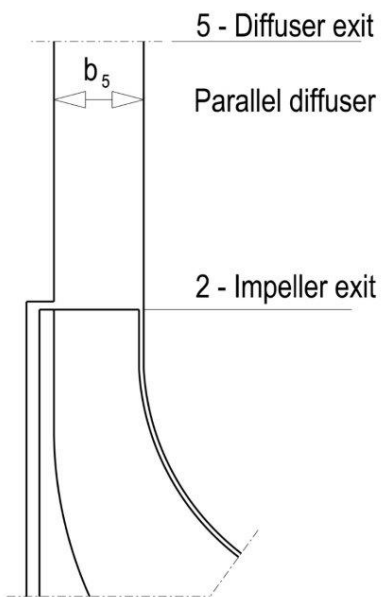


Figure 2.11: Sketch of impeller followed by a parallel wall diffuser

recovery process while a too high radius will cause excessive losses due to friction in the channel. Therefore Aungier estimates an optimal value of the exit radius r_5 with eq. (2.50)

$$r_5 = \left(\frac{r_5}{r_2} \Big|_{min} + \frac{4}{\pi} \phi_{01} \right) r_2 \quad (2.50)$$

$\frac{r_5}{r_2} \Big|_{min}$ represents the minimum radii ratio of the diffuser, that can be defined in the settings file, and its typical value stands around 1.55 in order to guarantee a good operation of the diffuser. The diffuser length is $L = r_5 - r_2$ and the area ratio is simply $A_R = \frac{r_5}{r_2}$.

The divergence parameter $D = b_2(A_R - 1)/L$ is one of the most characteristical parameters in a diffusion process. Comparing it to a reference value $D_m = 0.4(b_2/L)^{0.35}$, the diffusion efficiency E term is computed and used in eq. (2.48)

$$E = \begin{cases} 1 & \text{when } D \leq 0 \\ 1 - 0.2(D/D_m)^2 & \text{when } 0 < D < D_m \\ 0.8\sqrt{D_m/D} & \text{when } D \geq D_m \end{cases} \quad (2.51)$$

Aungier uses a simple boundary layer growth model to estimate the blockage at diffuser inlet and outlet through the boundary layer thickness 2δ . The inlet boundary layer thickness $2\delta_{in}$ is related to impeller friction coefficient c_f and blade mean camberline L_B :

$$2\delta_{in} = 5.142c_f L_B \quad (2.52)$$

The relationship allowing to find boundary layer thickness at outlet is:

$$rv_t = rv_{te}[1 - 2\delta/(4.5b)] \quad (2.53)$$

which links the edge angular momentum rv_{te} , constant along the passage as referred to the free stream, to the meanline angular momentum rv_t . Therefore eq. (2.53) will lead to $2\delta_{out}$ under the constraint $2\delta \leq b$, since at maximum $2\delta_{out}$ equals the passage width.

Boundary layer blockage comes from eq. (2.54)

$$B = \frac{2\delta}{8b} \quad (2.54)$$

The procedure starts with the calculation of the tangential velocity at diffuser exit from eq. (2.45)

$$v_{4t} = \frac{r_2}{r_4} v_{2t} \cdot \exp(-c_f L / (b_4 \cos \bar{\alpha})) \quad (2.55)$$

from which the meridional velocity derives.

$$v_{5m} = \frac{v_{5t}}{\tan \bar{\alpha}} \quad (2.56)$$

From eq. (2.46) the static pressure at exit p_4 is calculated and so is for the static density ρ_4 , with the gas equation of state $\frac{p}{\rho} = ZRT$. If continuity at station 5 is not satisfied, a new iteration begins (with the new values of α_5 and v_{m5}) till a satisfactory tolerance is met.

The stability of the diffuser is guaranteed by the proper selection of diffuser inlet flow angle α_2 , consequence of the good design practice suggested by Aungier for the impeller design.

2.3.2 Vaned Diffuser

The second type of diffuser is the vaned one. As Aungier states, a vaned diffuser can sustain higher inlet flow angles without the risk of stall thanks to the guidance of the vanes. The advantage in this case is the use of larger passage widths to reduce the friction losses. Therefore, it is particularly suited for low flow coefficient compressors while for high flow coefficients it loses effectiveness. On the other hand, the presence of vanes will penalize the performances at off-design conditions, because it will impose a smaller range of operation.

Aungier model of the vaned diffuser is again based on some pivotal parameters, such as the area ratio A_R , the divergence angle $2\theta_C$ and blade loading parameter L that will be later discussed. As done for all vaned components, flow calculations are performed at three reference sections: vane inlet, vane exit and throat. The vaned regions, as shown in fig. (2.12), stands between two vaneless spaces, one just after the impeller and the other before the entrance of the next component, being a volute or a return system. The first vaneless space is usually pinched, i.e. the two walls are not parallel, while the second is straight.

Anugier supplies formulas for optimal vane inlet flow angle α_3 , which depends from:

$$\alpha_3 = \begin{cases} 72^\circ + \frac{\alpha_2 - 72^\circ}{4} & \text{when } \alpha_2 \geq 72^\circ \\ 72^\circ & \text{when } \alpha_2 < 72^\circ \end{cases}$$

and vane leading edge r_3 refers to eq. (2.57):

$$\frac{r_3}{r_2} = 1 + \frac{90 - \alpha_3}{360} + \frac{M_2^2}{15} \quad (2.57)$$

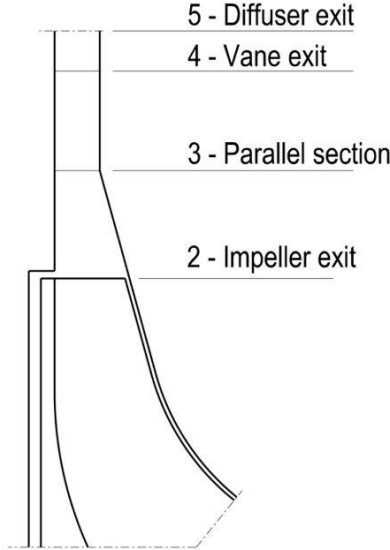


Figure 2.12: Sketch of impeller followed by a vaned diffuser

Section 2-3 The vaneless space between impeller exit and vane inlet should be not too low, to make the distorted flow more homogeneous, but not too high to avoid long flow paths.

In order to guarantee a reasonable measure of b_3 , which is the geometrical quantity that allows to set α_3 to the desired value, an upper limit of $b_3 = b_2$, to avoid detrimental diverging channels, and a lower limit of $b_3 = \frac{b_3}{b_2}|_{min} \cdot b_2$ (with $\frac{b_3}{b_2}|_{min}$ decided by the user), not to undergo an excessive pinching, are imposed. If the limits are exceeded, all the calculations are done considering a simplified case with $b_3 = b_2$.

In order not to repeat the dissertation, the procedure explained for the vaneless diffuser is applied also here to get the thermodynamic and flow quantities at section 3. Once section 2-3 is properly solved the vane region 3-4 starts to be analysed.

Section 3-4 From the flow angle found in the previous section and the desired incidence angle (imposed in the settings file with a default optimal value $i = -0.5$) the blade vane angle $\alpha_{3,bl}$ is calculated as $\alpha_{3,bl} = \alpha_3 - i$.

Regarding the vane number N_{vd} , Aungier relates it to the impeller number of blades N_{bl} by referring to the relative difference, $N_{vd} - N_{bl}$, that is possible to choose in the settings file. As Aungier prescribes the use of low solidity

thick vanes diffusers, N_{vd} will be usually lower than N_{bl} . Also here the vane thickness t_{vd} is found in relative terms, with respect to inlet radius r_3 and set by the designer.

The throat area calculation will be provided by some auxiliary equations given by Aungier. The throat angle $\cos \alpha_{th}$ comes from:

$$\cos \alpha_{th} = \cos^2 \alpha_3 / \cos \alpha_{3,bl} \quad (2.58)$$

The ideal passage throat area $A_{th,id}$ follows:

$$A_{th,id} = A_3 \cos \alpha_{th} \quad (2.59)$$

While the blockage is evaluated from a contraction ratio C_r calculated using $C_r = \sqrt{\frac{A_3 \cos \alpha_{3,bl}}{A_{th,id}}}$, indicating with A_3 passage area at vane inlet. The effective throat area can be obtained as $A_{th} = C_r A_{th,id}$ from which results the throat opening $h_{th} = \frac{A_{th}}{N_{vd} b_3}$.

To compute throat thermodynamic quantities the same procedure used for the impeller is applied also here.

The maximum extension of the blades $r_{4,max}$, which is equal to vaned diffuser outlet radius r_5 , follows eq. (2.50)

Three characteristic parameters for the vaned diffuser are the divergence θ_C , the aforementioned area ratio A_R and the blade loading L :

$$2\theta_C = \frac{2 \tan^{-1} \left[\frac{(w_4 - t_{vd})b_4}{b_3} - w_3 + t_{vd} \right]}{2L_B} \quad (2.60)$$

with $\tan \theta_C = \frac{\pi(r_4 \cos \alpha_{4,bl} - r_3 \cos \alpha_{3,bl})}{L_B}$ and $w_4 = \frac{2\pi r \cos \alpha_{4,bl}}{N_{vd}}$.

The area ratio A_R here becomes:

$$A_R = \frac{r_4 \cos \alpha_{4,bl}}{r_3 \cos \alpha_{3,bl}} \quad (2.61)$$

and the vane loading L

$$L = \frac{\Delta v}{v_3 - v_4} \quad (2.62)$$

where $\Delta v = \frac{2\pi(r_3 V_{t3} - r_4 V_{t4})}{N_{vd} L_B}$

Aungier states that the optimal ranges for these parameters are:

- $2\theta_C$

$$7^\circ < 2\theta_C < 11^\circ$$

- A_R

$$1.4 < A_R < 2.4$$

- L

$$0 < L < 0.33$$

being the upper limits for $2\theta_C$ and A_R the optimal values. The procedure suggested by Aungier is to start from these best conditions and, as soon as the constraints on r_4 and L are respected, stop the analysis.

The discharge blockage factor is:

$$B_4 = \frac{(k_1 + k_2(C_R^2 - 1))L_B}{w_4} \quad (2.63)$$

with parameters:

$$C_R = \frac{1}{2} \frac{v_{m3} \cos \alpha_{4,bl}}{v_{m4} \cos \cos \alpha_{3,bl}} + 1 \quad (2.64)$$

$$k_1 = 0.2 \left(1 - \frac{1}{C_L C_\theta} \right) \quad (2.65)$$

$$k_2 = \frac{2\theta_C}{125C_\theta} \left(1 - \frac{2\theta_C}{22C_\theta} \right) \quad (2.66)$$

Aungier employs correction coefficients C_L and C_θ in case the optimal ranges of L and $2\theta_C$ are not respected, as the user can modify in the settings the extreme limits beyond them.

Similarly to the impeller, the total pressure losses accounted for the vaned diffuser are:

- Incidence
- Skin friction
- Mixing
- Choking

The incidence loss is found as:

$$\bar{\omega}_{inc} = 0.8 \left(\frac{v_3 - v_{3,th}}{v_3} \right)^2 + \left(\frac{N_{vd} t_{vanes}}{2\pi r_3} \right)^2 \quad (2.67)$$

Skin friction follows:

$$\bar{\omega}_{sf} = \frac{4c_f (\bar{v}/v_3)^2 L_B}{d_H} / \left(\frac{2\delta}{d_H} \right)^{0.25} \quad (2.68)$$

The mixing loss is:

$$\bar{\omega}_{mix} = \left(\frac{v_{m,wake} - v_{m,mix}}{v_3} \right)^2 \quad (2.69)$$

which comes from the same procedure applied for the impeller.

$$\begin{aligned} v_{3,sep} &= \frac{v_3}{1 + 2C_\theta} & v_{3,sep} > v_4 \\ v_{m,wake} &= \sqrt{v_{sep}^2 - v_{4t}^2} & v_{4,mix} = \frac{A_4 v_{m4}}{2\pi t_{vd} b_4} \end{aligned}$$

And finally the choking loss:

$$\bar{\omega}_{ch} = \begin{cases} 0.5(0.05X + X^7) & \text{if } X > 0 \\ 0 & \text{if } X < 0 \end{cases}$$

As said for the impeller, choking occurs when $C_r A_{th} = A^* = \frac{\dot{m}}{\rho^* V^*}$.

The vane angle at discharge, $\alpha_{4,bl}$, is extracted from vane length L_B estimation as:

$$\cos^{-1} \left(\frac{2(r_4 - r_3)}{L_B} - \cos \alpha_{3,bl} \right) \quad (2.70)$$

The discharge flow angle follows Howell's work for axial compressors:

$$\alpha_4 = \alpha_{4,bl} - \delta^* - \frac{\partial \delta}{\partial i} (\alpha_{3,bl} - \alpha_3).$$

The minimum deviation angle δ^* is:

$$\delta^* = \frac{\theta \left(0.92 \left(\frac{a}{c} \right)^2 + 0.02 \alpha_{4,bl} \right)}{\sqrt{\sigma} - 0.02\theta} \quad (2.71)$$

where a/c is the maximum camber point:

$$\frac{a}{c} = \frac{2 - \frac{\bar{\alpha}_{bl} - \alpha_{3,bl}}{\alpha_{4,bl} - \alpha_{3,bl}}}{3} \quad (2.72)$$

The solidity σ is defined as:

$$\sigma = N_{vd}(r_4 - r_3) / (2\pi r_3 \cos \bar{\alpha}_{bl}) \quad (2.73)$$

and finally the camber $\theta = \alpha_{4,bl} - \alpha_{3,bl}$

The variation of the deviation angle with incidence $\frac{\partial \delta}{\partial i}$ can be computed, according to the model, as:

$$\frac{\partial \delta}{\partial i} = \exp \left[\left(\left(1.5 - \frac{90 - \alpha_{3,bl}}{60} \right)^2 - 3.3 \right) \sigma \right] \quad (2.74)$$

The vane length can be approximated from eq. (2.75):

$$L_B \sim \frac{2r_3(R-1)}{\cos \alpha_{3,bl} + \cos \alpha_{4,bl}} \quad (2.75)$$

considering the radii ratio $R = \frac{r_4}{r_3}$.

Once the analysis of the vanes is completed, a vaneless space with parallel walls is supposed to be present between r_4 and r_5 , and the now well known analysis for vaneless spaces is followed to compute the exit flow properties.

2.4 Stage exit

The last component of a compressor stage, after the impeller and the diffuser, can consist in a volute or in a return system. They are two alternative components, meaning that they cannot be simultaneously present in the layout of the same stage. Usually, the return system connects stages positioned on the same shaft while the volute is employed to bring the flow out of the machine, as required in the last stage or in intercooled stages, but the preference can be selected in the input file.

According to Aungier, they are the two least understood and less analysed components under the point of view of a 1D methodology, due to the complex flow field developing across them. Nonetheless, to consider the not negligible losses, a performance model and design approach have been provided by the author and they will be therefore used as a reference.

2.4.1 Return System

A specific routine for the return system has been implemented in Matlab code CCD, based on the procedure reported in [1]. The return system is composed by two elements: the cross-over bend (a vaneless space featuring a 180° turn) and the return channel (a vaned region accomodating the flow to be directed into the eye of the next stage). In fig. (2.13) the shape of the considered return system is highlighted.

The good dimensioning suggested by Aungier means a proper scaling of geometric quantities, accomplished also through an optimal set of flow and blade angles.

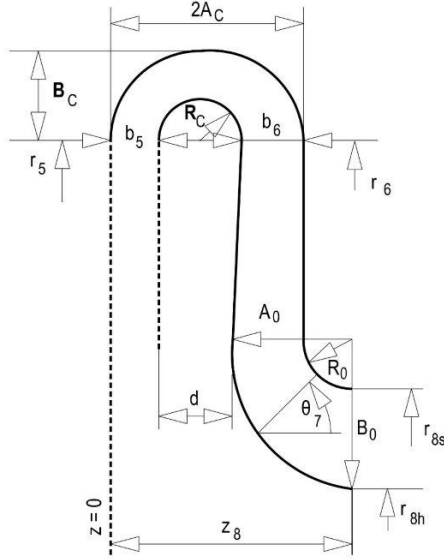


Figure 2.13: General shape of a return system

Cross-over bend

A vaneless passage analysis will be performed across the bend. The exit flow angle α_6 is computed through:

$$\alpha_6 = \frac{\pi}{2} - \tan^{-1}(0.32 + \frac{6.8}{\pi}\phi_{01}) \quad (2.76)$$

The contour of the cross-over bend is circular for the hub (with radius of curvature R_C) and elliptical for the shroud (A_C and B_C are the semi-axes) and they will be found as:

$$R_c = \frac{b_5 + b_6}{2} \quad (2.77)$$

$$A_c = R_c + \frac{b_5 + b_6}{2} \quad (2.78)$$

$$B_c = R_c + b_5 \quad (2.79)$$

where b_5 and b_6 represent the passage widths at inlet and outlet of the cross-over bend. In order not to have too large difference between the two, that can lead to flow detachment at section 6, a limit of $b_6 \leq 2b_5$ is imposed. To complete the geometry of the bend, the lengths of the cross-over contours

L_{CO} are calculated as a semi-circumference for the hub and as an arc of ellipse for the shroud:

$$L_{CO,h} = \pi R_c \quad (2.80)$$

$$L_{CO,s} \simeq \pi \sqrt{2(A_c^2 + B_c^2)} \quad (2.81)$$

The mean streamline value for the cross-over length L_{CO} is taken, repeating what done for impeller's inlet diameter, as a root mean square value of the two.

The governing equations of the vaneless space analysis, eq. (2.44) to eq. (2.47), here become:

- Tangential Momentum

$$bv_m \frac{d(rv_t)}{dm} = -rv \cdot v_t c_f \quad (2.82)$$

After integration it results:

$$\ln\left(\frac{v_{t6}}{v_{t5}}\right) = -\frac{c_f L_{CO}}{\bar{b} \cos \bar{\alpha}} \quad (2.83)$$

- Meridional Momentum

α_C is the mean streamline angle and in the cross-over bend it is null since $\alpha_{C5} = \frac{\pi}{2}$ and $\alpha_{C6} = -\frac{\pi}{2}$ and so $\sin \bar{\alpha}_C = 0$. Under our hypothesis and expressing the diffusion and curvature loss terms λ_D and λ_C , eq. (2.46) can be rewritten as:

$$\begin{aligned} \frac{1}{\gamma \bar{M}^2} \frac{dp}{p} &= \frac{dv}{v} \cos^2 \bar{\alpha} - c_f \frac{\cos \bar{\alpha}}{\bar{b}} dm + 2Z \left(\left(1 + \frac{\gamma-1}{2} \bar{M}^2 \right)^{\frac{\gamma}{\gamma-1}} - 1 \right) (1-E) \frac{1}{\gamma \bar{M}^2} \frac{dv}{v} \\ &\quad - \frac{Z k_m \left(\left(1 + \frac{\gamma-1}{2} \bar{M}^2 \right)^{\frac{\gamma}{\gamma-1}} - 1 \right) \cos \bar{\alpha}}{13\gamma \bar{M}^2} dm \end{aligned} \quad (2.84)$$

with passage curvature $k_m = \frac{\pi}{L_{CO}}$

Considering that $\int_5^6 dm = L_{CO}$, eq. (2.84) will be integrated to find the only unknown, that is the exit static pressure p_6 .

v_{6t} is gained through eq. (2.83) and with discharge flow angle also v_6 . Hence, the static temperature T_6 comes from eq. (2.47). Finally, the density is calculated with the equation of state and then the passage width b_6 from continuity.

Return Channel

The return channel is divided in two parts: the vanes and the final turn into the eye of the next stage. The location of mean radius r_7 , representing vane discharge, is approximated by $r_{8,s}$, whereas vane inclination θ at section 7 is set as a default option to $\theta = 45^\circ$. Both hub and shroud contours at final turn will be arcs of circumference. Instead, the profile of the channel between cross-over bend and final turn is perfectly radial for the shroud while the hub one is inclined, in order to accommodate for the passage width increase as shown in fig. (2.13).

With an optimum value of incidence i indicated around 4° , the blade angle $\alpha_{6,bl}$ can be obtained. Discharge blade angle $\alpha_{7,bl}$, instead, is imposed to 0° . Aungier employs Howell's deviation model for axial compressor to find the flow angle α_7 , but this methodology is useful for off-design evaluation as at design point $\alpha_7 = \alpha_{7,bl}$ can be assumed.

The calculation of the areas comprehends:

- Inlet area A_6

$$A_6 = 2\pi r_6 b_6 (1 - B_{6,metal}) \quad (2.85)$$

Blade blockage $B_{6,metal}$ depends on the vanes number and thickness.

- Throat area A_{th}

$$A_{th} \approx (2\pi r_6 - N_{vc} t_v) b_6 \cos \alpha_6 \quad (2.86)$$

N_{vc} is the vane number and t_{vc} is the vane thickness, taken $t_{vc} = 0,04 \cdot r_6$ to scale it with the radius and make the vane quite thick as considered by Aungier and Lüdtke. No aerodynamic blockage is added at exit also because the thickness is considered homogeneous in this 1D approach but at exit is thinner than at inlet.

- Exit vane area A_7

$$A_7 = (2\pi r_7 - N_{vc} t_{vc}) b_7 \quad (2.87)$$

b_7 is the passage width at the end of the vanes.

- Return channel exit area A_8

$$A_8 = \pi(r_{8s}^2 - r_{8h}^2) = \pi k r_{8s}^2 \quad (2.88)$$

k and r_{8s} are respectively the shape factor and the eye radius of the next stage.

Losses of Return Channel The losses are computed in terms of total pressure loss coefficient $\bar{\omega}$ based on the inlet condition at station 6

$$\bar{\omega} = \frac{p_{06} - p_{07}}{p_{06} - p_6} \quad (2.89)$$

- Incidence loss

$$\bar{\omega}_{inc} = 0.8 \left(1 - \frac{v_{m6}}{v_6 \cos \alpha^*} \right)^2 \quad (2.90)$$

The optimal incidence angle α_6^* is assumed to occur when the flow inlet angle is equal to the one at vane throat.

$$\alpha_6^* = \frac{\pi}{2} - \tan^{-1} \left[(1 - B_6) \tan(\arcsin \frac{A_{th}}{A_6}) \right] \quad (2.91)$$

indicating with B_6 the aerodynamic blockage, taken as the maximum value between

$$B_6 = 1 - \frac{b_5}{b_6} \quad B_6 = \frac{(k_m b_6)^2}{12 + (k_m b_6^2)} \quad (2.92)$$

- Skin friction loss

$$\bar{\omega}_{sf} = 4c_f \left(\frac{\bar{v}}{v_6} \right)^2 L_B / d_H + \frac{|\alpha_{C6} - \alpha_{C7}| v_{6m} v_{7m}}{13 v_6^2} \quad (2.93)$$

d_H is the hydraulic diameter found as an average between throat and vane exit and α_{C7} is equal to $-\theta$.

- Blade loading loss

$$\bar{\omega}_{bl} = (\Delta v / v_6)^2 / 6 \quad (2.94)$$

with $\Delta v = \frac{2\pi(r_6 v_{6t} - r_7 v_{7t})}{N_{vc} L_B}$

The number of vanes N_v is obtained from a criterion that imposes the loading by fixing the velocity ratio $\frac{2\Delta v}{v_6 + v_7}$ to a certain value (lower than 0.7 as recommended by Aungier) with $\Delta v = 2\pi r_6 v_{6t} / (N_{vc} L_B)$, considering no tangential component at 7 and being $L_B = \frac{2(r_6 - r_7)}{\cos \alpha_{6,bl} + \cos \alpha_{7,bl}}$ the mean camberline. It has been chosen 0.5 by default in the settings.

- Mixing loss

$$\bar{\omega}_{mix} = \left(\frac{v_{m,wake} - v_{m,mix}}{v_6} \right)^2 \quad (2.95)$$

The meridional velocities of the wake and after mixing are estimated from:

$$v_{m,wake} = \sqrt{v_{sep}^2 - v_{7t}^2} \quad v_{m,mix} = \frac{v_{7m} A_7}{2\pi r_7 b_7}$$

- Exit turn loss

In case vane exit exit is not already axial, is accounted as another total pressure loss coefficient including friction and curvature contributions:

$$\bar{\omega}_{ex} = \left(4c_f + \frac{1}{13} \right) |\alpha_{c7}| \left(\frac{v_{m7}}{v_6} \right)^2 \quad (2.96)$$

Aungier also adds the choking loss to this model but since it is very rare to happen in the return channel it has been preferred not to consider it.

Since stage exit area A_8 depends, as reported in eq. (2.88), on the unknown eye radius of next stage, it has been decided to solve the issue by making the hypothesis that r_{8s} will be very close to blade shroud radius r_{1s} of the next stage. In this way, the blade inlet velocity triangle can be considered to relate return channel exit velocity v_8 to the eye radius through the peripheral velocity, since the rotational speed is already set. In fact, as the shroud relative angle of next stage β_{1s} will be around -60° (this is a typical value indicated by many authors among which Aungier and Whitfield and Baines) through some useful correlations (eq. (2.97) to eq. (2.99)) the value of r_{8s} will result:

$$u_{1s} = v_8 \tan \beta_{1s} \quad (2.97)$$

$$u_{1s} = \frac{\pi N r_{8s}}{30} \quad (2.98)$$

$$r_{8s} = \frac{30 v_8 \tan \beta_{1s}}{\pi N} \quad (2.99)$$

So that by substituting this expression in the continuity equation $\dot{m} = \rho_8 v_8 A_8$ it can be found that

$$v_8 = \sqrt[3]{\frac{\dot{m} \pi}{\rho_8 k \left(\frac{30 \tan \beta_{1s}}{N} \right)^2}} \quad (2.100)$$

The hub radius r_{8h} is computed with k and r_{8s} , noticing that passage width b_7 , equal to b_8 , follows as $b_7 = r_{8s} - r_{8h}$.

Of course, the proper procedure to compute eye and blade section will be applied when the analysis shifts to the next stage, but it is expected not move away too much from these calculations.

2.5 Volute

The final volute plays the important role of collecting the flow, which is continuously evolving radially through the machine, and guide it in the desired direction. In order to do that, in opposition to the other elements of the compressor, the velocity component contributing to the throughflow is the tangential one. The meridional velocity, instead, will become a swirl component, as shown in fig. (2.17), that will be dissipated along the passage.

Aungier deals with an asymmetric volute, that is a volute where the diffuser passage is not centered with respect to volute-cross section (see again fig. (2.17)). A general shape of a volute is shown in fig. (2.17)

The collection process starts from a section called tongue and then it evolves angularly with the collection angle θ . The mean radius of the cross section, r_c , is a characteristic parameter of the volute. According to its evolution with θ , it is possible to distinguish between external volutes (fig. (2.14)), in which r_c increases with θ , semi-external volutes (fig. (2.15)), when r_c remains constant, and internal volutes (see fig. (2.16)), if r_c decreases with θ . Even if the preferable choice, when possible, is to pick an external volute configuration to help the flow slowing down, the designer can decide in the settings file which configuration to adopt. The geometry of the cross-section is circular for the external and semi-external layouts and only in case of the internal volute a rectangular one is set, to guarantee more geometrical flexibility varying the aspect ratio W/H when space constraints become more important.

The volute analysis is conducted in three important stations: cut-off, full collection and exit cone station. Cut-off is the section where the flow passage stops curving and it becomes straight while full collection is where the collection of the flow is completed (during this process the area is increasing proportionally to θ to accomodate the new incoming flow rate). The final exit cone in fig. (2.18) is a diffuser which slows down the flow once again.

Another important feature for the design of a volute is the sizing parameter SP , which is calculated as the ratio between the tangential momentum at inlet and outlet as:

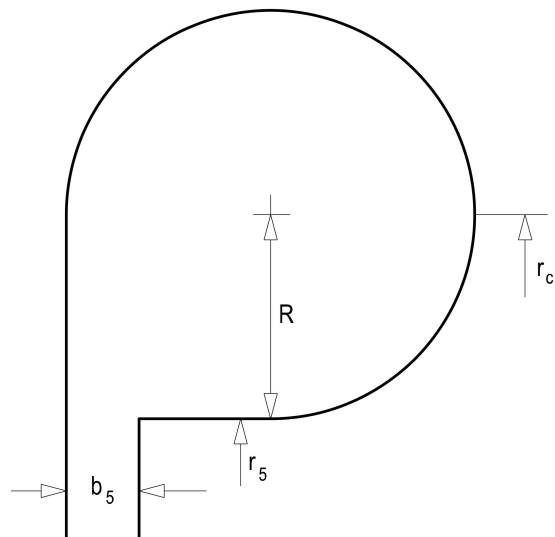


Figure 2.14: Geometry of a circular external volute

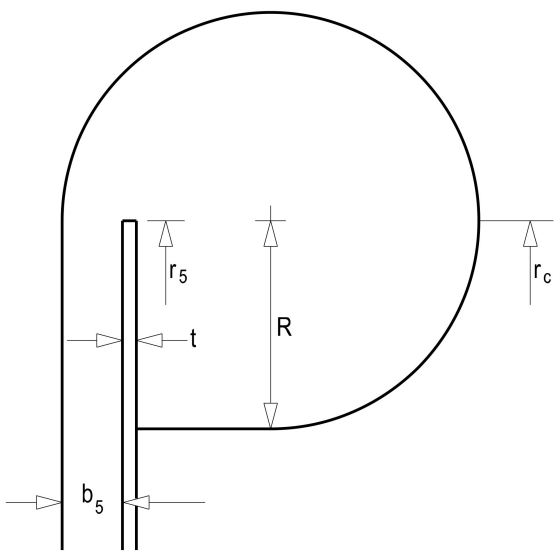


Figure 2.15: Geometry of a circular semi-external volute

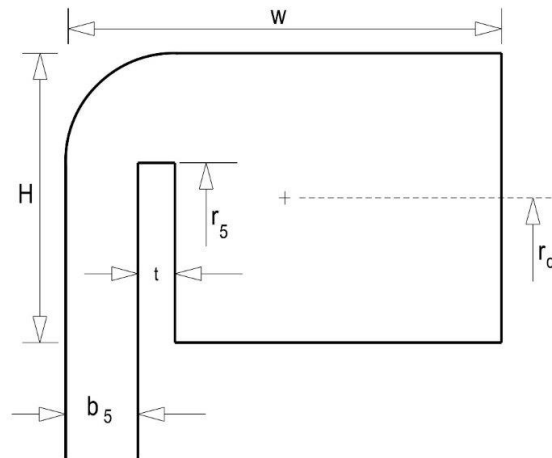


Figure 2.16: Geometry of a rectangular internal volute

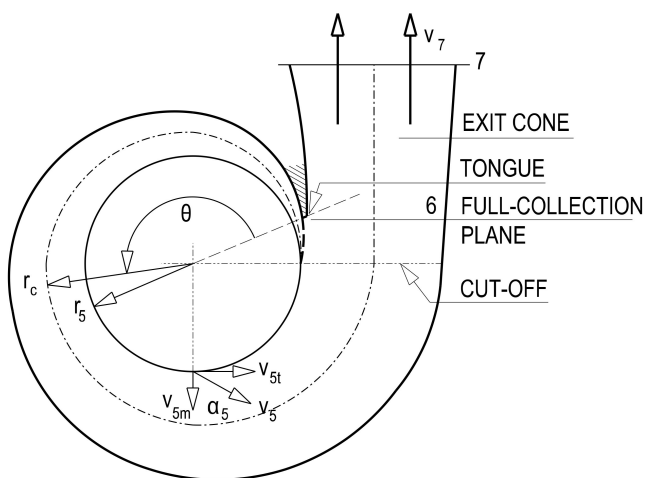


Figure 2.17: General Shape of the volute

$$SP = \frac{r_5 v_{t5}}{r_6 v_6} \quad (2.101)$$

It expresses the ratio of the actual volute area to the value satisfying the ideal conservation of angular momentum. Typical values range from 1-1.2 but also for this option the user will have the decision. SP is also employed as a correction factor to take into account distorted velocity profiles, viscous effects and secondary flows.

In his model, Aungier considers the hypothesis of incompressible fluid (sustainable since the Mach number in this component is low) and no volute inlet blockage. Therefore, continuity becomes:

$$vA(\theta) = \theta \cdot (rbv_m)_5 \quad (2.102)$$

On the contrary, in CCD density variation and diffuser exit blockage effects are taken into account so that continuity is properly respected. Hence, eq. (2.102) becomes:

$$\rho v A(\theta) = \theta \cdot (\rho rbv_m)_5 (1 - B_5) \quad (2.103)$$

With this approach and using the definition of SP , the cut-off area can be calculated as:

$$A_{6,cut-off} = \frac{\theta_{cut-off} r_6 b_5 SP \rho_5 (1 - B_5)}{\tan \alpha_5 \rho_6} \quad (2.104)$$

considering a mass flow increasing linearly with the collection angle θ , A_6 will be then simply found as:

$$A_6 = \frac{2\pi r_6 b_5 SP \rho_5 (1 - B_5)}{\tan \alpha_5 \rho_6} \quad (2.105)$$

With the area varying between cut-off section and full-collection one, it is possible to keep constant the flow velocity in the passage and so also the tangential velocity momentum ratio because the radial coordinate is the same.

Loss Model Aungier delivers a simple set of loss correlations both for the volute and for the final exit cone.

- Meridional velocity loss

The coefficient corresponds to a complete loss of the meridional component

$$\bar{\omega}_m = \left(\frac{v_{m5}}{v_5} \right)^2 \quad (2.106)$$

- Tangential velocity loss

The loss of the tangential velocity will be dependent on the sizing parameter

$$\bar{\omega}_{tg,vol} = \begin{cases} 0.5 \frac{r_5 V_{t5}^2}{r_6 V_5^2} \left(1 - \frac{1}{SP^2}\right) & \text{when } SP \geq 1 \\ \frac{r_5 V_{t5}^2}{r_6 V_5^2} \left(1 - \frac{1}{SP}\right)^2 & \text{when } SP < 1 \end{cases} \quad (2.107)$$

- Skin friction loss

Skin friction losses are directly proportional to the passage length L and inversely to the hydraulic diameter d_H

$$\bar{\omega}_{sf} = 4c_f \left(\frac{v_6}{v_5}\right)^2 L/d_H \quad (2.108)$$

with $L = \pi(r_5/r_6)/2$ and $d_H = \sqrt{4A_6/\pi}$.

Taking advantage of the total pressure loss relationship, eq. (2.109), the total pressure at full collection plane p_{06} is determined.

$$p_{06} = p_{05} - \bar{\omega}_{vol}(p_{05} - p_5) \quad (2.109)$$

The analysis needs a guess on volute exit velocity v_6 so to be able to compute the static temperature $T_6 = T_{02} - \frac{v_6^2}{2c_p}$ and the Mach number $M_6 = \frac{v_6}{\sqrt{\gamma R T_6}}$ from which the static pressure can be found:

$$p_6 = p_{06} \left(1 + \frac{\gamma - 1}{2} M^2\right)^{-1} \quad (2.110)$$

The next step is to compute the static density with which the exit velocity can be recalculated: $v_6 = \frac{\dot{m} \theta_{cut-off}}{2\pi\rho_6 A_6}$

- Exit cone loss The exit cone loss comes from:

$$\bar{\omega}_{ec} = \left(\frac{v_6 - v_7}{v_5}\right)^2 \quad (2.111)$$

The final exit cone (look at fig. (2.18)) is like an exhaust diffuser and consequently the typical diffuser parameters, such as divergence angle $2\theta_c$, area ratio A_R and length L , are used to size it. $2\theta_c$ and the A_R are set to optimal values if no external constraints are present, so $2\theta_c = 10, 5^\circ$ and $A_R = 2.3$ but also these ones are setting provided by the user. The same procedure of station 6 is then used to find the thermodynamic quantities at exit cone outlet.

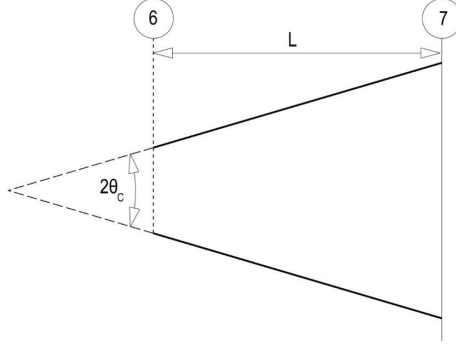


Figure 2.18: Exit cone

2.6 Stage performance

Once the stage total pressure $p_{0,out}$ has been computed either from the volute or return system models, the isentropic efficiency η_{is} of the stage is calculated as:

$$\eta_{is} = \frac{\left(\frac{p_{0,out}}{p_{01}}\right)^{(\gamma-1)/\gamma} - 1}{\frac{T_{02}}{T_{01}} - 1} \quad (2.112)$$

Moreover, considering the polytropic transformation

$$\frac{p_{02}}{p_{01}} = \left(\frac{T_{02}}{T_{01}}\right)^{\frac{n_p}{n_p-1}} \quad (2.113)$$

the polytropic exponent n_p is obtained, leading also to the polytropic efficiency:

$$\eta_p = \frac{n_p}{\gamma} \frac{\gamma - 1}{n_p - 1} \quad (2.114)$$

In order to attenuate numerical instability effects in the main efficiency loop, a relaxation factor ϵ is employed when computing the new value:

$$\eta_{is} = \epsilon \eta_{is,new} + (1 - \epsilon) \eta_{is,old} \quad 0 < \epsilon < 1 \quad (2.115)$$

It is clear that the value of ϵ will affect the velocity of the design calculations, the more $\epsilon \rightarrow 0$ the more it will be slow, but with values around 0.4

it is possible in many cases to avoid problems of convergency without losing so much time.

The performances of the whole machine are evaluated stacking the contribution of all the n stages, so to calculate the ideal, the real and the polytropic heads of the compressor:

$$\Delta h_{0,id} = \frac{\gamma Z_{in} RT_{0,in}}{\gamma - 1} \left(\beta_{tot}^{\frac{\gamma-1}{\gamma}} - 1 \right) \quad (2.116)$$

$$\Delta h_{0,real} = \sum_{i=1}^n \left[\frac{\gamma \bar{Z}_i RT_{0,in(i)}}{\gamma - 1} \left(\left(\frac{p_{0,out(i)}}{p_{0,in(i)}} \right)^{\eta_{p(i)}(\gamma-1)/\gamma} - 1 \right) \right] \quad (2.117)$$

$$\Delta h_{0,p} = \sum_{i=1}^n \left[\frac{\gamma \eta_{p(i)} \bar{Z}_i RT_{0,in(i)}}{\gamma - 1} \left(\left(\frac{p_{0,out(i)}}{p_{0,in(i)}} \right)^{\eta_{p(i)}(\gamma-1)/\gamma} - 1 \right) \right] \quad (2.118)$$

These computations lead to the isentropic and polytropic efficiency of the whole compressor:

$$\eta_{is,comp} = \frac{\Delta h_{0,id}}{\Delta h_{0,real}} \quad \eta_{p,comp} = \frac{\Delta h_{0,p}}{\Delta h_{0,real}} \quad (2.119)$$

2.7 Geometry Plot

Even if only preliminary, the compressor's design plot can be useful to give the designer an idea of the layout of the machine, that will be later refined with more sophisticated tools. Therefore, the sketch of the compressor, as the one reported in fig. (2.19), is made utilising the geometrical design quantities previously calculated.

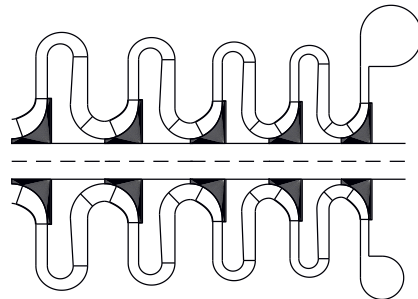


Figure 2.19: Example of the layout of a five stage compressor as generated by CCD

2.8 Output File

The most important design results are collected in a separate .txt file, regarding some stage parameters plus more detailed quantities about the components. An example of output with just the stage parameters is reported in fig. (2.20)

-----STAGE PARAMETERS-----						
	S1	S2	S3	S4	S5	S6
Design Quantities						
The polytropic efficiency of the stage is:	0.814	0.807	0.799	0.790	0.782	0.785
The isoentropic efficiency of the impeller is:	0.893	0.888	0.882	0.873	0.866	0.859
The isoentropic efficiency of the stage is:	0.812	0.805	0.797	0.788	0.779	0.783
The flow coefficient of the stage is:	0.027	0.026	0.024	0.022	0.020	0.020
The surge flow coefficient of the stage is:	0.013	0.012	0.011	0.010	0.010	0.009
The tip Mach Number of the stage is:	0.246	0.246	0.246	0.250	0.251	0.249
The Suction Temperature of the stage is:	298.0	303.1	308.3	313.6	319.1	324.7
The Discharge Temperature of the stage is:	303.1	308.3	313.6	319.1	324.7	330.5
The Suction Pressure of the stage is:	51.00	53.51	56.14	58.90	61.79	64.83
The Discharge Pressure of the stage is:	53.51	56.14	58.90	61.79	64.83	68.02
The pressure ratio of the stage is:	1.049	1.049	1.049	1.049	1.049	1.049
The total work factor of the stage is:	0.702	0.708	0.714	0.697	0.704	0.711
The blade work factor of the stage is:	0.654	0.656	0.658	0.636	0.637	0.639
The parasitic work of the stage is:	0.048	0.052	0.056	0.062	0.067	0.072
The impeller total pressure loss of the stage is:	0.2372	0.2356	0.2347	0.2246	0.2237	0.2185
The rotational speed of the stage is:	11761	11761	11761	11761	11761	11761

Figure 2.20: Example of output file gathering the most important stage parameters

Chapter 3

Off Design Performance Maps

During the preliminary design phase it is also very important, both for the designer and the customer, to have an idea of the off-design performances of the compressor in order to evaluate if the machine is suitable for the desired application. The relevance of a fast and reliable estimation becomes greater thinking of the cost and time consumption of a precise CFD analysis or of an experimental campaign, in particular for cases where the number of stages is considerable.

In the recent years, a new approach has been developed and validated by Casey and Robinson [2] for single stage compressors (then extended to multi-stage by Al-Busaidi and Pilidis [8]), and it will be employed, as in the previous version of CCD, to deal with the generation of the efficiency and pressure ratio maps of the compressor. The advantage is that this procedure does not require lots of information about the compressor and it allows a quick prediction of the performances also for multi-stage layouts.

The methodology is based on four non-dimensional parameters, the flow coefficient ϕ , the efficiency η , the total work factor λ and the tip-speed Mach number M_{u2} , plus some auxiliary equations and empirical parameters to be calibrated according to the specific case. Casey and Robinson motivate the choice of these four parameters given that they are representative of some pivotal characteristics of the stage: ϕ refers to the type of the stage and is also somehow connected to the achievable efficiency (see the performance charts provided in literature) as reported in Cumpsty [6], η is related to the aerodynamic quality of the design while λ accounts for the effects of the number of blades and backsweep and more in general for the shape of impeller exit velocity triangle. Finally, the tip-speed Mach number M_{u2} characterises the application of the compressor (typically process compressors have $0.5 < M_{u2} < 1$ and for turbochargers it can go even beyond 1.5), the ratios of total pressures and temperatures and the effect played by compressibility.

Thanks to the fact that well-design stages have similar performance map shapes, it can be expected that compressors with comparable global parameters will give results close to each other. The aim of the procedure is then to find η and λ through the additional variables and formulas, thus not considering any loss correlation as done in the design part.

The fundamental assumptions at the basis of the application of Casey and Robinson model are:

- $\phi_D = \phi_P$ and $\eta_D = \eta_P$

Casey and Robinson separate the peak parameters (ϕ_P and η_P) from the design ones (ϕ_D and η_D), but instead here the design point is considered to be the peak efficiency point and to lay on the 100% speedline.

- The effect of compressor's components like the return system and the volute is neglected. Moreover, also the distinction between vaned and vaneless diffuser has been, partially, neglected, even if they play a role in the off-design performances. In fact, vaneless diffuser allow a wider range of operations and that is the reason why lots of comporessors for automotive turbochargers, where the operation is very variable, may pick a vaneless type. On the contrary, vaned diffuser will have almost constant vane exit angles independently of the working condition, allowing an easier matching of the following components. Nonetheless, corrections of peak flow coefficients are applied for turbochargers considering vaneless stages when $M_{u2} < 1.3$ from the chart of fig. (3.3) and vaned stages when $M_{u2} > 1.3$ as in fig. (3.1). This is how the implemented procedure accounts for diffuser type.

3.1 Pressure Ratio Map

The coupling bewtween CCD design analysis and performance algorithms has been conducted similarly to Romei's work with some adjustements needed to connect the employed definitions with Aungier ones. The calculation of pressure generation for the off design is strongly dependent on the blade and total work factors λ_B and λ , related by eq. (2.43).

Casey and Robinson compute the parasitic work λ_{par} (in reality only the contribution of disk friction) scaling it with the flow coefficient, while Aungier evaluates it through proper equations as discussed in the previous chapter. Due to the impossibility of applying again those correlations with this off design philosophy, it has been established to keep a constant value for the parasitic work.

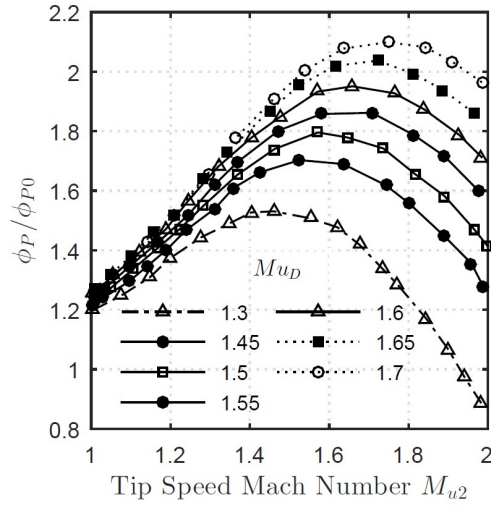


Figure 3.1: Peak flow coefficient correction of vaned turbochargers at different design Mach numbers. On the ordinate, the ratio between peak and inlet flow coefficient as function of the abscissa M_{u2}

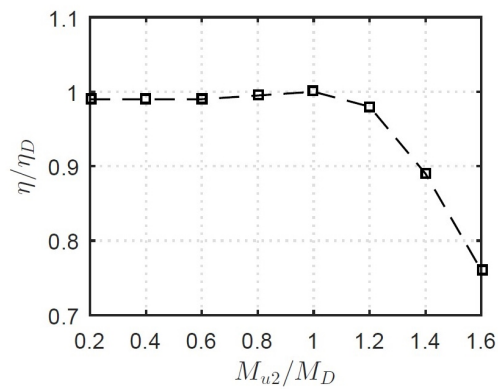


Figure 3.2: Efficiency correction ratio over a range of tip speed Mach number with respect to design one

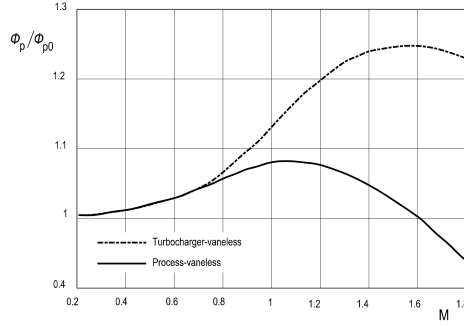


Figure 3.3: Flow coefficient correction at low design Mach number for vaneless stages. On the ordinate, the ratio of the flow coefficient to that at peak point, over a range of tip-speed Mach number

From Angier, the blade work factor can be expressed as:

$$\lambda_B = \sigma(1 + \phi_2 \zeta \tan \beta_{2,bl}) \quad (3.1)$$

For the same reason as before, the assumption of constant tip distortion ζ has been made, while the slip factor σ does not vary once eq. (2.24) is followed. λ_B is consequently a function of the exit flow coefficient ϕ_2 , that can be calculated from eq. (3.2):

$$\phi_2 = \phi_{01} \frac{\rho_{01}}{\rho_2} \frac{d_2}{\pi b_2 \epsilon_2} \quad (3.2)$$

As illustrated in Casey and Schlegel [7], the density ratio $\frac{\rho_2}{\rho_{01}}$ is found through eq.(3.3):

$$\frac{\rho_2}{\rho_{01}} = [1 + (\gamma - 1)\chi_D \lambda M_{u2}^2]^{-\frac{1}{n_d-1}} \quad (3.3)$$

where χ_D is the reaction degree [7]:

$$\chi_D = 1 - \frac{\lambda_B^2 + \phi_2^2}{2\lambda} \quad (3.4)$$

and n_d is the polytropic exponent of the total to static process 01 \rightarrow 2, derived as:

$$n_d = \frac{\gamma \eta_{p,ts}}{\gamma \eta_{p,ts} - \gamma + 1} \quad (3.5)$$

where the impeller total to static polytropic efficiency $\eta_{p,ts}$ is calculated in the same way of the total to total one. Once the work factor λ is computed, the pressure ratio is obtained

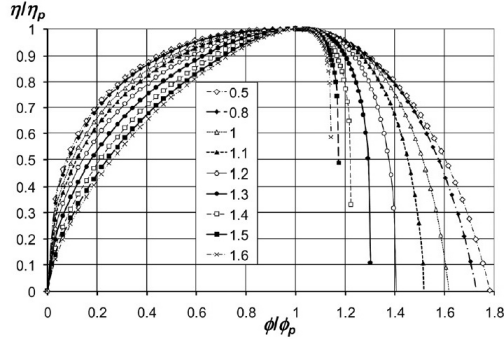


Figure 3.4: Efficiency correction with respect to flow coefficient ratio relative to that at peak efficiency at different tip-speed Mach numbers

$$\beta_T = (1 + (\gamma - 1)\lambda M_{u2}^2)^{\frac{\gamma \eta_p}{\gamma - 1}} \quad (3.6)$$

3.2 Efficiency Map

The correlation on which off design efficiency depends is function of the Mach number and of the ratio $\frac{\phi}{\phi_C}$ (where ϕ_C is the flow coefficient at choke condition):

$$\frac{\eta}{\eta_P} = \begin{cases} \left[1 - \left(1 - \frac{\phi/\phi_C}{\phi_P/\phi_C} \right)^D \right]^{1/D} & \phi < \phi_P \\ (1 - G) + G \left[1 - \left(\frac{\frac{\phi}{\phi_C} - \frac{\phi_P}{\phi_C}}{1 - \frac{\phi_P}{\phi_C}} \right)^H \right]^{1/H} & \phi > \phi_P \end{cases} \quad (3.7)$$

In (3.7) two different equations are considered for flows below and above peak efficiency point both having an ellipse-like shape with a flat region around peak efficiency η_P , as illustrated in fig. (3.4). The first equation is built so that the efficiency falls to zero at null flow and it reaches a maximum exactly at $\frac{\phi_P}{\phi_C}$. In order to match test data, the authors introduce an exponent D which takes different values according to M_{u2} (it varies between 1.7 for high M_{u2} and 2.1 for low M_{u2}).

The right hand side curve starts from the peak with another flat region and then decreases rapidly. In the equation is inserted a factor G to account for the fact that when maximum flow is reached the efficiency may differ from zero. More precisely, the value of $\frac{\eta}{\eta_P}$ at which maximum limit occurs is represented by $(1-G)$. For low Mach number impellers, that will not arrive at choke condition due to the onset of negative incidence stall well before,

G assumes a value bigger than one (the author uses $G = 2$) while for high speed impellers it can be $G = 0.3$ since in these cases maximum flow will be reached soon after peak efficiency. Parameter H , similarly to D of eq. (3.7), accounts for different efficiency trends depending on Mach number, as typically the efficiency drop in the high flow region is getting sharper as Mach number increases.

All these coefficients ($\frac{\phi_P}{\phi_C}$, D , G , H) has the only dependence on the Mach number between the speedlines but they are constant along a single one. Moreover, they tend to have constant values also at low speeds (where the flow is close to be incompressible) and at high speeds as discovered by Casey and Robinson analysing several test data. The intermediate values are then found through the use of the blending function P of eq.(3.8) with those values as asymptotes.

$$P = \frac{1}{1 + e^{-t}} \quad t = (M - B)(AM + C) \quad (3.8)$$

From which follows:

$$\begin{aligned} \frac{\phi_P}{\phi_C} &= (1 - P) \left(\frac{\phi_P}{\phi_C} \right)_{LO} + P \left(\frac{\phi_P}{\phi_C} \right)_{HI} \\ D &= (1 - P)D_{LO} + PD_{HI} \\ G &= (1 - P)G_{LO} + PG_{HI} \\ H &= (1 - P)H_{LO} + PH_{HI} \end{aligned}$$

The limit for peak to choke flow coefficient ratio is

$$\left(\frac{\phi_P}{\phi_C} \right)_{LO} = \begin{cases} 0.55 & \text{for process} \\ 0.5 & \text{for turbochargers} \end{cases} \quad (3.9)$$

$$\left(\frac{\phi_P}{\phi_C} \right)_{HI} = \begin{cases} 0.84 & \text{for process} \\ 0.79 & \text{for turbochargers} \end{cases} \quad (3.10)$$

The transition between the low and the high limits is regulated by three coefficients A , B and C . B influences the position in which the mean value is reached, and is suggested to be chosen as:

$$B = \begin{cases} 1.1 - 1.2 & \text{for turbocharger} \\ 0.8 - 0.9 & \text{for process} \end{cases} \quad (3.11)$$

For the cases examined by Casey and Robinson the value of A is between 0 and 1 and for C between 4 and 5 and they determine the rate of change of the coefficients with M .

-----Input parameters to calibrate the Performance Map -----

N_Speedlines	3
N_max[%]	105
N_min[%]	90
A	0
B	0.8
C	5
As	0
Bs	0.8
Cs	4.75
D_low	2.1
D_high	1.7
G_low	2
G_high	0.3
H_high	3.5
H_low	2
peak_to_choke_low	0.55
peak_to_choke_high	0.95
surge_to_choke_low	0.225
surge_to_choke_high	0.835

Figure 3.5: Example of input file for the performance maps

3.3 Procedure in CCD

In a specific input file, as the one illustrated in fig. (3.5), the reference constants are set according to the guidelines explained above.

The user can select the number of speedlines to be considered in the maps. The speedlines are generated as a percentage of the design rotational speed (the 100% one) so that the tip peripheral speed u_2 and tip-speed Mach number M_{u2} are consequently scaled. The peak efficiency points different from the 100% one will result from a correction on ϕ_P dependent on the Mach ratio of $\frac{M_{u2}}{M_D}$ and the same will be for ϕ_P , according to the graphs reported in fig. (3.2) and fig. (3.3).

The range of a single speedline is enclosed by two extreme conditions: the surge at low flow rate and the choke at high flow rate. Surge is the instability of the machine happening when it is no more able to sustain the pressure difference across it, leading to serious damages, while choke is the point in which the flow reaches sonic velocity and mass flow can increase no more. Those limits are expressed in terms of flow coefficients, respectively ϕ_S

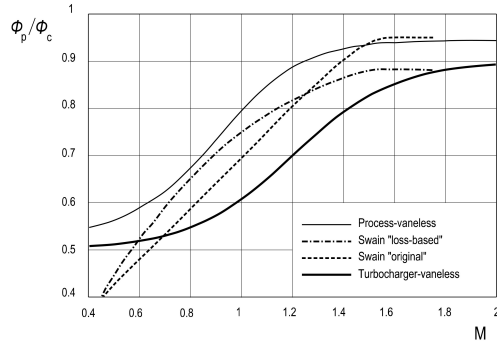


Figure 3.6: Variation of the peak flow coefficient with respect to that at choke $\frac{\phi_P}{\phi_C}$ over a range of tip-speed Mach number

and ϕ_C for the surge and the choke and more exactly they are established as ratios with respect to the peak flow coefficient ϕ_P . As the authors themselves explain, it is difficult to predict stability limits because a very deep knowledge of the internal aerodynamics, geometry and loading is mandatory, but from the variety of test data available, they give some indications according to the specific machine. In any case, the graphs fig.3.6 and fig. 3.7 are the support to estimate surge and choke limits.

Some examples of performance maps are given in fig. (3.8) and fig. (3.9)

Similarly to what done for the design, a stage stage stacking technique is applied to gain the whole compressor maps.

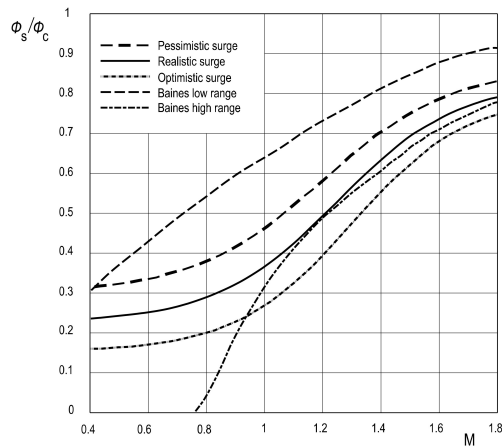


Figure 3.7: Variation of the surge flow coefficient with respect to that at choke $\frac{\phi_s}{\phi_c}$ over a range of tip-speed Mach number

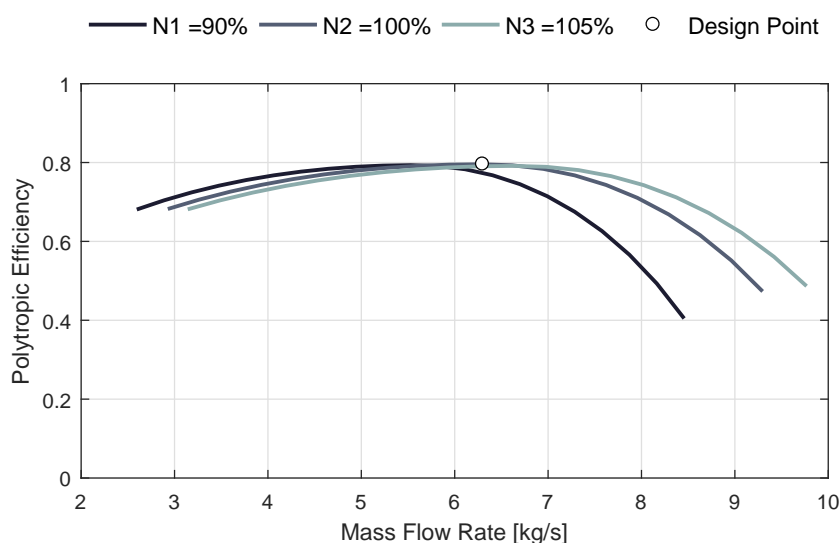


Figure 3.8: Example of an efficiency performance map of the compressor as generated by CCD

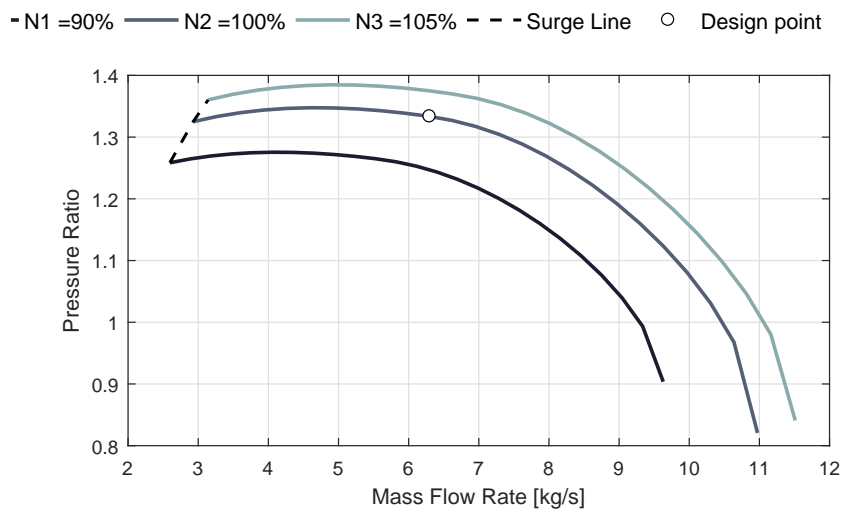


Figure 3.9: Example of a pressure ratio performance map of the compressor as generated by CCD

Chapter 4

Validation

In this chapter the application and validation of the new implemented code is discussed.

In order to compare both the preliminary design quantities and the peak performances, looking also at the off-design behaviour, four test cases have been considered:

- 3 Stage compressor - IGCC (Integrally Geared Centrifugal Compressor)
- 5 stage compressor - process
- 6 stage compressor - hydrogen rich gas
- 1 stage compressor - turbocharger HECC (High Efficiency Centrifugal Compressor)

It has to be pointed out that the validation process is made more difficult by the fact that no complete information about the compressors is usually available in open literature. In fact, it is common to find quite detailed descriptions about the design of a compressor with just a hint on the performance maps and viceversa; the consequence is that some parameters must be reasonably guessed in order to perform the simulations.

First of all, in order not to confuse the reader, the version of CCD which is currently discussed in this thesis is named CCD V03, since two versions, CCD V01 and CCD V02, were created by A. Romei in his work, differing in the philosophy for blade exit angle $\beta_{2,bl}$ computation. The comparisons will be made with CCD V01 as, like in CCD V03, the possibility of selecting $\beta_{2,bl}$ is given in the input file, allowing a more proper procedure.

The choice of these particular validation cases has been made considering that the first three have been analysed also for CCD V01 and it was a due

benchmark, while the last one has been added mainly because some CFD studies at the Von Karman Institute have been conducted about it and a comprehensive paper was published on its regard.

The adopted strategy is to confront the obtained results of the new CCD V03 both with the test data and with CCD V01. At first, the same input employed at its time for CCD V01 is used to examine what the outcome is when equal information are provided. Successively, if necessary, some input parameters are tuned to catch more precisely important characteristics of the test cases.

4.1 3 stages IGCC

In the recent years, the applications with integrally geared centrifugal compressor (IGCC) have been continuously increasing, from air separation plants to power generation and hydrocarbon refrigeration. An IGCC is an efficient and reliable multi-shaft machine in which a proper gear coupling interconnects the shafts regulating the rotational speeds [9]. The removal of the velocity constraint and the possibility of employing intercoolers are the most remarkable advantages that make this arrangement frequently preferable to in-line compressors.

The present IGCC is a 3 stages machine working with air. The stages are mounted on two shafts: two stages on the first shaft, both with intercoolers, and the third stage on the other, that is the fastest. Moreover, the first stage is equipped with a vaned diffuser while the others with a vaneless one. A picture of the geometry as generated by CCD is illustrated in fig. (4.1).

Since, for this case, geometrical and performance data have been reachable [12], a careful analysis has been made. Table 4.1 reports the comparison between CCD V03 and the test data, with the indication of the relative errors between the two, calculated as $(X_{CCD} - X_{ref})/X_{ref}$, where X indicates a general compressor quantity. The same comparison, but with respect to the results of CCD V01, is done in table 4.2.

Tables 4.1 and 4.2 highlight that the the thermodynamic outlet quantities of the stages are well foreseen by the code (the relative errors are all less than 1%), thanks also to the role played by the intercoolers, that impose fix suction temperatures for both the second and the last stage, reducing possible errors accumulation from one stage to another. In general, the second stage is the one that distances itself the most from the reference compressors parameters such as tip speed Mach number M_{u2} (deviation of -4%) and total work factor λ (deviation of $+8.2\%$). The cause can be found in the lower estimation of both the rotational speed and tip diameter. On the contrary, the peak

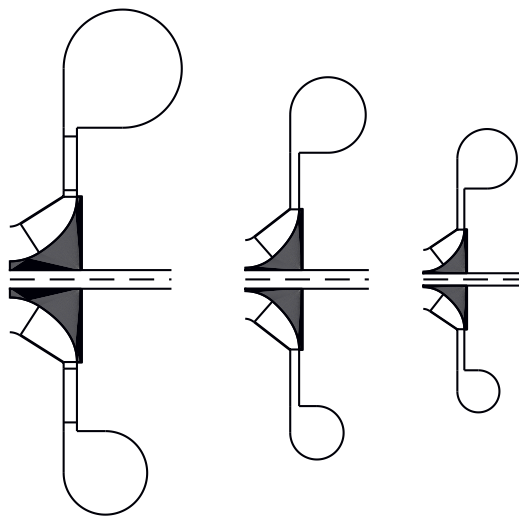


Figure 4.1: Geometry of the compressor 3 stages IGCC as generated by CCD V03

efficiency predictions are very good (well under 1% of relative errors), in line also with CCD V01. For what concerns the geometrical quantities, relevant differences (higher than 10%) are encountered in the exit blade width and diffuser exit radius of the first stage.

	CCD V03			3 Stages IGCC			Relative Errors		
	Stage 1	Stage 2	Stage 3	Stage 1	Stage 2	Stage 3	Stage 1	Stage 2	Stage 3
Flow Rate [Nm ³ /h]	81500			81500					
Stage [·]	3			3					
ϕ_{01} [·]	0.107	0.085	0.098	0.109	0.082	0.089			
$\beta_{2,bl}$ [deg]	-40	-40	-40	-40	-40	-40			
Pressure Ratio [·]	2.163	1.749	1.726	2.163	1.749	1.726			
Shape Factor [·]	0.88	0.91	0.93	0.88	0.91	0.93			
Thermodynamic Quantities									
$T_{0,in}$ [K]	298.2	304	305	298.2	304.2	305	+0%	-0.1%	+0%
$T_{0,out}$ [K]	383.3	365.3	365.4	382	365	365	+0.3%	+0.1%	+0.1%
$p_{0,in}$ [bar _a]	1.01	2.13	3.63	1.008	2.115	3.645	+0.2%	+0.7%	-0.4%
$p_{0,out}$ [bar _a]	2.18	3.73	6.27	2.18	3.7	6.29	+0%	+0.8%	-0.3%
Compressor Parameters									
η_p [·]	0.878	0.870	0.863	0.88	0.875	0.866	-0.2%	-0.6%	-0.3%
M_{u2} [·]	1.085	0.912	0.917	1.1	0.95	0.94	-1.4%	-4%	-2.4%
λ [·]	0.606	0.606	0.589	0.59	0.56	0.56	+2.7%	+8.2%	+5.2%
N[rpm]	9018	9018	12779	9335	9335	12713	-3.4%	-3.4%	+0.5%
Power [kW]	6026			6333			-4.9%		
Geometrical Quantities									
d_2 [m]	0.784	0.665	0.472	0.780	0.675	0.494	+0.5%	-1.5%	-4.5%
d_h [m]	0.172	0.111	0.073	0.182	0.117	0.077	-5.5%	-5.1%	-5.2%
d_e [m]	0.496	0.369	0.276	0.524	0.399	0.301	-5.3%	-7.5%	-8.3%
b_1 [mm]	162	129	102	171	130	99	-5.3%	-0.8%	+3%
b_2 [mm]	63	42	33	55	42	34	+14.5%	+0%	-2.9%
N_{bt} [·]	17	15	16	16	16	16	+6.3%	-6.3%	+0%
Diffuser Parameters									
d_3 [m]	0.846				0.88				-3.8%
d_5 [m]	1.438	1.202	0.862	1.216	1.25	0.84	+18.3%	-3.8%	+7.2%
N_{vanes} [·]	19				19				+0%
α_3 [deg]	63.6				60.5				+5.1%

Table 4.1: Comparison between the output of CCD V03 and the reference data using the input quantities of the validation for CCD V01. In **bold** the parameters that are imposed to the code

	CCD V03			CCD V01			Relative Errors		
	Stage 1	Stage 2	Stage 3	Stage 1	Stage 2	Stage 3	Stage 1	Stage 2	Stage 3
Flow Rate [Nm ³ /h]	81500			81500					
Stage[-]	3			3					
ϕ_{01} [-]	0.107	0.085	0.098	0.107	0.092	0.098			
$\beta_{2,bl}$ [deg]	-40	-40	-40	-40	-40	-40			
Pressure Ratio [-]	2.163	1.749	1.726	2.163	1.749	1.726			
Shape Factor[-]	0.88	0.91	0.93	0.88	0.91	0.93			
Thermodynamic Quantities									
$T_{0,in}$ [K]	298.2	304	305	298.2	304	305	+0%	+0%	+0%
$T_{0,out}$ [K]	383.3	365.3	365.4	382.7	364.1	364.4	+0.3%	+0.1%	+0.1%
$p_{0,in}$ [bar _a]	1.01	2.13	3.63	1.01	2.13	3.63	+0%	+0%	+0%
$p_{0,out}$ [bar _a]	2.18	3.73	6.27	2.18	3.73	6.27	+0%	+0%	+0%
Compressor Parameters									
η_p [-]	0.878	0.870	0.863	0.883	0.886	0.876	-0.6%	-1.8%	-1.5%
M_{u2} [-]	1.085	0.912	0.917	1.108	0.905	0.911	-2.1%	+0.8%	+0.7%
λ [-]	0.606	0.606	0.589	0.58	0.60	0.59	+4.5%	+1%	-0.2%
N[rpm]	9018	9018	12779	9302	9302	12653	-3.1%	-3.7%	-4.2%
Power[kW]	6026			5964.3			+1.5%		
Geometrical Quantities									
d_2 [m]	0.784	0.665	0.472	0.775	0.640	0.474	+1.2%	+3.9%	-0.4%
d_h [m]	0.172	0.111	0.73	0.177	0.115	0.076	-2.8	-3.5%	-3.9
d_e [m]	0.496	0.369	0.276	0.512	0.383	0.288	-3.1%	-3.7%	-4.2%
b_1 [mm]	162	129	102	173	134	102	-6.4%	-3.7%	+0%
b_2 [mm]	63	42	33	57	46	36	+10.5%	-8.7%	-8.3%
N_{bl} [-]	17	15	16	16	18	16	+6.3%	-16.7%	+0%
Diffuser Parameters									
d_3 [m]	0.846				0.859				-1.5%
d_5 [m]	1.438	1.202	0.862	1.267	1.038	0.771	+13.5%	+15.8%	+11.8%
N_{vanes} [-]	19				16				+18.8%
α_3 [deg]	63.6				63.3				+0.5%

Table 4.2: Comparison between the output of CCD V03 and CCD V01, with the indication of relative errors in the last column. In **bold** the quantities that are imposed to the code

4.1.1 Off-Design IGCC

The off-design maps, as reported in table (4.3) and table (4.4), have been evaluated using the values of off-design parameters suggested by Casey and Robinson for process compressors (discussed at section 3.2), but the peak to choke flow coefficient parameter ϕ_P/ϕ_C has been rised till 0.95 as the turning towards choke after peak efficiency is quite sudden for the first stage.

A	B	C	A_s	B_s	C_s
0.5	0.85	5	0	0.85	4.75

Table 4.3: Value of off-design constants for blending function

	D	G	H	ϕ_P/ϕ_C	ϕ_S/ϕ_C
Low Mach	1.7	2	2	0.55	0.225
High Mach	2.1	0.3	3.5	0.95	0.835

Table 4.4: Value of off-design constants for low and high Mach numbers

In two separate plots shown in fig. (4.2) and fig. (4.3) the efficiency and pressure ratio maps have been compared to test data and CCD V01 maps.

The shape of the efficiency curves traces very well the IGCC map, especially for the first stage where they are almost superposed. The other two stages differentiate a bit in the high speed region near choke, as a consequence of the tuning made for the first stage.

The pressure ratio map is almost identical for CCD V01 and V03, also because they rely on the same off-design model, while is not yet able to catch the real trend as in reality it has a very rapid decrease from stall to choke condition limiting the range of operation, reasonably due to the effect of the vaned diffuser that is not well simulated by the off-design methodology.

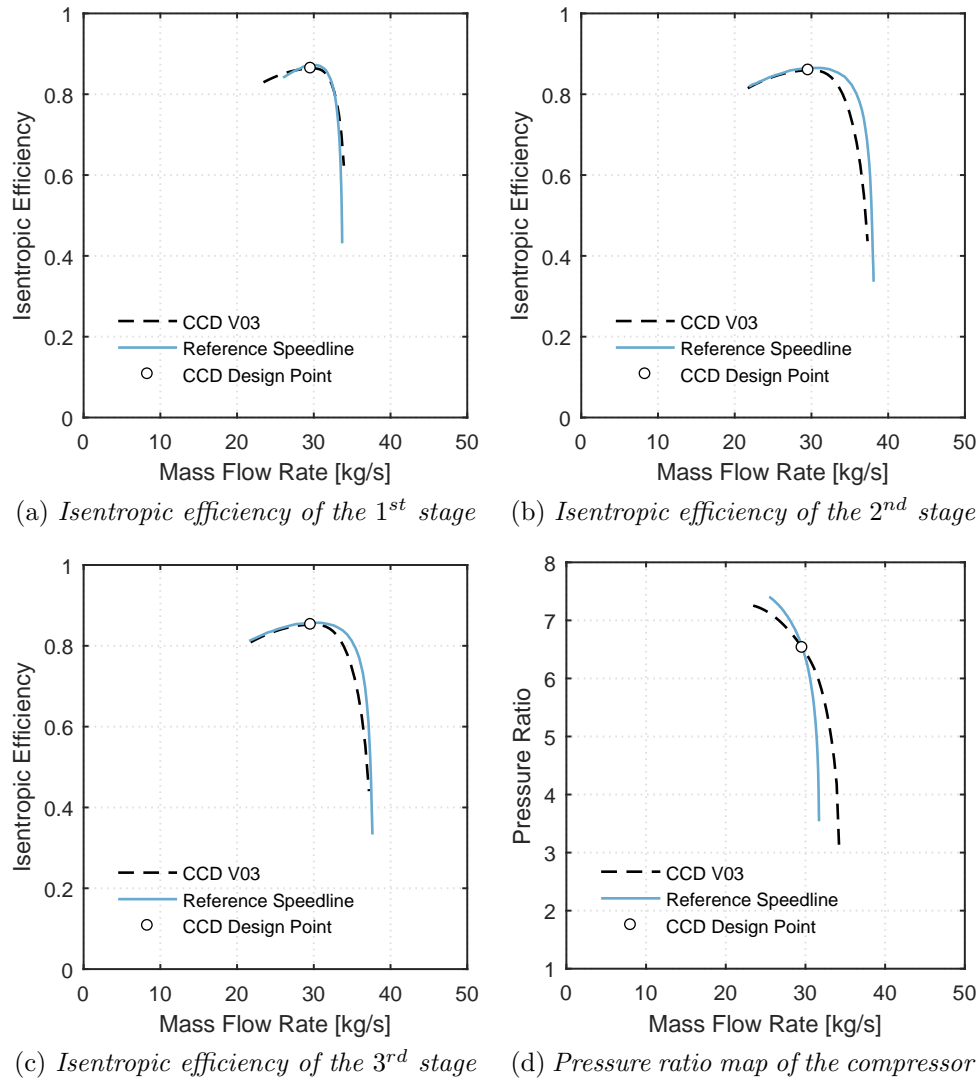


Figure 4.2: Comparison off CCDV03 maps with tests

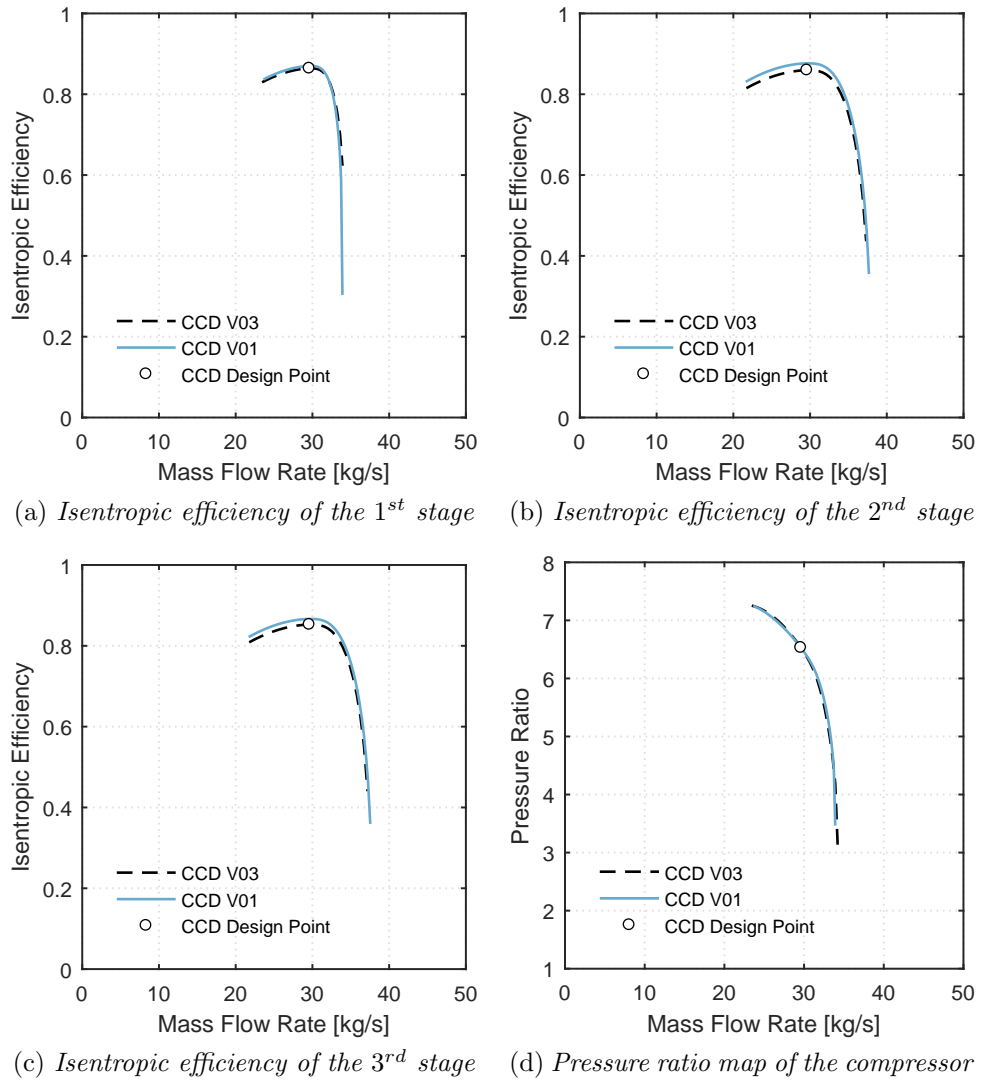


Figure 4.3: Comparison of CCD V03 maps with CCD V01

4.1.2 Match of first stage

As it emerged from table 4.1, in order to reduce the excessive geometrical differences related to exit diffuser diameter d_5 and vaned diffuser inlet flow angle α_3 of the first stage, a second simulation is performed with ad hoc settings that have been applied to the vaned diffuser routine. Moreover, also an intervention on the blade inlet d_{1m}/d_e has been carried out to regulate the blade width. The new differences in the first stage can be appreciated in fig. (4.4).

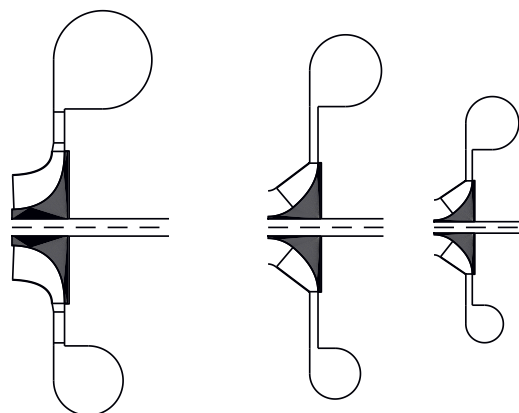


Figure 4.4: 3 stages IGCC geometry with matching input

In table (4.5) the new results with respect to the test case are reported, while table (4.6) sums up the deviations with respect to CCD V01.

	CCD V03			3 Stages IGCC			Relative Errors		
	Stage 1	Stage 2	Stage 3	Stage 1	Stage 2	Stage 3	Stage 1	Stage 2	Stage 3
Flow Rate [Nm ³ /h]	81500			81500					
Stage [\cdot]	3			3					
ϕ_{01} [\cdot]	0.109	0.087	0.097	0.109	0.082	0.089			
$\beta_{2,bl}$ [deg]	-40	-40	-40	-40	-40	-40			
Pressure Ratio [\cdot]	2.163	1.749	1.726	2.163	1.749	1.726			
Shape Factor [\cdot]	0.88	0.91	0.93	0.88	0.91	0.93			
Thermodynamic Quantities									
T_{0,in} [K]	298.2	304	305	298.2	304.2	305	+0%	-0.1%	+0%
T_{0,out} [K]	384.1	365.2	365.6	382	365	365	+0.5%	+0.1%	+0.2%
p_{0,in} [bar _a]	1.01	2.13	3.63	1.008	2.115	3.645	+0.2%	+0.7%	-0.4%
p_{0,out} [bar _a]	2.18	3.73	6.27	2.18	3.7	6.29	+0%	+0.8%	-0.3%
Compressor Parameters									
η_p [\cdot]	0.871	0.870	0.860	0.88	0.875	0.866	-1%	-0.6%	-0.7
M_{u2} [\cdot]	1.09	0.91	0.92	1.1	0.95	0.94	-0.9%	-3.8%	-2.4%
λ [\cdot]	0.61	0.60	0.59	0.59	0.56	0.56	+2.5%	+7.7%	+5.4%
N [rpm]	9170	9170	12729	9335	9335	12713	-1.8%	-1.8%	+0.1%
Power [kW]	6054			6333					
Geometrical Quantities									
d₂ [m]	0.774	0.655	0.475	0.780	0.675	0.494	-0.8%	-3%	-3.8%
d_h [m]	0.184	0.111	0.073	0.182	0.117	0.077	+1.1%	-5.1%	-5.2%
d_e [m]	0.531	0.369	0.276	0.524	0.399	0.301	+1.3%	-7.5%	-8.3%
b₁ [mm]	174	129	102	171	130	99	+1.8%	-0.8%	+3%
b₂ [mm]	55.6	42	33	55	42	34	+1.1%	+0%	-2.9%
N_{bl} [\cdot]	16	15	16	16	16	16	+0%	-6.3%	+0%
Diffuser Parameters									
d₃ [m]	0.863				0.88				-2%
d₅ [m]	1.207	1.231	0.793	1.216	1.25	0.84	-0.7%	-1.5%	-1.4%
N_{vanes} [\cdot]	19				19				+0%
α_3 [deg]	60.5				60.5				+0%

Table 4.5: Comparison between the output of CCD V03 and the test data after matching vaned diffuser quantities. In **bold** the quantities that are imposed to the code and in *italic* the matched quantity of the first stage vaned diffuser

	CCD V03			CCD V01			Relative Errors		
	Stage 1	Stage 2	Stage 3	Stage 1	Stage 2	Stage 3	Stage 1	Stage 2	Stage 3
Flow Rate [Nm ³ /h]	81500			81500					
Stage[-]	3			3					
ϕ_{01} [-]	0.109	0.087	0.097	0.107	0.092	0.098			
$\beta_{2,bl}$ [deg]	-40	-40	-40	-40	-40	-40			
Pressure Ratio [-]	2.163	1.749	1.726	2.163	1.749	1.726			
Shape Factor[-]	0.88	0.91	0.93	0.88	0.91	0.93			
Thermodynamic Quantities									
$T_{0,in}$ [K]	298.2	304	305	298.2	304	305			
$T_{0,out}$ [K]	384.1	365.2	365.6	382.7	364.1	364.4			
$p_{0,in}$ [bar _a]	1.01	2.13	3.63	1.01	2.13	3.63			
$p_{0,out}$ [bar _a]	2.18	3.73	6.27	2.18	3.73	6.27			
Compressor Parameters									
η_p [-]	0.871	0.870	0.860	0.883	0.886	0.876	-1.4%	-1.8%	-1.8%
M_{u2} [-]	1.09	0.91	0.92	1.108	0.905	0.911	-1.6%	+1%	+0.7%
λ [-]	0.61	0.60	0.59	0.58	0.60	0.59	+4.3%	+0.5%	+0%
N[rpm]	9170	9170	12729	9302	9302	12653	-1.4%	-1.4%	+0.7%
Power[kW]	6054			5964.3					
Geometrical Quantities									
d_2 [m]	0.774	0.655	0.475	0.775	0.640	0.474	-0.1%	+2.3%	+0.2%
d_h [m]	0.184	0.111	0.73	0.177	0.115	0.076	+4%	-3.5%	-3.9%
d_e [m]	0.531	0.369	0.276	0.512	0.383	0.288	+3.7%	-3.7%	-4.2%
b_1 [mm]	174	129	102	173	134	102	+0.6%	-3.7%	+0%
b_2 [mm]	55.6	42	33	57	46	36	-2.5%	-8.7%	-8.3%
N_{bl} [-]	16	15	16	16	18	16	+0%	-16.7%	+0%
Diffuser Parameters									
d_3 [m]	0.863				0.859			+0.3%	
d_5 [m]	1.207	1.231	0.793	1.267	1.038	0.771	-4.7%	+18.6%	+2.9%
N_{vanes} [-]	19				16			+18.8%	
α_3 [deg]	60.5				63.3			-4.4%	

Table 4.6: Comparison between the output of CCD V03 and CCD V01 with the new geometry for first stage. In **bold** the quantities that are imposed to the code and in *italic* the matched quantity of the first stage vaned diffuser

Even if the geometry for the first stage has been adjusted to trace the original compressor, the efficiency prediction has worsen. This can be a signal that Aungier considerations about geometrical optimal values, though he affirmed to be general since validated over a wide range of compressors type, suit for some application but may differ from others, as it can be seen for the vane inlet angle that with CCD model is around 63.5° while in reality is 60.5° .

4.2 5 Stages Process Compressor

The second case for validation is a five-stage gas export centrifugal compressor studied in the work of Al Busaidi [8]. Contrarily to the IGCC compressor, not a lot of information were provided. For example, it is known that the machine is processing a hydrocarbon mixture with molecular weight of $\tilde{M} = 19.10 \text{ g/mol}$, but the isentropic coefficient is not specified and it has been taken equal to 1.275. Moreover, no information about the effect played by compressibility are reported, increasing the difficulty of predicting the flow behaviour. The suction conditions are $p_{0,in} = 8 \text{ bar}$ and $T_{0,in} = 324.35 \text{ K}$ with a discharge pressure of 21 bar. Due to the lack of specifications, at the beginning the exact values of inlet flow coefficient ϕ_{01} and shape factor used for CCD V01 are taken. The blade exit angles, instead, is an explicit parameter. The comparisons with the five stages and CCD V01 are given in table (4.7) and table (4.8). The drawn geometry of the machine is the one of fig. (2.19)

	CCD V03					Al Busaidi				
	St 1	St 2	St 3	St 4	St 5	St 1	St 2	St 3	St 4	St 5
Mass Flow [kg/s]	59.16					59.16				
$\beta_{2,bl}[-]$	-50	-49	-48	-48	-48	-50	-49	-48	-48	-48
Pressure Ratio [-]	1.24	1.22	1.21	1.20	1.19	1.24	1.22	1.21	1.20	1.19
$\eta_p[-]$	0.827	0.831	0.832	0.834	0.854	0.86	0.86	0.86	0.85	0.85
b_1 [mm]	97	88	79	70	62	100	92	85	77	69
b_2 [mm]	59	53	49	45	42	53	48	45	41	37
d_2 [mm]	640	626	614	607	594	655	655	655	650	645
$d_h/d_2[-]$	0.359	0.366	0.373	0.386	0.402	0.342	0.353	0.367	0.380	0.392

Table 4.7: Comparison between CCD V03 and 5-stage compressor test case with the same input used in V01. In **bold** the quantities that are imposed to the code

	CCD V03					CCD V01				
	St 1	St 2	St 3	St 4	St 5	St 1	St 2	St 3	St 4	St 5
Mass Flow [kg/s]	59.16					59.16				
$\beta_{2,bl}[-]$	-50	-49	-48	-48	-48	-50	-49	-48	-48	-48
Pressure Ratio [-]	1.24	1.22	1.21	1.20	1.19	1.24	1.22	1.21	1.20	1.19
$\eta_p[-]$	0.827	0.831	0.832	0.834	0.854	0.887	0.887	0.885	0.882	0.877
b_1 [mm]	97	88	79	70	62	102	91	82	72	63
b_2 [mm]	59	53	49	45	42	53	49	46	42	40
d_2 [mm]	640	626	614	607	594	654	638	621	614	605
$d_h/d_2[-]$	0.359	0.366	0.373	0.386	0.402	0.345	0.353	0.365	0.380	0.395

Table 4.8: Comparison between CCD V03 and V01 for the 5-stage compressor test case with the same input used in V01. In **bold** the quantities that are imposed to the code

A different philosophy, with respect to CCD, has been adopted to design the compressor for what concerns the tip diameter d_2 . In the real application it remains almost constant between the stages while in CCD, since it is taken into account the variation of volumetric flow rate across the machine, it typically decreases from one stage to another. This difference influences also the tip blade width b_2 , while the ratio d_h/d_2 is quite well respected. More importantly, with these inputs the predicted peak efficiency for the first stages is notably lower than the reference. A cause can be individuated also in the value of flow coefficient $\phi_{01} = 0.093$, which is quite high for the first stage having a backsweep of 50° . Additionally, it also unusual that, for a global pressure of 3, five stages have been employed, underlining once more that such a peculiar application may diverge from common design practices.

4.2.1 Off-design 5 stages

The interesting aspect of this validation case is the range on which compressor maps data have been provided, with speedlines from 60% to 100%. In this way, it is possible to compare how Casey and Robinson model will behave far from the operational speedline. Since the compressor to deal with is of process type, similar parameters to the previous case are employed here (see table (4.9) and table (4.10)), with the exception of B that is set to 0.55 according to the mean Mach number of the machine, which is indeed around 0.55, in order to give the blending function P an almost identical parameter variation trend among the stages.

A	B	C	A_s	B_s	C_s
1	0.55	5	0	0.55	4.75

Table 4.9: 5 stages off design paramters for blending function

	D	G	H	ϕ_P/ϕ_C	ϕ_S/ϕ_C
Low Mach	1.7	2	2	0.50	0.225
High Mach	2.1	0.3	3.5	0.95	0.835

Table 4.10: 5 stages off design parameters

The pressure ratio is well estimated for what concerns the lower speedlines but loses effectiveness close to surge line when the speed increases. Surely, the fact that design point is not on the 100% speedline but just a bit lower has an impact on the shift (if the highest speedline is corrected a more similar trend is shown, as depicted in fig. (4.7)).

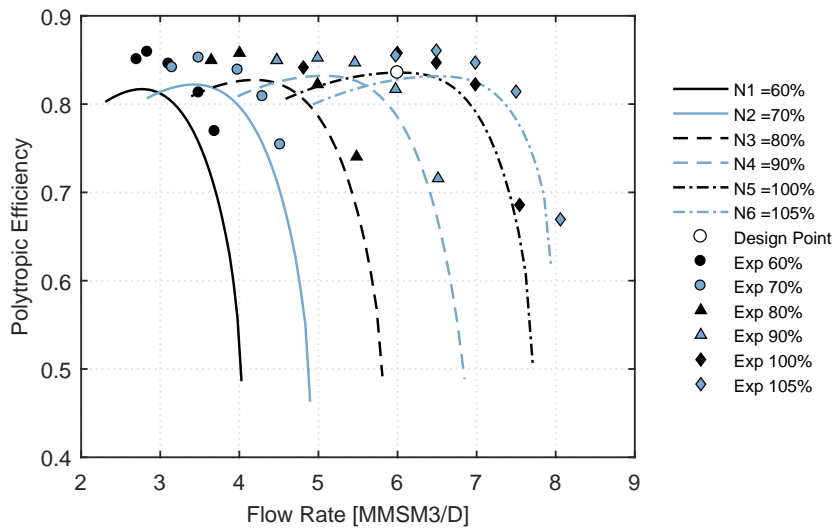


Figure 4.5: 5 stages efficiency map with test data

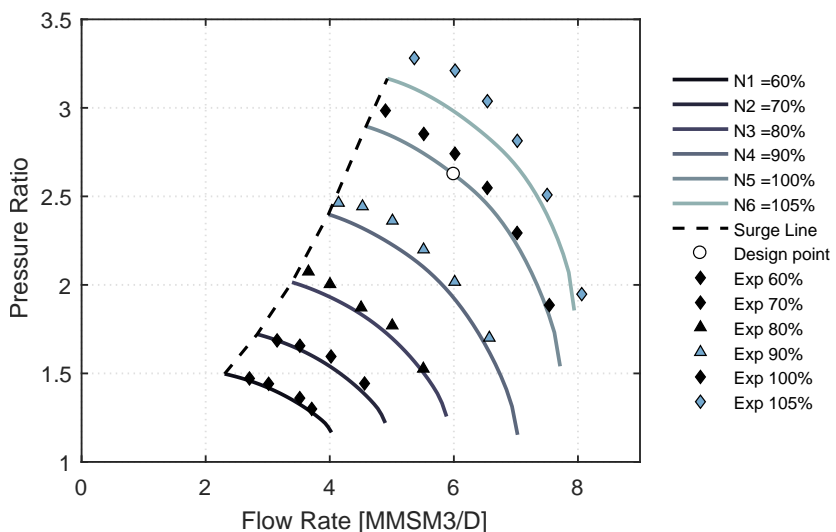


Figure 4.6: 5 stages pressure ratio map with test data

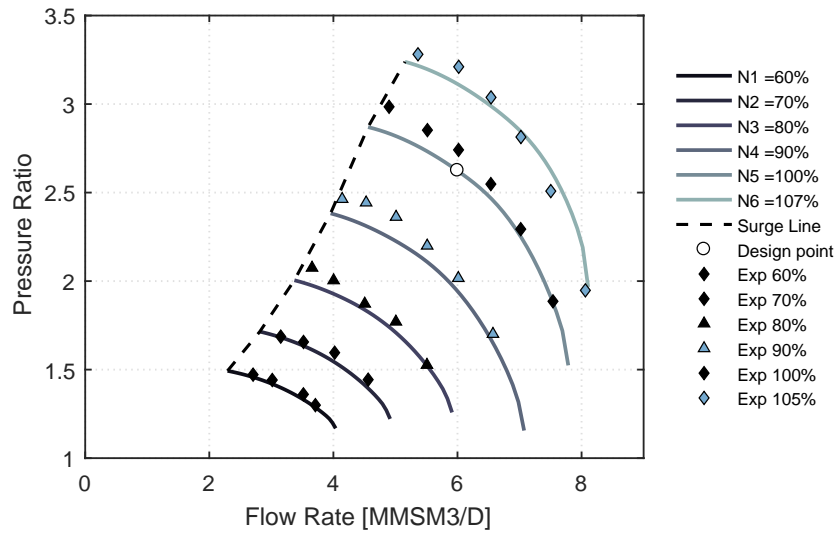


Figure 4.7: Pressure ratio map with speed correction for the higher speedline to account the design point shift

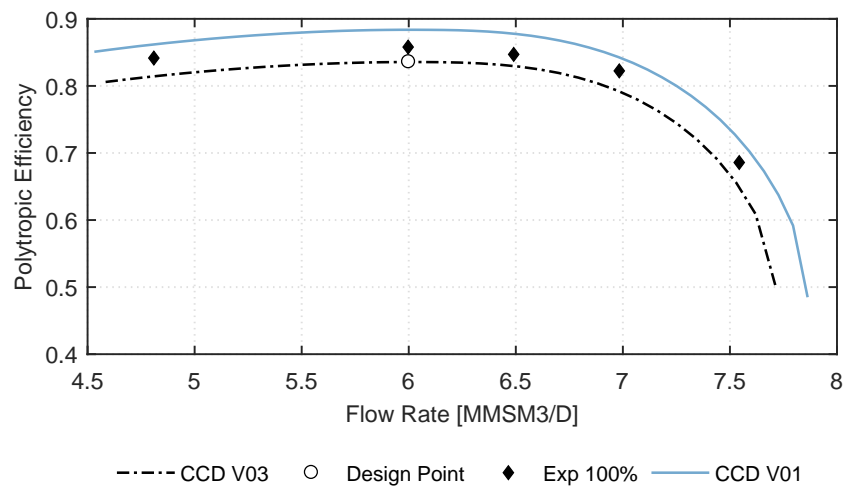


Figure 4.8: 5 stages efficiency map of 100% speedline

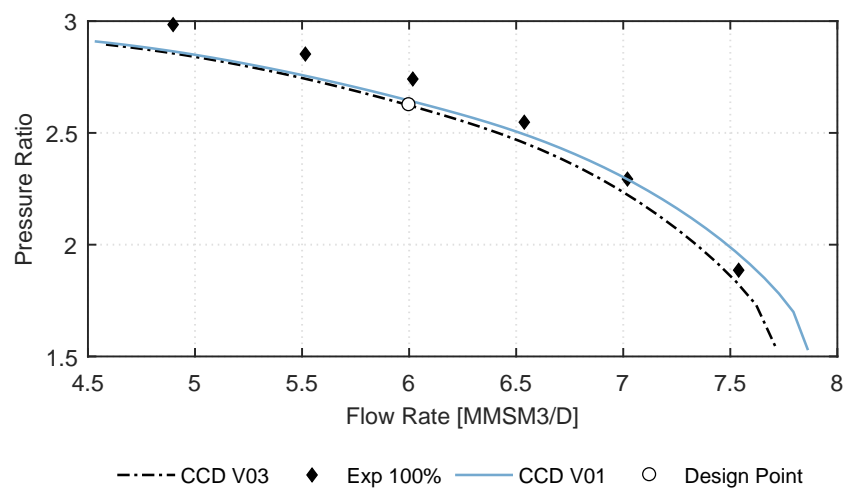


Figure 4.9: 5 stages pressure ratio map of 100% speedline

4.2.2 6 Stages Hydrogen compressor

The six stage hydrogen compressor is taken from the work of Ludtke [3]. Also in this case not a lot of data are available. The suction pressure is $p_{0,in} = 51$ bar and the discharge one $p_{0,out} = 58$ bar with a mass flow of $\dot{m} = 6.3$ kg/s. The pressure ratio distribution is unknown so that it is assumed to be uniform among the stages. On the other hand, the flow coefficient is $\phi_{01} = 0.0181$ and the rotational speed $N = 12700$ rpm, not very high values in order to keep the tip peripheral speed at low values as a consequence of the low molar mass \tilde{M} .

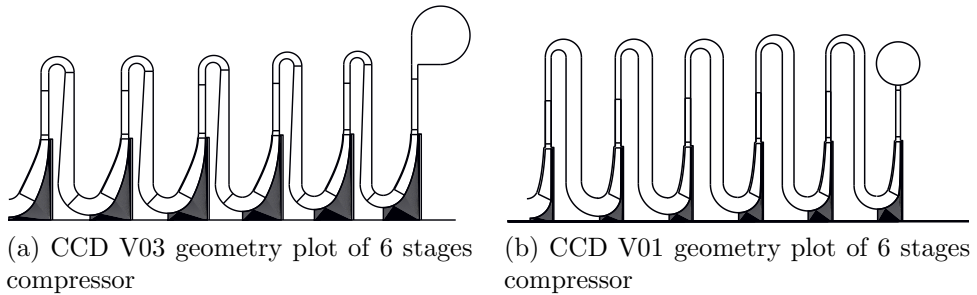


Figure 4.10: 6 stages compressor geometry

The data of the compressor are collected in table (4.11)

\dot{m} [kg/s]	$p_{0,in}$ [bar]	$p_{0,out}$ [bar]	ϕ_{01}	N [rpm]
6.3	51	68	0.0181	12700

Table 4.11: Data of 6 stage hydrogen compressor

The suction temperature is not reported and it is assumed to be equal to the ambient one. Initially, $\phi_{01} = 0.027$ is considered, in order to use the same input of V01 and compare the outputs.

The main results are shown in table (4.12)

As the speedline at full capability was known, a comparison is shown in fig. (4.11).

	CCD V03						CCD V01						
	St. 1	St. 2	St. 3	St. 4	St. 5	St. 6		St. 1	St. 2	St. 3	St. 4	St. 5	St. 6
N[rpm]	11741	11741	11741	11741	11741	11741		12720	12720	12720	12720	12720	12720
$\beta_{2,bl}$ [deg]	-45	-45	-45	-50	-50	-50		-45	-45	-45	-50	-50	-50
shape factor[-]	0.80	0.75	0.70	0.65	0.60	0.55		0.80	0.75	0.70	0.65	0.60	0.55
d_2 [mm]	333	336	339	348	351	351		324	328	331	345	348	352
u_2 [m/s]	205	206	208	213	215	216		216	218	220	229	231	234
η_p [-]	0.816	0.809	0.801	0.792	0.783	0.787		0.764	0.756	0.749	0.731	0.724	0.718
b_1 [mm]	31	29	27	25	23	21		27	26	24	23	22	20
b_2 [mm]	14	14	13	13	12	12		11	11	10	10	10	9

Table 4.12: Six stages compressor comparison between the outputs of CCD V03 and V01 with $\phi_{01} = 0.027$. In **bold** the quantities that are imposed to the code

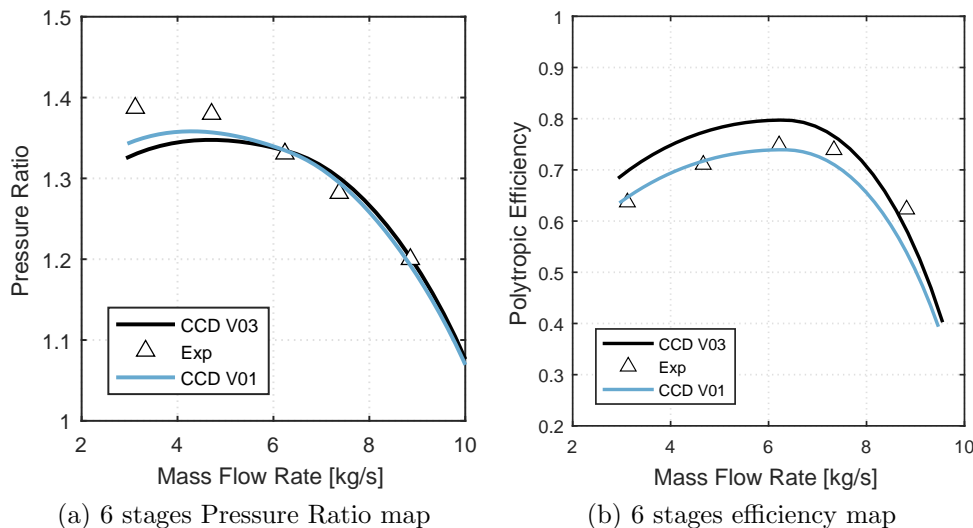


Figure 4.11: Efficiency and PR maps comparison for the 6 stages case

4.2.3 Flow coefficient match

As it emerged from the analysis, the most notable difference between the two versions regards the efficiency per stage, which is much higher in the CCD V03 simulation. One possible motivation is due to the shift of inlet flow coefficient ϕ_{01} which is higher than the reference leading to a benefit in terms of efficiency. Furthermore, as one of the main remarks by Ludtke is to show the efficiency dependance on the inlet flow coefficient [3], it has been decided to obtain a match of ϕ_{01} and look at the response of the code, even if the poor data available discourage from further examinations.

In this case the new results are reported in table 4.13.

CCD V03						CCD V01						
St. 1	St. 2	St. 3	St. 4	St. 5	St. 6	St. 1	St. 2	St. 3	St. 4	St. 5	St. 6	
$\eta_p[-]$	0.783	0.774	0.766	0.754	0.745	0.747	0.764	0.756	0.749	0.731	0.724	0.718

Table 4.13: Six stages efficiency comparison of CCD V03 and V01 with an inlet flow coefficient for V03 of $\phi_{01} = 0.0181$, as the compressors' one, and $\phi_{01} = 0.027$ for V01

The new off design maps can be evaluated in fig. (4.12))

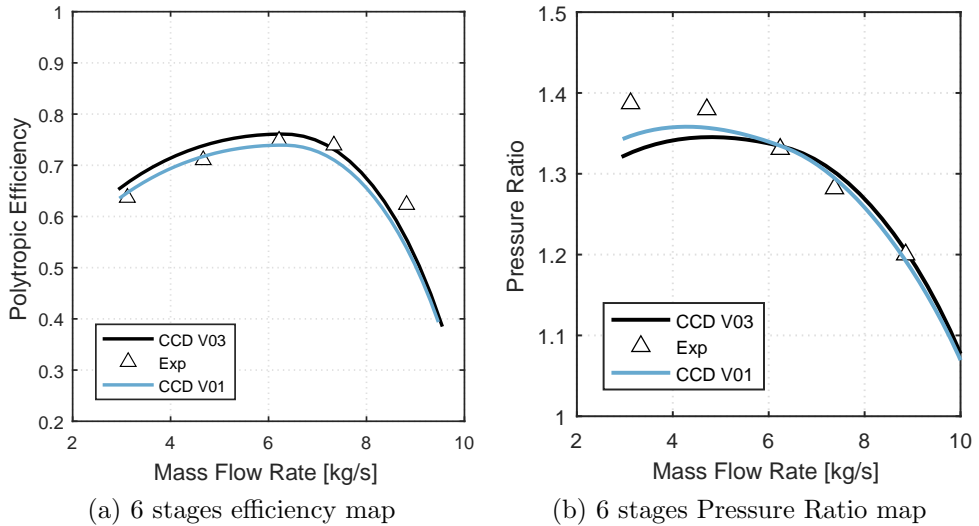


Figure 4.12: Efficiency and PR maps comparison for the 6 stages case with ϕ_{01} match

The efficiency trend in fig. (4.12) is much closer to test data for this case while the pressure ratio is still far from the reference as it approaches stall

condition.

As previously said, the lack of information did not allow a significant comparison with the real machine, also because some important inputs like the suction temperature and some fluid parameters like the isentropic flow coefficient have been guessed. If the chance of accessing data from hydrogen rich gas machine like this one would be given, it should be investigated whether the errors in the design and performance estimation are problems of the code or the analysis is just deceived by the wrong indications.

By the way, it was interesting to see how the inlet flow coefficient can affect the performances of the machine, as in general it deteriorates the efficiency when decreasing.

4.3 High Efficiency Centrifugal Compressor (HECC)

The last validation example is a high efficiency centrifugal compressor (HECC) representative of the final stage of an axi-centrifugal compressor for rotorcrafts applications [13]. The study of HECC was conducted by the american United Technologies Research Center (UTRC) and NASA with the aim of developing a compact, high work factor and performant device.

The HECC is comprehensive of a splitted impeller, with 15 full blades, a splitted vaned diffuser and an exit guide vane (EGV) as illustrated in the model designed by NASA in fig. (4.13), while the representation proposed by CCD is in fig. (4.14).

The suction conditions are summed up in table (4.14).

\dot{m} [kg/s]	$p_{0,in}$ [bar]	$p_{0,out}$ [bar]	$T_{0,in}$ [K]	N [rpm]
3.75	0.7584	3.5266	288.2	21789

Table 4.14: Suction parameters for HECC

The stage total pressure ratio is 4.65 but, as can be noticed from table (4.14) and the inlet is suppressed in order to reduce the thrust load in the facility.

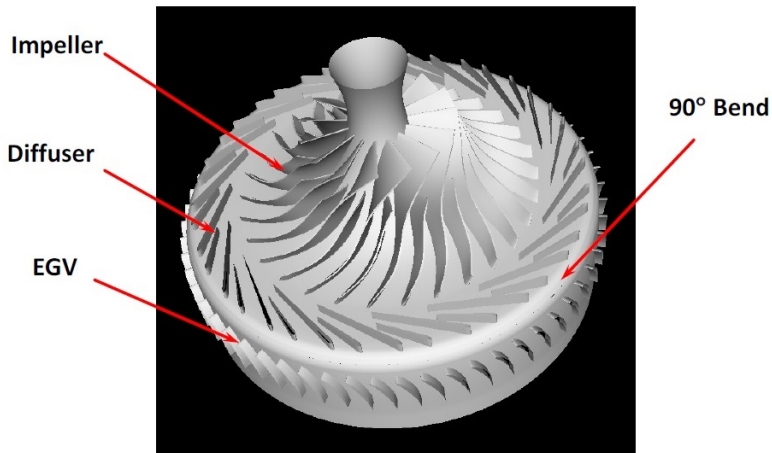


Figure 4.13: High Efficiency Centrifugal Compressor as modeled by NASA

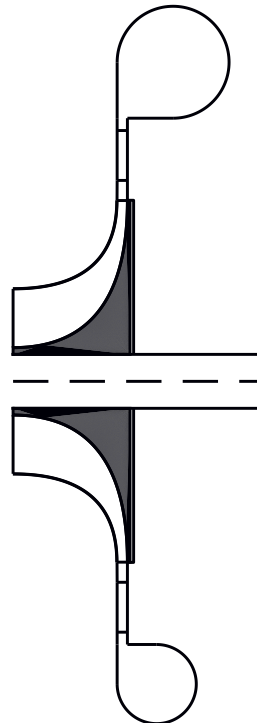


Figure 4.14: High Efficiency Centrifugal Compressor as sketched by CCD

Since HECC impeller exit angle $\beta_{2,bl}$ is varying along the span between -32° and -42° , while CCD requires only one value, a representative $\beta_{2,bl} = -37^\circ$ has been set.

Considering that in CCD there is no EGV model and the return system cannot be considered by CCD as no stage is following, an external volute has been selected in order to recreate the HECC stage exit Mach number of 0.15. Moreover, an adaption also for the diffuser is required: an equivalent vane number of 30 is assumed to approximate the vaned diffuser configuration of 20 full vanes and 20 splitted vanes.

A flow coefficient of $\phi_{01} = 0.0435$ is chosen in order to match the compressor's rotational speed of 21789 rpm. As the blade shape is fully 3D but the actual value of ϕ_{01} would lead to an intermediate configuration, the quantity d_{1m}/d_e is set to match the inlet blade geometry. Instead, a value of $\phi_{01} = 0.035$ has to be selected for CCD V01 to arrive at the same rotational speed.

The main geometrical quantities and compressor parameters are collected and compared to reference HECC data in table (4.15) and to CCD V01 in table (4.16).

The geometry of the compressor is well simulated by CCD V03 with the

	CCD V03	HECC	Relative errors
$\eta_p[-]$	0.884	0.855	+3.4%
$\lambda[-]$	0.75	0.81	-7.4%
$N[\text{rpm}]$	21780	21789	-0.04%
$d_{1h}[\text{mm}]$	80	81	-1.2%
$d_{1s}[\text{mm}]$	220	215	+2.3%
$d_2[\text{mm}]$	431	432	-0.2%
$b_1[\text{mm}]$	70	67	+4.5%
$b_2[\text{mm}]$	12.4	15.5	-20%
$d_3[\text{mm}]$	479	465	+3.0%
$N_{bl}[-]$	30	30	+0%
$d_{max}/d_2[-]$	1.455	1.45	+0.3%
$M_{out}[-]$	0.148	0.15	-1.3%

Table 4.15: Comparison between CCD V03 results and HECC data with respect to the more representative quantities

exception of the impeller tip width b_2 , which is more similar to the one given by CCD V01, that is far off-target. The geometrical and flow variations occurring along the span are probably the causes of that deviation. In fact, from the test of NASA it comes out that real flow angles become very tangent while approaching the extremities of the blade, thus requiring a bigger tip width to discharge the flow rate.

The peak polytropic efficiency is higher than the one coming out from unsteady CFD and test for a relative 3.4% but, also in steady CFD simulations run by NASA it results overpredicted. The contributions of EGV (replaced by the volute) and, in particular, the presence of unsteady phenomena occurring between impeller exit and vaned diffuser inlet, are effects that are not possible to consider with a 1D program at the state of art of CCD. For what regards CCD V01, it shows a low efficiency mainly because in its calculations it relies on the inlet flow coefficient ϕ_{01} which is quite low in this case. The same flow coefficient is the cause of the discrepancies also in the inlet width.

	CCD V03	CCD V01	Relative errors
$\eta_p[-]$	0.884	0.797	-9.8%
$\lambda[-]$	0.75	0.73	-2.7%
$N[\text{rpm}]$	21780	21730	-0.2%
$d_{1h}[\text{mm}]$	80	77	-3.8%
$d_{1s}[\text{mm}]$	220	211	-4.1%
$d_2[\text{mm}]$	431	463	+7.4%
$b_1[\text{mm}]$	70	52	-25.7%
$b_2[\text{mm}]$	12.4	12	-3.2%
$d_3[\text{mm}]$	479	513	+7.1%
$N_{bl}[-]$	30	36	+20%
$d_{max}/d_2[-]$	1.455	1.58	+8.6%

Table 4.16: HECC: Comparison between the results of CCD V03 and CCD V01

4.3.1 Off-design

Exploiting on one hand test measurements and unsteady CFD calculations performed at NASA test center and on the other CFD simulations run at the Von Karman Institute, two different off-design studies have been conducted.

Table (4.17) and table (4.18) report the off-design parameters which show the best agreement with NASA data.

A	B	C	A_s	B_s	C_s
0.5	0.4	5	0	0.4	4.75

Table 4.17: HECC paramters for blending function

	D	G	H	ϕ_P/ϕ_C	ϕ_S/ϕ_C
Low Mach	1.7	2	2	0.55	0.24
High Mach	2.1	0.3	3.5	0.95	0.835

Table 4.18: HECC: low and high limit for off-design parameters

The results of the comparison with NASA analysis are shown in fig. (4.15) and fig. (4.16).

Instead, fig. (4.17) and fig. (4.18) illustrates the maps with respect to CFD calculations performed at the Von Karman Institute (notice that the off-design speedlines analysed are different from NASA reference). No pressure ratio map of CCD V01 is plotted in fig. (4.16) and fig. (4.18) as it is almost superposed to CCD V03 one.

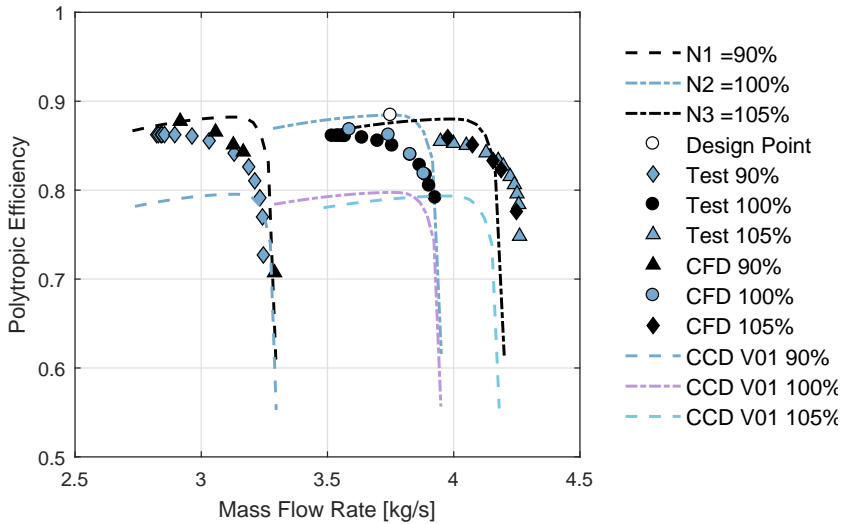


Figure 4.15: HECC efficiency map of CCD V03 compared with test data, CFD and CCD V01

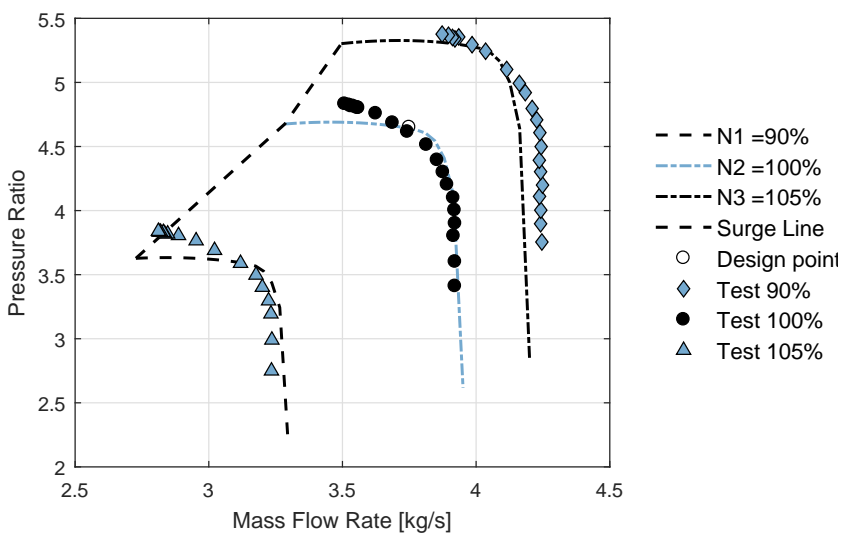


Figure 4.16: HECC pressure ratio map of CCD V03 compared with test data

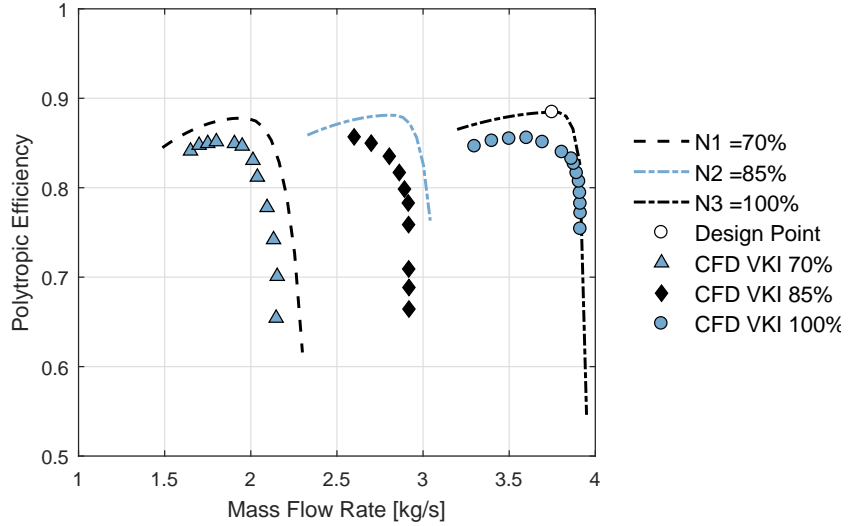


Figure 4.17: Efficiency map comparison between CCD V03 and CFD results performed at VKI

The shape of the tested pressure ratio curves is similar to the estimated one till the stall region. Once again, the uneffectiveness of the off-design approach to predict instabilities shows its limits, but it is instead reasonable for the choke region. On the contrary, the predicted efficiency map presents a shift in the 105% speedline, with respect to test data, as the choke is expected to occur before than the real one.

The comparison with the simulations run at VKI, as depicted in fig. (4.17) and fig. (4.18), demonstrates a good trend both for the efficiency, if it is not considered the effect of the overprediction, and the pressure ratio for the 100% speedline; the same can be said also for the 70% one, except for pressure ratio at choke, while the intermediate one distances itself both for stall and choke prediction.

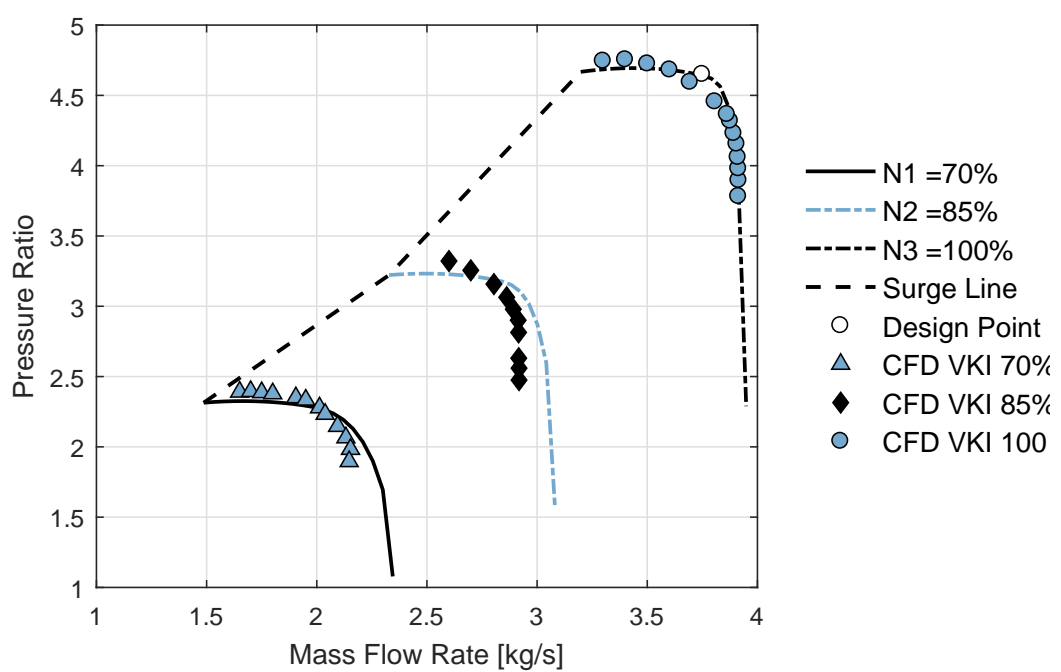


Figure 4.18: Pressure ratio map comparison between CCD V03 and CFD results performed at VKI

4.4 Summary of Validation Tests

Four reference cases have been considered to validate the capability of the new program, through an implemented loss model for the main components, to provide a reliable design and well predict the peak performances of a centrifugal compressor. For the first case in particular, both the geometrical and thermodynamic quantities confirm a good agreement with the reference data and also the efficiency is within a reasonable margin of error for all the stages, as it was for CCD V01.

Since the approach for the off-design is conducted in a very similar way, no surprise is encountered in discovering that the behaviour of the two versions is almost identical, when they have comparable starting points. Moreover, even if only few input parameters are requested by CCD to run an analysis, the first test shows the importance of having all the pivotal data available, in order to leave to chance the less possible guesses. In fact, as case two and three pointed out, the comparison is made more difficult when several unknown paramters can deceive it. In general, it seems that one characteristic of the loss model has been to attenuate the strong influence of the inlet flow coefficient in the determination of the efficiency, evaluating it on physical based correlations. As a matter of fact, even if it is of course generally true the dependence on ϕ_{01} , in some cases you can get good performances also for not high values of ϕ_{01} , as realised from the turbocharger compressor simulation.

Finally, it has to be clarified that the loss model has been validated as a whole, meaning that the performance of the entire machine have been compared with baseline references, since it was not possible to perform a component by component off-design analysis as it is not implemented in the code.

Chapter 5

Conclusions

A new one-dimensional methodology for the design and performance prediction of multi-stage centrifugal compressors has been programmed in a new version of Matlab® program CCD, obtaining encouraging feedbacks from testings. The current tool can be a helpful support for the designer when receiving a commission from a costumer. In fact, using the few specifications that would be given, among which mass flow, fluid suction conditions and total pressure ratio, CCD addresses the designer towards a reasonable configuration of the most important components of a centrifugal compressor like the impeller, the vaneless and vaned diffuser, the return system and the volute. New design methodologies based on good design practices have been indeed incorporated in CCD in order to size them. To give more flexibility to the user, in an input file the possibility of assembling an arbitrary compressor has been given by specifying the desired components that will compose the machine, plus controlling some settings about their principal characteristics.

Since one of the biggest issues when dealing with a turbomachine is the computation of the losses occurring in it, a comprehensive 1D loss model provided by Aungier [1] has been implemented in the code for all the elements of the compressor, allowing to properly evaluate the performances at design point through the use of correlations that rely on the geometrical and flow quantities previously calculated. For what concernss the off-design, instead, an approach based on non-dimensional parameters has been followed. In fact, even if the the loss correlations employed can be applied for off-design conditions, it was not possible to simply change the inlet mass flow in the input file to obtain the performance and efficiency maps because this would have lead to a variation of the geometry of the compressor, as the main routine is suited for a design process. Therefore, a specific procedure has to be studied to perform such calculations and it can be a topic for a future work on CCD.

5.1 Future Works

Multi-objective optimization

In the estimation of the performances of a compressor the efficiency is not the only parameter to worry about but also a wide range of operation has to be accounted. Since CCD predicts only one reasonable design but maybe not the best one, it can be useful to run an optimization which guides the designer towards the most appropriate configuration for the required compressor. Currently, some optimization analyses are already running at the Von Karman Institute in order to be able to achieve this goal.

New programming language When a multi-objective optimization is considered important, the need of quick simulations becomes really pivotal as thousands of them have to be carried out. Since the coupling of an optimization software with Matlab is not efficient, a transition of CCD to Python may be the right choice to pick, so that even an articulate optimization can be done in a reasonable time.

Off-design

The next step for CCD is the use the loss correlation models also for the off-design, comparing the results with respect to Casey and Robinson approach. This will be possible by implementing another separate routine which takes in input the main geometrical quantities obtained during the design phase. For each speedline, choke condition can be evaluated from the velocity which causes choke in the throat while stall condition can be decided by fixing a limit value for diffusion ratio w_{1s}/w_2 . The thermodynamic quantities are calculated in order to estimate the efficiency and the pressure ratio.

Modeling of new components Some missing components that could be additionally modeled in CCD are represented by regulation systems such as Inlet Guide Vane (IGV) or diffuser guide vane (DGV). With this addition, also a more proper off-design analysis could be carried out.

Real gas behaviour Even if the compressibility effect in a compressor is not as much important as in a gas turbine, where the temperatures can be incredibly high, the use of more powerful thermodynamic correlation can be employed to better estimate the properties of the fluid across the machine, so to render the 1D performance analysis more reliable.

Chapter 6

References

- [1] R.H. Aungier, *Centrifugal Compressors: a Strategy for Aerodynamic Design and Analysis*, ASME PRESS 2000
- [2] M. Casey, C. Robinson *A method to estimate the Performance Map of a Centrifugal Compressor Stage*, Journal of Turbomachinery, November 2012
- [3] K.H. Lüdtke, *Process Centrifugal Compressor: Basics, Function, Operation, Design, Application* , Springer 2004
- [4] P. Harley, S. Spence, D. Filsinger, M. Dietrich and J. Early *Assessing 1D Loss Models for the Off-Design Performance Prediction of Automotive Turbocharger Compressors* June 2013
- [5] A. Whitfield, N. C. Baines *Design of Radial Turbomachines*, Longman Singapor Publisher (Pte) Ltd., 1990
- [6] N. Cumpsty, *Compressor Aerodynamics*, Krieger Publishing Company, 1989
- [7] M. Casey and M. Schlegel, *Estimation of the performance of turbocharger compressors at extremely low pressure ratios*, Proceedings of the Institution of Mechanical Engineers, Part A: Journal of Power and Energy, vol. 224, no. 2, pp. 239-250, 2010
- [8] W. Al-Busaidi and P. Pilidis, *A new method for reliable performance prediction of multi-stage industrial centrifugal compressors based on stage stacking technique: Part I - existing models evaluation*, Applied Thermal Engineering, vol. 98, pp. 10 - 28, 2016

- [9] A. Srinivasan and C. Impastato, *Application of integral geared compressors in the process gas industry*, ASME, vol. GT, no. 95870, 2013
- [10] P. Dalbert, M. Casey, and E.Schurter, *Development testing and performance prediction of radial compressor stages for multi-stage industrial compressors*, Thermal Engineering, vol. 88-GT-34, 1988
- [11] R. Van den Braembussche, *Centrifugal Compressors: Analysis and Design*. Course Note 192, 2015
- [12] A. Romei, *Design and optimization of multi-stage centrifugal compressors with uncertainty quantification of off design performances*, Master Thesis, Polytechnic of Milan, 2016
- [13] G. Medic et al., *High efficiency centrifugal compressors for rotorcraft applications*, NASA/CR-2014-218114
- [14] R. H. Aungier, *Centrifugal compressor stage preliminary aerodynamic design and component sizing*, ASME 95-GT-78
- [15] R. H. Aungier, Aerodynamic design and analysis of vaneless diffusers and return channels, ASME 93-GT-101, 1993
- [16] R. H. Aungier, *Mean streamline aerodynamic performance analysis of centrifugal compressors*, ASME Vol. 117, p. 360-366, July 1995
- [17] R. H. Aungier, *Sealing flow requirements for a rotating disk with external swirling flow*, ASME 94-GT-86, 1994
- [18] R. H. Aungier, *A fast, accurate real gas equation of state for fluid dynamic analysis applications*, ASME Vol.117, p.277-281, 1995
- [19] P. Came and C. Robinson, *Centrifugal compressor design*, Proceedings of the Institution of Mechanical Engineers, vol. 213, no. C, pp. 139-155, 1998
- [20] D. Rusch and M. Casey, *The design space boundaries for high flow capacity centrifugal compressors*, Journal of Turbomachinery, vol. 135, no. 3, pp. 1-11, 2013
- [21] S. Dixon and C. Hall, *Fluid Mechanics and Thermodynamics of Tur-*

bomachinery, Elsevier Inc., 6th ed., 2010

[22] F. Wiesner, *A review of slip factors for centrifugal impellers*, Journal of Engineering for Power, vol. 89, no. 4, 1967

[23] J. Daily and R. Nece, *Chamber dimension effects on induced flow and frictional resistance of enclosed rotating disks*, ASME J.Basic Eng., vol. 82, pp. 217-232,1960.

[24] E. Swain, *Improving a one-dimensional centrifugal compressor performance prediction method*, in Proc. IMechE Part A, pp. 653-659, 2005

[25] H. Oh, E. Yoon, and Chung, *An optimum set of loss models for performance prediction of centrifugal compressor*, in Proc. IMechE Part A, pp. 331-338, 1997

[26] W. Al-Busaidi and P. Pilidis, *A new method for reliable performance prediction of multi-stage industrial centrifugal compressors based on stage stacking technique: Part ii - new integrated model verification*, Applied Thermal Engineering, vol. 90,pp. 927-936, 2015

[27] M. Casey and D. Rusch, *The matching of a vaned diffuser with a radial compressor impeller and its effect on the stage performance*, in Proceedings of ASME Turbo Expo 2014, pp. 1-14, 2014

[28] C. Rodgers, *Typical performance characteristics of gas turbine radial compressor*, ASME J. Eng. Power, vol. 86, 1964

[29] N. Baines, *Fundamentals of Turbocharging*. Concepts NREC, 2005

[30] H. Simon, *Design concept and performance of a multistage integrally geared centrifugal compressor series for maximum efficiencies and operating ranges*, ASME,vol. 87-GT, no. 43, 1987

[31] S. Pierret, *Designing turbomachinery blades by means of the function approximation concept based on artificial neural network, genetic algorithm, and the Navier-Stokes equations*. PhD thesis, Polytechnique de Mons - von Karman Institute for Fluid Dynamics, Mons (Belgium), 1999

[32] C. Osnaghi, *Teoria delle Turbomacchine*. Società Editrice Esculapio, oct 2013.

- [33] C. Rodgers and L. Sapiro, *Design considerations for high pressure ratio centrifugal compressor*, American Society of Mechanical Engineering
- [34] P. Dalbert, M. Casey, and E. Schurter, *Development testing and performance prediction of radial compressor stages for multi-stage industrial compressors*, Applied Thermal Engineering, vol. 88-GT-34, 1988
- [35] M. V. Casey, *The effects of Reynolds number on the efficiency of centrifugal compressors stages*, Vol 107 April 1985
- [36] K. Ludtke, *The influence of adjustable inlet guide vanes on the performance of multi-stage industrial centrifugal compressors*, ASME 92-GT-17, 1992
- [37] C. Rodgers, *Centrifugal compressor inlet guid vanes for increased surge margin*, ASME Vol.113 October 1991
- [38] C. R. Weber, M. E. Koronowski, *Meanlineperformance prediction of volutes in centrifugal compressors*, ASME 86-GT-216, 1986
- [39] J.H.Horlock, *Axial flow compressors, fluid mechanics and thermodynamics*, Krieger, 1973
- [40] M.V. Herbert *A method of performance prediction for centrifugal compressors* Aeronautical research council reports and memoranda, 1980
- [41] P. Yuan, C.Wei, Y. Song, *A new optimization method for centrifugal compressors based on 1D calculations and analyses*, Energies 2015,8,4317-4334
- [42] X. Gong, R. Chen, *Total pressure loss mechanism of centrifugal compressors*, Canadian Center of Science and Education, Vol.4, No.2, 2014
- [43] P. Harley et al., *An evaluation of 1D design methods for the off-design performance of automotive turbocharger compressors*, ASME, GT2012-69743
- [44] M. R. Galvas, *Fortran program for predicting off-design performance of centrifugal compressors*, NASA TN D-7487, November 1973